2018

MECHANISTIC STUDIES OF PROTON-COUPLED ELECTRON TRANSFER REACTIONS INVOLVING ANTIOXIDANTS

Kejie Meng

Follow this and additional works at: https://scholarscompass.vcu.edu/etd

Part of the Analytical Chemistry Commons, and the Physical Chemistry Commons

Mechanistic Studies of Proton-Coupled Electron Transfer Reactions Involving Antioxidants

A dissertation submitted in partial fulfillment of the requirements for the degree of Doctor of Philosophy at Virginia Commonwealth University.

By

Kejie Meng

Doctor of Philosophy

Department of Chemistry

Director: Dr. Julio C. Alvarez

Director of Graduate Students, Associate Professor

Department of Chemistry

Virginia Commonwealth University

Richmond, Virginia

May, 2018

Acknowledgments

I would like to express my special thanks and appreciation to my advisor Dr. Julio Alvarez for his guidance and support throughout my PhD journey. I thank him for training me to become an independent researcher and a problem solver by his encouragement and patience.

I also want to thank my committee members: Dr. Maryanne M. Collinson, Dr. Jose U. Reveles Ramirez, and Dr. Matthew C. T. Hartman for great comments and suggestions about my proposal defense and research. I give many thanks to my previous colleagues Jonnathan Medina-Ramos and Timothy M. Alligrant for helping me at the beginning of my research project. I thank Dr. Sarah Rutan and Dr. Michael Hunnicutt for helping me out with my research presentation and teaching experience. I thank my labmates, high school students, and undergraduate students for working with me on the projects.

I would like to thank my friends Edmund Perozzi and Rhoda Perozzi for their support, friendship, and great comments on my writing. Many thanks to all my friends in Richmond, Virginia.

I would like to thank my family in China for their continuous love. I especially thank my husband, Shanwei Shen, for unconditional understanding, support, and taking care of me.

Finally, I want to thank the Department of Chemistry at Virginia Commonwealth University for giving me the opportunity to work on my graduate career. I greatly appreciate the sponsors of the Fred M. Hawkridge Scholarship, Altria Graduate Assistantships, and VCU Presidential Research Quest Fund, which supported me in my research work.

Table of Contents

List of Tables

Chapter 1: NA

Chapter 2:

Chapter 3:

Chapter 4: NA

List of Figures

Chapter 4:

List of Schemes

List of Symbols and Abbreviations

PCET	Proton-coupled electron transfer
PT	Proton transfer
ET	Electron transfer
B	Base form of buffer
BH^+	Acid form of buffer
A-X	Oxidized molecule
I	Intermediate
TS	Transition states
$\Delta G°$	Gibbs free energy
OH	Hydroxyl functional groups
SH	Sulfhydryl functional groups
Cys	Cysteine
TEAC	Trolox Equivalent Antioxidant Capacity
CA	Chronoamperometry
CC	chronocoulometry
GSH	Reduced glutathione
GS^-	Glutathione in the thiolate form
$GS^\bullet$	Glutathione radical
$GSH^{\bullet+}$	Glutathione radical cation
GSSG	Glutathione disulfide
TOH	Trolox
ABTS	2,2' – azinobis-(3-ethylbenzothiazoline-6-sulfonic acid)
$ABTS^{\bullet+}$	2,2' – azinobis-(3-ethylbenzothiazoline-6-sulfonic acid) radical cation
Bu_4NPF_6	Tetrabutylammonium hexafluorophosphate
ACN	Acetonitrile
n	Number of electrons
Q	Charge
F	Faraday constant
TO^+	Trolox in phenoxonium cations form
TO^-	Trolox in phenolate anion form
$TO^\bullet$	Trolox in phenoxyl radical form
TOQ(OH)	Trolox in Quinone from
$TOH^{\bullet+}$	Trolox in the cation radical form
α-TOH	α-Tocopherol
α-TO^+	α-Tocopherol in phenoxonium cations form
α-TOQ(OH)	α-Tocopherol in hemiketal form
α-$TO^\bullet$	α-Tocopherol in phenoxyl radical form
PCE	Particle collision electroanalysis
LOOH	Lipid hydroperoxide
$LOO^\bullet$	Oxidized lipid hydroperoxide

PKC	Protein kinase C
α-TOH$^{+\bullet}$	α-Tocopherol in the cation radical form
α-TOH^{2+}	α-Tocopherol in the dication form
α-TO^{-}	α-Tocopherol in the phenolate anion form
EDR	Emulsion droplet reactor
IL-PA	Ionic liquid, trihexyltetradecylphosphonium bi(trifluoromethylsulfonyl)amide
DI	Deionized water
DLS	Dynamic light scattering
ε	Dielectric constant
D_{ems}	Diffusion coefficient of a spherical emulsion droplet
f	Collision frequency
k_B	Boltzmann constant
T	Temperature
η	Viscosity
r_{ems}	Radius of droplet
$r_{electrode}$	Radius of the electrode
$Cems$	Concentration of the emulsion droplets
N_A	Avogadro's number
i	Current
δ	Thickness of diffusion layer
D	Diffusion coefficient
PCET	Proton-coupled electron transfer
v	Scan rate
A	Electrode surface area
R	Universal gas constant
Γ	Surface coverage
k_s	Heterogeneous rate constant
α	Transfer coefficient
K_{eq}	Equilibrium contant
k_f	forward rate constant
ΔE_p	Potential peak difference
RSD	Rate determining step
k_{obs}	Observed rate-constant
KIE	Kinetic isotope effect
M	Mediators
CV	Cyclic voltammetry

Abstract

MECHANISTIC STUDIES OF PROTON-COUPLED ELECTRON TRANSFER REACTIONS INVOLVING ANTIOXIDANTS

By Kejie Meng, Ph.D in Chemistry

A dissertation submitted in partial fulfillment of the requirements for the degree of Doctor of Philosophy at Virginia Commonwealth University.

Virginia Commonwealth University, 2018

Thesis Director: Julio C. Alvarez, Ph.D., Department of Chemistry at VCU

The objective of the research was to investigate proton-coupled electron transfer (PCET) reactions involving antioxidants to gain insight into the detailed mechanisms of glutathione (GSH), Trolox, and α-tocopherol (α-TOH). PCET reactions are complex redox reactions that transfer electrons and protons sequentially or in concert. These reactions are ubiquitous in natural or artificial processes that produce electrochemical energy that is extractable as electricity or as chemical fuels of high energy content. Examples of processes based on PCET are photosynthesis, respiration, nitrogen fixation, carbon dioxide reduction, redox fuel cells, and artificial photosynthesis. Antioxidants were selected as a PCET model to understand the coupling between proton transfer (PT) and electron transfer (ET) in order to elucidate structure-reactivity relationships under different experimental conditions. PCET reactions were studied with a set of electrochemical techniques to propose a preliminary mechanism that could be validated with

digital simulations matching the electrochemical response. In some cases, other analytical techniques were used to aid in the system characterization. This thesis presents the results and discussion of the effects of oxidant-base pairs on the mediated oxidation of GSH, the $-2e^-/-H^+$ process of Trolox in aqueous and nonaqueous solvents with various pH values, and the particle collision electrolysis of α-tocopherol in oil-in-water emulsion droplets on an ultramicroelectrode. Ultimately our goal was to determine the kinetic and thermodynamic factors that control PCET reactions so that they can be applied in designing artificial systems for the production of energy using more abundant reagents with lower cost and better yields.

Chapter 1: Introduction and background

1.1 Proton-coupled electron transfer

Electron transfer (ET) and proton transfer (PT) are involved in numerous chemical reactions that occur in biological, environmental, and other chemical systems.[1][2][3] Examples are the $1e^-$, $1H^+$ oxidation of biological thiols such as cysteine (Cys), glutathione (GSH), and homocysteine, which are common targets of research due to their biological role as antioxidants in cells.[4][5] The $2e^-$, $2H^+$ oxidation of hydroquinone and the reduction of benzoquinone have also received attention because of the role of quinones in photosynthesis.[6] Such reactions are termed proton-coupled electron transfer (PCET) because they involve the transfer of electrons and protons in coupled steps; however, the sequence of the transfer may vary. In some cases, the electron transfer is completed before the proton transfer or vice versa, while in some reactions both the proton and electron are transfered in a single step without forming a stable intermediate.[7][8]

Concerted PCET, commonly represented by CPCET, means that the ET and PT occur in a single step. "Concerted" implies the absence of an intermediate but does not indicate synchronous transfer.[8] Some authors use "concerted proton-electron transfer" (CEP) to replace the notation CPCET.[7][8][9] The stepwise pathway, ETPT or PTET, implies that the ET and PT take place in two consecutive kinetic steps. Scheme 1.1 is typically used to facilitate the discussion of $1e^-/1H^+$ PCET mechanisms. The species A-X-H in Scheme 1.1 represents an oxidizable molecule and functions as a redox active Bronsted acid. B is a base acting as proton acceptor. A-X-H can donate an electron and a proton in the presence of B, so that the radical A-X$^\bullet$ and BH^+ are

produced. The horizontal lines in Scheme 1.1 refer to PT reactions and the vertical lines refer to ET. The coupled routes ET-PT (vertical-horizontal) and PT-ET (horizontal-vertical) represent the stepwise mechanisms whereas the diagonal pathway represents the concerted reaction (CPCET).[8]
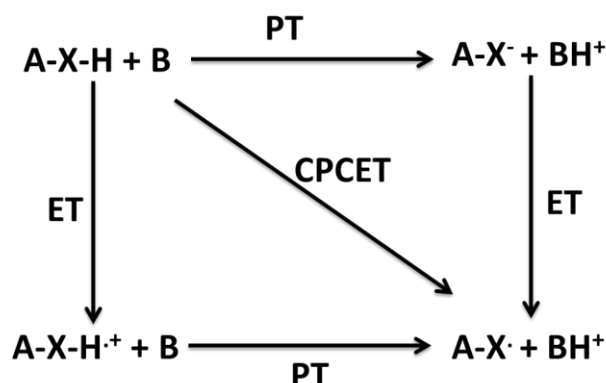
Scheme 1.1 Square schemes for proton-coupled electron transfer (PCET).

The stepwise processes go through an intermediate (I) connecting two transition states (TS) (Scheme 1.2). The intermediate states are uphill (thermodynamically unfavorable) from the final product.[8] In the concerted pathway, there is a single transition state involving the concerted transfer of both the proton and electron without the formation of intermediate species (Scheme 1.2).[8] The $\Delta G°$ for CPCET is often more negative than the value of $\Delta G°$ for the initial ET or initial PT which indicates that concerted reactions are thermochemically favored over stepwise paths. However, thermodynamic considerations are not sufficient to determine reaction pathways. Over the last 20 years, chemical and electrochemical studies involving theoretical and experimental methods have been done to investigate the kinetic and thermodynamic behavior of PCET reactions in order to further understand their mechanisms. The goal of this thesis research was to investigate the factors (oxidants, base, pH, pK_a) that affect the interplay between ET and

PT, which can be applied in designing artificial systems for the production of energy relying on proton-coupled electron transfer processes.
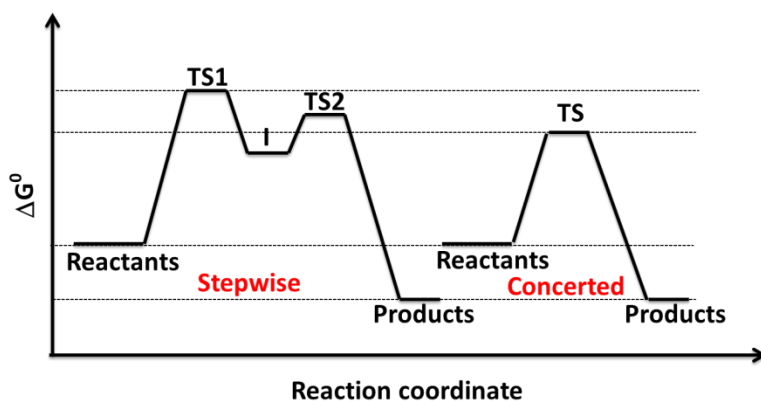
Scheme 1.2 Pathways of concerted and stepwise reactions.

1.2 PCET involving antioxidants

PCET is ubiquitous in biological redox reactions where proton transfer and electron transfer reactions are tied to the energy conversion of biomolecules. Molecules with electroactive hydroxyl (OH) and sulfhydryl (SH) functional groups are commonly selected as models to study PCET reactions. GSH, Trolox, and α-tocopherol were used for mechanistic studies of PCET reactions in this tresearch. These antioxidants are widely used as targets of research because antioxidants help to protect cells against the effects of free radicals and their concentration changes are commonly related to various pathologies.[4-5, 10] The concentration of GSH found in cells is usually in the range of 1-10 mM.[11] The first stage of GSH in antioxidant defense in cells is to lose one electron and one proton to generate a radical $GS^{\bullet}$. After the oxidation, thiol radicals dimerize and form the disulfide GSSG at a diffusion limited rate.[4-5, 10] The proton-coupled electron transfer reactions occurred in the first stage of the oxidation of GSH. In this research, the mechanistic studies of GSH were achieved electrochemically by using metal complexes ($Mo(CN)_8^{3-}$, $IrCl_6^{2-}$, $Fe(phen)_3^{3+}$) as mediators, where the oxidation of GSH was

studied by analyzing the redox current changes of the mediators indirectly.[12] The rate of oxidation of GSH was investigated in buffered aqueous solutions at various concentrations, different pH values, and various pk_a values. The apparent exothermic and endothermic values of $^{app}\Delta G°'$ for proton transfer and electron transfer were obtained as described later. The work in chapter 2 provides a better understanding of the interplay between PT and ET, which will help in designing catalysts for the energy harvesting process with better yields. α-Tocopherol (α-TOH) is by far the most naturally abundant and biologically active component of vitamin E. The functional group OH of α-tocopherol can react with a free radical in mammalian tissues to protect living cell lipids.[13] [14] [15] Vitamin E has been proposed to terminate the free radical chain autoxidation cycle by first reacting with a hydroperoxide radical ($LOO^\bullet$) to generate a lipid peroxide (LOOH) in a cell membrane and a tocopherolxyl radical (α-$TO^\bullet$). Second, the tocopherolxyl radical reacts with another hydroperoxide radical to terminate the autoxidation cycle. The PCET reaction happens in the first step of the oxidation of α-TOH. However, a growing body of evidence shows that α-TOH can also act as a cellular signaling molecule by interacting with other proteins and enzymes of the cell.[16] [17] [18] It is generally true that natural phenols have an antioxidative function in biological systems and α-TOH and α-$TO^\bullet$ are thought to be involved in the biological chemistry of its antioxidative cases. [19] [13-14] Electrochemical experiments have demonstrated that α-TOH undergoes a $-2e^-/-H^+$ process and that additional semistable oxidized compounds are formed. Examples of these semistable compounds are phenoxonium cation (α-TO^+), cation radical (α-$TOH^{+\bullet}$), dication (α-TOH^{2+}), phenolate anion (α-TO^-), hemiketal (α-TOQ(OH)), and p-quinones, which were determined by a combination of electrochemical and in situ spectroscopic analyses.[20] [21] [22] The phenoxonium cation (α-TO^+) has a long life and is unlikely to react with free radicals under the environmental conditions compared

with α-TO•.[23] Richard's research group proposed that α-TO⁺ may have important role in α-TOH's non-antioxidant actions and that all other oxidized forms of vitamin E are worthy of consideration.[24] Currently, there are no detailed mechanisms in existence that explain the functions of phenoxonium cations in biological systems, but the work described in chapter 4 explored those properties. Trolox is an analogue of α-TOH but is more hydrophilic since it has a carbonyl group at the 2-position instead of the extended phytyl hydrocarbon chain. Trolox is used as a standard in the Trolox Equivalent Antioxidant Capacity (TEAC) assay to measure the antioxidant capacities of natural antioxidants because it enables the TEAC assay to study both water-soluble and lipid-soluble antioxidants.[25] Proton-coupled electron transfer reactions happened to the OH group of Trolox at the 6-position. In the procedures of the TEAC assay, Trolox and antioxidative samples react separately with generated ABTS [2,2' – azinobis-(3-ethylbenzothiazoline-6-sulfonic acid)] radical cations. The decrease in ABTS•⁺ concentration by adding a certain concentration of antioxidant sample, is related to that of 1mM Trolox and provides the TEAC values of the antioxidant. This assay is the one most widely used since it is not expensive and has straight forward procedures.[26] [27] [25] However, the TEAC values of a single compound or sample differed in various solvents or pH values.[26] The details of the mechanism between Trolox and ABTS•⁺ under different experimental conditions are still not clear. A deeper understanding of the electrochemical reactions of Trolox in aqueous and nonaqueous solutions is required. As described in chapter 3, the anodic oxidation of Trolox was studied in water and acetonitrile solutions at various pH values. Electrochemical methods and UV-vis spectroscopy were used to characterize the generated intermediates and products. Digital simulation was used to evaluate our proposed oxidation mechanism of Trolox. The results and discussions presented in Chapter 3 will help to improve TEAC assay.

1.3 Electrochemical methods

The electrochemical experiments on antioxidants presented here were performed at various pH values, under aqueous and nonaqueous solutions, and in the presence of various concentrations of buffer solutions. Macroelectrodes (3 mm in diameter GC, 2 mm in diameter Pt) and an ultramicroeledtrode (10 µm in diameter Pt) were used for electrochemical measurements in the following three research projects (chapters 2, 3, and, 4). Cyclic voltammetry, chronoamperometry, chronocoulometry, and bulk electrolysis were the primary electrochemical techniques used in this research. Digital simulation was used to simulate the experimental data in order to test the validity of the proposed mechanism and obtain related thermodynamic and kinetic parameters. This section of the introduction and background chapter describes the fundamentals of the commonly used electrochemical techniques and the procedures required to use digital simulation software.

1.3.1   Cyclic voltammetry

Cyclic voltammetry is a commonly used electroanalytical technique for the study of electroactive species. This technique has been extensively used in the fields of electrochemistry, inorganic chemistry, organic chemistry, and biochemistry.[28] In this method, the potential of a working electrode is changed linearly through time, starting from the initial potential where no reduction or oxidation reaction occurs and moving to potentials where the electron transfer reaction of the redox species occurs. After traversing the peak potential (about 200 mV beyond), the direction of the linear sweep is reversed, and the electrochemical current of the intermediates and products formed during the forward scan can be detected.[29] The scan rate (v) controls the time scale of the experiment. A supporting electrolyte is commonly used to increase the conductivity and maintain the ionic strength of the solutions.[28] Several important parameters can

be obtained from the cyclic voltammogram (CV, current-potential curve) directly: cathodic (E_{pc}) and anodic (E_{pa}) peak potentials, cathodic (i_{pc}) and anodic (i_{pa}) peak currents, half-peak potential ($E_{p/2}$) and half-wave potential ($E_{1/2}$). Cyclic voltammetry measurements can also be used to calculate the diffusion coefficient (D) of the redox species, the number of electrons transferred in the reaction process, and the heterogeneous rate constant of the electron(s) transferred to/from the working electrode.[28]

Cyclic voltammetry consists of cycling the potential of the working electrode and measuring the current response. Scheme 1.3 shows the simplified three-electrode setup used for electrochemical experiments. The potentiostat was used to control the potential applied to the working electrode which was measured with respect to the reference electrode. The auxiliary or counter electrode, along with the working electrode, provides a circuit for current flow. Therefore, the potential changes of the working electrode are measured independently and more accurately compared with a two-electrode setup.[28] Different electrode materials can lead to different cyclic voltammogram responses.[30] In the present work, a glassy carbon (3 mm in diameter) electrode was used to study the mediated oxidation of GSH and electrochemical reaction of Trolox in aqueous solutions. A Pt electrode was used to detect the oxidation reaction of Trolox in organic solvent (Pt 2 mm in diameter) and the particle collision electrolysis of α-tocopherol in toluene emulsion droplets (Pt 10 µm in diameter). Ag/AgCl and Ag wire were used as the reference electrodes. A Pt wire was used as counter electrode in all the electrochemical experiments. The three-electrode setup was put inside a Faraday cage, to minimize the electromagnetic interference from the surroundings when running all voltammetric experiments.
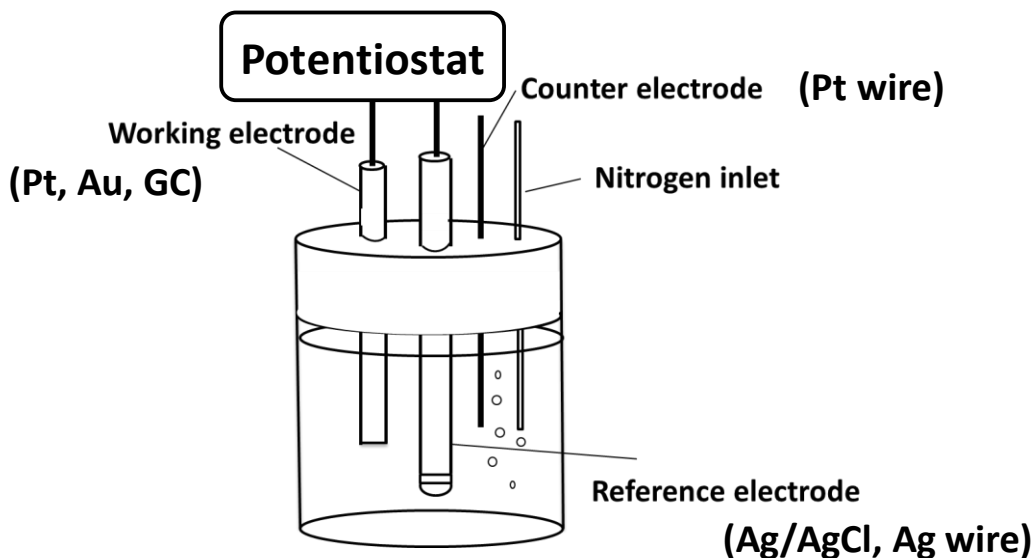
Scheme 1.3 Standard three-electrode cell setup connected to a potentiostat used for cyclic voltammetry experiments.

Scheme 1.4 shows the difference in the voltammograms for a macroelectrode and a microelectrode. In principle, a stationary electrode immersed in an unstirred electrolyte solution is given a potential that changes linearly over time in the forward and backward scans. When the potential is scanned from negative to positive, the electroactive species can undergo an oxidation reaction (heterogeneous charge transfer) in the electrolytic solutions, that is, electrons will be transferred from the redox species to the electrode.[28] The concentration of redox species on the surface of the electrode starts to change at the same time, in that the starting materials start to diffuse to the electrode and the oxidized forms set off diffusive mass transport from the electrode. Depending on the size of the electrode and the volume of the electrolytic solution used, voltammograms can distinguish between macroelectrodes and microelectrodes. For disk macroelectrodes with a diameter ≥ 1 mm, mass transport perpendicular to the electrode is in the form of a semi-infinite planar diffusion and this process produces the characteristic cyclic

voltammogram.[31] The current response is typically described as "diffusion limited" and gives

rise to an asymmetric peak, as shown in Scheme 1.4 (left).[32] As the electrode size is reduced to

an ultramicroeletrode, the diffusion process depends on the shape of the electrode and

convergent diffusion to the edges of the electrode become significant. A spatial diffusion field

develops which results in the loss of the typical "duck" shaped response,[29] as is evident in

Scheme 1.4 (right), to form a sigmoidal voltammogram. When scanning the potential in the

reverse direction (from positive to negative), the reduction reaction happens at a macroelectrode

(under planar diffusion) and the oxidation reaction occurs at the ultramicroelectrode (under

spherical diffusion).[28] For the electrochemically reversible electron transfer process, the

magnitude of the voltammetric current (i_p) observed at a macroelectrode is governed by the

following Randles-Sevcik equation[28]:

$$i_p = 0.446nFAC^\circ \left(\frac{nFvD_\circ}{RT}\right)^{1/2} \qquad \text{Equation 1.1}$$

where i_p is the peak current (A), v is the scan rate (V/s), n is the number of electrons

transferred in the redox reaction, A is the electrode surface area (cm^2), $D_\circ$ is the diffusion

coefficient of the analyte (cm^2/s), C° is the bulk concentration of the redox species (mole cm^{-3}),

F is the Faraday's constant, R is the universal gas constant, and T is the temperature (K). If the

electrochemically reversible process involves freely diffusing redox species, the peak current

(i_p) increases linearly with the square root of the scan rate v, and the equation can be used to

calculate the surface area of the electrode (A) and the diffusion coefficient ($D_\circ$) of the redox

species in the solution. The magnitude of the steady state current (i_{ss}) observed at an

ultramicroeletrode is expressed by the steady-state current equation which is independent of

the scan rate (v):

$$i_{ss} = 4nr_\circ FD_\circ C \qquad \text{Equation 1.2}$$

where $r_{\circ}$ is the radius (cm) of a ultramicroelectrode. This equation can be used for both spherical and hemispherical electrodes and provides information on the n and $D_{\circ}$ of the redox species in the electrolyte solution.[28]
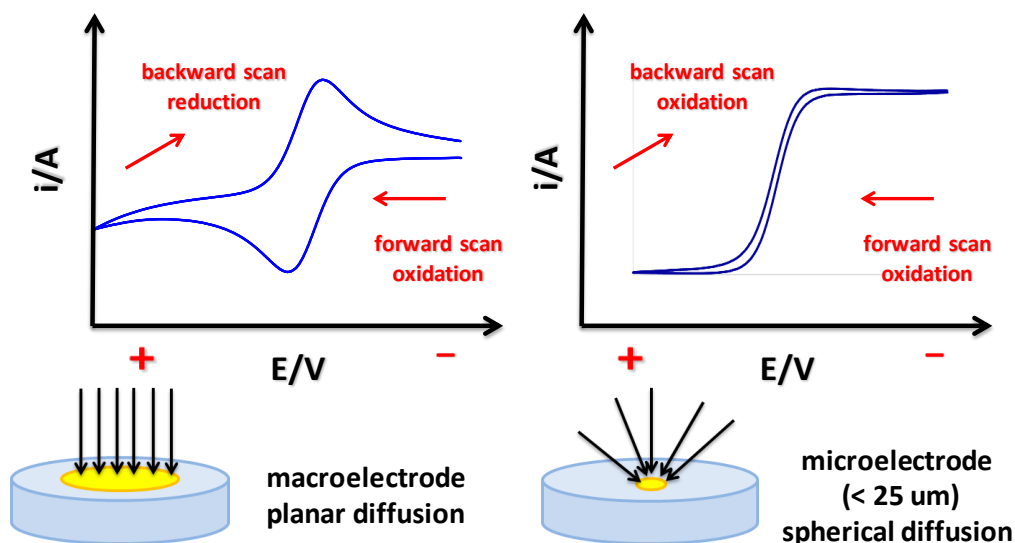
Scheme 1.4 Voltammetric current-voltage curves. Left: for semi-infinite planar diffusion to a macroelectrode; right: for spherical diffusion to a microelectrode.

Electrochemical behaviors of electroactive reactants adsorbed on the electrode surface are different from voltammograms described in Scheme 1.4. The peak current (i_p) is directly proportional to scan rate (v) when redox species are adsorbed on the electrode surface.[33] The cathodic and anodic current peaks will appear at the same potential and have equal magnitudes for ideal, reversible adsorbed electroactive species.[28]

Cyclic voltammetry can also be applied to the qualitative diagnosis of homogeneous chemical reactions that are coupled to electron transfer reactions.[28] As described later in Chapter 2, the mediated oxidation of GSH is the sample case of E_rC_i process. E indicates a heterogeneous electron transfer reaction and C represents a homogeneous chemical step. The subscript r indicates reversibility and subscript i indicates irreversibility. The E_rC_i mechanism of the

mediated oxidation of GSH shows the reversible electron transfer of mediators on the surface of a working electrode followed by an irreversible homogeneous chemical reaction between GSH and oxidized mediators in the solution. The reversible, one-electron transfer reaction of the mediator gives rise to a "duck" shaped voltammogram. A slow homogeneous chemical reaction results in a more complicated voltammogram because the oxidized mediator reacts to GSH in the solution. When the rate constant of the chemical reaction increases, the amount of oxidized mediator consumed in the chemical reaction increases. The ratios of the anodic to cathodic peak currents increase because the oxidized mediator is consumed by GSH, resulting in fewer species to reduce on the cathodic scan. The scan rate affects the experimental response because the time scale of the experiment competes with the time scale of the chemical reaction. Therefore, cyclic voltammograms can provide kinetic and mechanistic information for electron transfer reactions coupled with chemical reactions processes. The oxidation reactions of Trolox and α-tocopherol undergo two sequential electron transfer reversible processes as described in Chapters 3 and 4.

1.3.2 Chronoamperometry and chronocoulometry

As shown in Equations 1.1 and 1.2, when the sizes of electrodes are reduced, the current responses of the electrodes undergo qualitatively similar changes because, as the distance from the working electrode increases, the redox species flux per surface unit decreases.[28] Chronamperometric (CA) and chronocoulometric (CC) techniques can provide more details of this phenomenon.
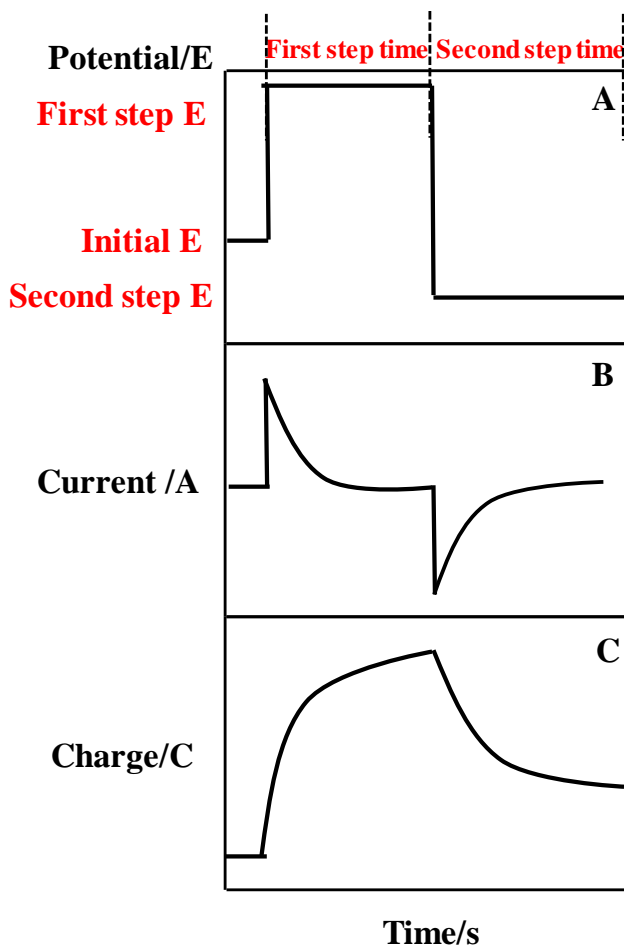
Figure 1.1 Potential wave form of double potential step vs. time (A); the current response vs. time (B); the charge response vs. time (C).

As shown in Figure 1.1, the redox reaction does not occur when the value selected is the **Initial E** and when there are no concentration gradients adjacent to the electrode surface. The **First step E** and **Second step E** are sufficient to completely reduce or oxidize a dissolved electroactive species at the electrode surface. The current vs. time for the double potential step CA experiment is shown in Figure 1.1 B. When the potential is stepped to **First step E** or **Second step E**, there is a current "spike" followed by a gradual decay in the current. The current response is a measure of the rate of electrolysis.[28] The current "spike" is generated by electrolyzing the redox species adjacent to the electrode surface. Once these substrates have been

electrolyzed, the current is controlled by the rate of diffusion of the starting materials (in the forward step) or the generated products (in the reverse step). [34] The current vs. time plot for CA is described by the Cottrell equation:[28]

$$i = \frac{nFAC_\circ \sqrt{D_\circ}}{\sqrt{\pi t}}$$

Equation 1.3

where the current decreases as a function of $t^{-1/2}$. CA was used to measure the surface areas of the working electrodes, diffusion coefficients of mediators, Trolox, and α-tocopherol in this research. The charge is the integral of the current with respect to time. As shown in Figure 1.1 C, the CC response was collected by the CC technique using a CHi660c electrochemical workstation in our research group. Similarly, the charge vs. time curve is described by Anson Equation:[35]

$$Q = \frac{2nFAC_\circ \sqrt{D_\circ t}}{\sqrt{\pi}} + Q_c + Q_{ads}$$

Equation 1.4

where Q_c is the charge following into the interfacial capacitance when the electrode potential is stepped from **Initial E** to **First step E**. Q_{ads} is the extra charge produced by the adsorbed species on the electrode surface. The quantity of adsorbed species can be calculated by Equation 1.5[35]:

$$Q_{ads} = nF\Gamma$$

Equation 1.5

where Γ is the surface coverage of the adsorbed species (mole/cm^2). The linear relationship between Q and $t^{1/2}$ is widely used in a variety of electrochemical measurements.

In chapter 2, the "duck" shaped cyclic voltammograms of three mediators ($Mo(CN)_8^{3-}$, $IrCl_6^{2-}$, $Fe(phen)_3^{3+}$) were obtained because these electroactive molecules undergo electrochemically reversible processes. In the presence of GSH, the voltammograms were more challenging to interpret since chemical reactions are coupled to the electron transfer reactions. In

chapter 3, Trolox and oxidized products were adsorbed onto the surface of the GC electrode in aqueous solutions. Chronocoulometry was used to calculate the surface coverage values of the adsorbed species. After the $-2e^-/-H^+$ proton-coupled electron transfer process of phenols, as shown in chapters 3 and 4, chemical decomposition reactions happened to the intermediate phenoxonium ions. Adsorption and coupled chemical reactions affect the shapes of experimental voltammograms. Digital simulation is a useful method for testing the validity of the proposed electrochemical reaction mechanisms of the oxidation of antioxidants in this work. The associated rate constants and thermodynamic information can be extracted from the simulation results. In the next section, the process of using DigiElch7 to simulate a cyclic voltammogram of the redox pair $Mo(CN)_8^{3-}/ Mo(CN)_8^{4-}$ is described.

1.3.3 Digital simulations of experimental cyclic voltammograms using DigiElch 7

Digital simulations of experimental voltammograms were performed using the DigiElch 7 software package. The theoretical basis of this software has been described extensively in previous published reports.[36][37][38][39][40] The simulation process can be used to test the proposed mechanisms by fitting all the thermodynamic and kinetic parameters until a close match to the experimental CV is obtained. Moreover, a fundamental knowledge of the electrochemical reactions and coupled chemical reactions involved in the electrolytic solution is required to evaluate the simulation results.

As shown in Scheme 1.5, the proposed mechanism and the related thermodynamic and kinetic parameters were entered into the software to simulate an experimental voltammogram of the redox couple $Mo(CN)_8^{3-}/ Mo(CN)_8^{4-}$. "Ox" represents the oxidized form of a redox couple, $Mo(CN)_8^{3-}$, and "Red" corresponds to the reduced form $Mo(CN)_8^{4-}$. "e" is used to represent one
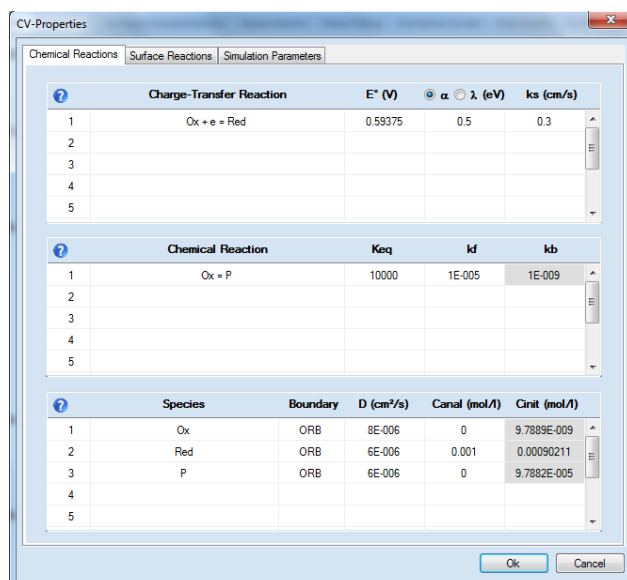
Scheme 1.5 Chemical reaction window of DigiElch 7. Reproduction authorized by ElchSoft.

electron. The sign "=" represents a reaction at equilibrium. "P" is used to represent any products formed in the solution. The reaction of "Ox + e = Red" shows the heterogeneous electron transfer reaction of the redox couple happened on the surface of a working electrode. "Ox = P" shows the homogeneous chemical reaction of $Mo(CN)_8^{3-}$ happened in the solution. The number of charge-transfer reactions and chemical reactions entered into the simulation software depends on the complexity of the proposed mechanism. E° was initially approximate from the experimental data as the half-way potential ($E_{1/2} = (E_{pa} + E_{pc})/2$). The transfer coefficient (α) has a typical value 0.5.[28] The heterogeneous rate constant k_s (cm/s) was estimated using the method of Nicholson.[41] According to Nicholson et.al, The CV's are functions of the parameter ψ, defined by Equation 1.6:[41]

$$\psi = \frac{k_s}{(\pi D f v)^{1/2}}$$ Equation 1.6

where, f = F/RT = 38.92 V^{-1}, and ν is the scan rate. The diffusion coefficient values of the oxidant and other produced forms are assumed to be pretty close. The value of ψ is determined

17

by the current peak difference (ΔE_p) for the reversible one-step, one-electron process.[41] [28] C_{anal} represents the initial concentrations of the reactants. The unknown equilibrium contant (K_{eq}) and forward rate constant (k_f) were allowed to vary iteratively while adjusting the simulation parameters.
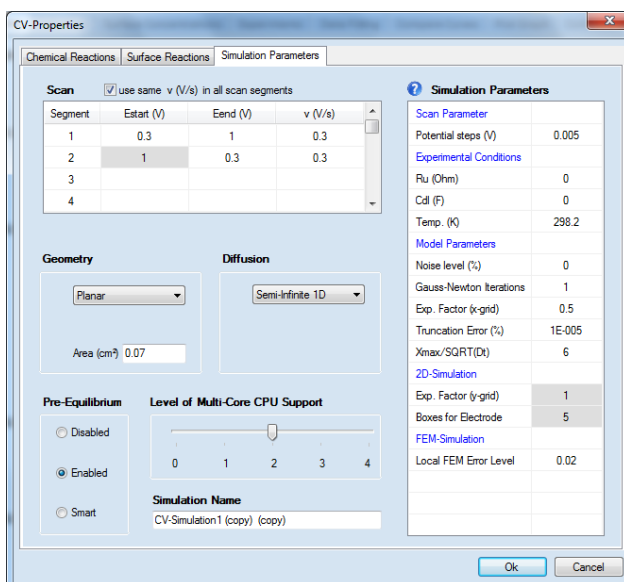
Scheme 1.6 Simulation parameters window of DigiElch 7. Reproduction authorized by ElchSoft.

In Scheme 1.6, the scan rate and potential range parameters had the same values as used in performing voltammetric experiments. The area of the working electrode was calculated by CA and CC techniques. Since the diameter of the working electrode was approximately 3 mm, planar geometry, and a semi-infinite 1D diffusion mode were choosen. The other parameters were set by the DigiElch software as default values to start the simulation. Once all the parameters required by the software were entered and the experimental CV was imported, the simulation process was ready to run. The simulated (black circles) and experimental (green lines) CV's appeared to be overlaid, as shown in Scheme 1.7. Before obtaining a close match, small changes can be applied to the calculated or previously known parameters; larger changes are

used to adjust an unknown equilibrium and rate constants. This procedure continued until a good agreement of the magnitude of the peak current and the position of the peak potential were obtained. To obtain the optimal kinetic and electrochemical parameters, one set of simulated parameters has to match all the experimental cyclic voltammograms over a range of scan rates.
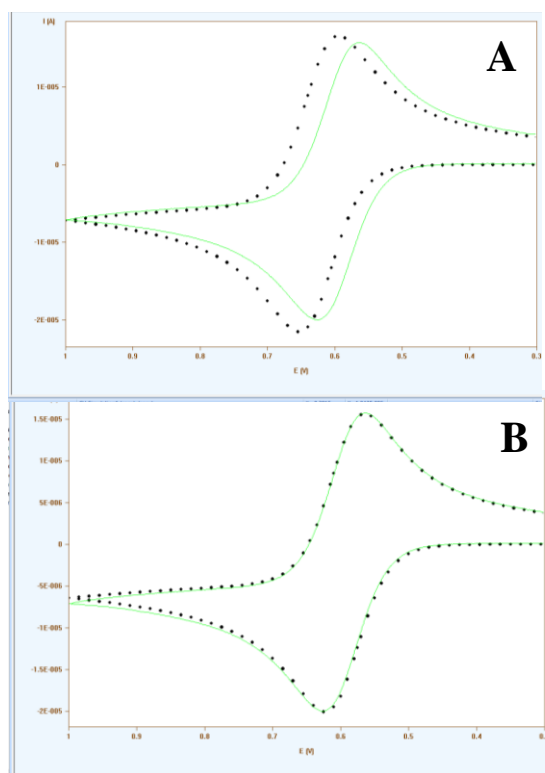
Scheme 1.7 Simulation window of DigiElch 7. Green lines show the experimental CV's and black circles represent simulated CV's. A: before obtaining a good fit; B: final good fit.

1.4 List of references

1.   Migliore, A.; Polizzi, N. F.; Therien, M. J.; Beratan, D. N., Biochemistry and Theory of Proton-Coupled Electron Transfer. *Chem. Rev.* **2014,** *114* (7), 3381-3465.

2.   Hammes-Schiffer, S.; Stuchebrukhov, A. A., Theory of Coupled Electron and Proton Transfer Reactions. *Chem. Rev.* **2010,** *110* (12), 6939-6960.

3.   Meyer, T. J.; Huynh, M. H. V.; Thorp, H. H., The possible role of proton-coupled electron transfer (PCET) in water oxidation by photosystem II. *Angew. Chem.-Int. Edit.* **2007,** *46* (28), 5284-5304.

4.   Warren, J. J.; Tronic, T. A.; Mayer, J. M., Thermochemistry of Proton-Coupled Electron Transfer Reagents and its Implications. *Chem. Rev.* **2010,** *110* (12), 6961-7001.

5.   Madej, E.; Wardman, P., The oxidizing power of the glutathione thiyl radical as measured by its electrode potential at physiological pH. *Arch. Biochem. Biophys.* **2007,** *462* (1), 94-102.

6.   Alligrant, T. M.; Hackett, J. C.; Alvarez, J. C., Acid/base and hydrogen bonding effects on the proton-coupled electron transfer of quinones and hydroquinones in acetonitrile: Mechanistic investigation by voltammetry, H-1 NMR and computation. *Electrochim. Acta* **2010,** *55* (22), 6507-6516.

7.   Hammes-Schiffer, S., Theory of Proton-Coupled Electron Transfer in Energy Conversion Processes. *Accounts Chem. Res.* **2009,** *42* (12), 1881-1889.

8.   Mayer, J. M., Proton-coupled electron transfer: A reaction chemist's view. *Annu. Rev. Phys. Chem.* **2004,** *55*, 363-390.

9.   Sjodin, M.; Ghanem, R.; Polivka, T.; Pan, J.; Styring, S.; Sun, L. C.; Sundstrom, V.; Hammarstrom, L., Tuning proton coupled electron transfer from tyrosine: A competition between concerted and step-wise mechanisms. *Phys. Chem. Chem. Phys.* **2004,** *6* (20), 4851-4858.

10.   Nekrassova, O.; Kershaw, J.; Wadhawan, J. D.; Lawrence, N. S.; Compton, R. G., Oxidation of cysteine by electrogenerated octacyanomolybdate(v). *Physical Chemistry Chemical Physics* **2004,** *6* (6), 1316-1320.

11.   Forman, H. J.; Zhang, H. Q.; Rinna, A., Glutathione: Overview of its protective roles, measurement, and biosynthesis. *Mol. Asp. Med.* **2009,** *30* (1-2), 1-12.

12.   Medina-Ramos, J.; Oyesanya, O.; Alvarez, J. C., Buffer Effects in the Kinetics of Concerted Proton-Coupled Electron Transfer: The Electrochemical Oxidation of Glutathione Mediated by IrCl6 (2-)at Variable Buffer pK(a) and Concentration. *J. Phys. Chem. C* **2013,** *117* (2), 902-912.

13.   Niki, E.; Noguchi, N., Dynamics of antioxidant action of vitamin E. *Accounts of Chemical Research* **2004,** *37* (1), 45-51.

14.   Wang, X. Y.; Quinn, P. J., The location and function of vitamin E in membranes (review). *Mol. Membr. Biol.* **2000,** *17* (3), 143-156.

15.   Burton, G. W.; Ingold, K. U., Buffer Effects in the Kinetics of Concerted Proton-Coupled Electron Transfer: The Electrochemical Oxidation of Glutathione Mediated by IrCl6 (2-)at Variable Buffer pK(a) and Concentration. *Accounts of Chemical Research* **1986,** *19* (7), 194-201.

16.   Boscoboinik, D.; Szewczyk, A.; Hensey, C.; Azzi, A., Reply to "Comment on 'Buffer Effects in the Kinetics of Concerted Proton-Coupled Electron Transfer: The Electrochemical Oxidation of Glutathione Mediated by IrCl6 (2-) at Variable Buffer pK(a) and Concentration". *J. Biol. Chem.* **1991,** *266* (10), 6188-6194.

17.   Traber, M. G.; Arai, H., Molecular mechanisms of vitamin E transport. *Annu. Rev. Nutr.* **1999,** *19*, 343-355.

18.   Ricciarelli, R.; Zingg, J. M.; Azzi, A., The 80th anniversary of vitamin E: Beyond its antioxidant properties. *Biological Chemistry* **2002,** *383* (3-4), 457-465.

19.   Brown, D. A.; London, E., Structure and origin of ordered lipid domains in biological membranes. *J. Membr. Biol.* **1998,** *164* (2), 103-114.

20.   Peng, H. M.; Choules, B. F.; Yao, W. W.; Zhang, Z. Y.; Webster, R. D.; Gill, P. M. W., Long-lived radical cations as model compounds for the reactive one-electron oxidation product of vitamin E. *Journal of Physical Chemistry B* **2008,** *112* (33), 10367-10374.

21.   Peng, H. M.; Webster, R. D., Investigation into phenoxonium cations produced during the electrochemical oxidation of chroman-6-ol and dihydrobenzofuran-5-ol substituted compounds. *J. Org. Chem.* **2008,** *73* (6), 2169-2175.

22.   Lee, S. B.; Lin, C. Y.; Gill, P. M. W.; Webster, R. D., Transformation of alpha-tocopherol (vitamin E) and related chromanol model compounds into their phenoxonium ions by chemical oxidation with the nitrosonium cation. *J. Org. Chem.* **2005,** *70* (25), 10466-10473.

23.   Yue, Y. N.; Novianti, M. L.; Tessensohn, M. E.; Hirao, H.; Webster, R. D., Optimizing the lifetimes of phenoxonium cations derived from vitamin E via structural modifications. *Organic & Biomolecular Chemistry* **2015,** *13* (48), 11732-11739.

24.   Webster, R. D., New insights into the oxidative electrochemistry of vitamin E. *Accounts of Chemical Research* **2007,** *40* (4), 251-257.

25.   Miller, N. J.; Riceevans, C.; Davies, M. J.; Gopinathan, V.; Milner, A., A Novel Method for Measuring Antioxidant Capacity and Its Application to Monitoring the Anioxidant Status in Permature Neonates. *Clinical Science* **1993,** *84* (4), 407-412.

26.   van den Berg, R.; Haenen, G.; van den Berg, H.; Bast, A., Applicability of an improved Trolox equivalent antioxidant capacity (TEAC) assay for evaluation of antioxidant capacity measurements of mixtures. *Food Chemistry* **1999,** *66* (4), 511-517.

27.   Erel, O., A novel automated direct measurement method for total antioxidant capacity using a new generation, more stable ABTS radical cation. *Clinical Biochemistry* **2004,** *37* (4), 277-285.

28.   Bard, A. J.; Faulkner, L. R., Electrochemical methods : fundamentals and applications. 2nd ed.. ed.; New York : Wiley: 2001; p 833.

29.   Elgrishi, N.; Rountree, K. J.; McCarthy, B. D.; Rountree, E. S.; Eisenhart, T. T.; Dempsey, J. L., A Practical Beginner's Guide to Cyclic Voltammetry. *Journal of Chemical Education* **2018,** *95* (2), 197-206.

30.   Hendel, S. J.; Young, E. R., Introduction to Electrochemistry and the Use of Electrochemistry to Synthesize and Evaluate Catalysts for Water Oxidation and Reduction. *Journal of Chemical Education* **2016,** *93* (11), 1951-1956.

31.   Heinze, J., Ultramicroelectrodes in Electrochemistry. *Angew. Chem.-Int. Edit.* **1993,** *32* (9), 1268-1288.

32.   Heinze, J., Cyclic Voltammetry - Electrochemical Spectroscopy. *Angew. Chem.-Int. Edit. Engl.* **1984,** *23* (11), 831-847.

33.   Gerischer, H.; Scherson, D. A., On the Shape of the Cyclic Voltammetry Peaks of Species Irreversibly Adsorbed on Electrode Surfaces. *J. Electroanal. Chem.* **1985,** *188* (1-2), 33-38.

34.   Lee, G. Y.; Park, J. H.; Chang, Y. W.; Cho, S.; Kang, M. J.; Pyun, J. C., Chronoamperometry-Based Redox Cycling for Application to Immunoassays. *ACS Sens.* **2018,** *3* (1), 106-112.

35.   Yamada, A., Charge of adsorbates determined by chronocoulometry. *Denki Kagaku* **1998,** *66* (2), 157-162.

36.   Rudolph, M., Digital simulations on unequally spaced grids. Part 2. Using the box method by discretisation on a transformed equally spaced grid. *J. Electroanal. Chem.* **2003,** *543* (1), 23-39.

37.   Rudolph, M., Digital simulations on unequally spaced grids. Part 1. Critical remarks on using the point method by discretisation on a transformed grid. *J. Electroanal. Chem.* **2002,** *529* (2), 97-108.

38.   Rudolph, M., Attaining exponential convergence for the flux error with second- and fourth-order accurate finite-difference equations. Part 3. Application to electrochemical systems comprising second-order chemical reactions. *J. Comput. Chem.* **2005,** *26* (11), 1193-1204.

39.   Rudolph, M., Attaining exponential convergence for the flux error with second- and fourth-order accurate finite-difference equations. I. Presentation of the basic concept and application to a pure diffusion system. *J. Comput. Chem.* **2005,** *26* (6), 619-632.

40.   Ijsseling, F. P., Electrochemical Methods in Crevice Corrosion Testing - Report Prepared for the European-Fedration-of-Corrosion-Working-Party Physicochemical Testing Methods of Corrosion- Fundamentals and Applications. *British Corrosion Journal* **1980,** *15* (2), 51-69.

41.   Nicholson, R. S., Theory and Application of Cyclic Voltammetry for Measurement of Electrode Reaction Kinetics. *Analytical Chemistry* **1965,** *37* (11), 1351-+.

Chapter 2: Interplay of proton and electron transfer to determine concerted behavior in the proton-coupled electron transfer of glutathione oxidation

2.1 Abstract

Glutathione (GSH), whose thiol group dictates its redox chemistry, oxidizes to the thiyl radical (GS$^\bullet$), which rapidly dimerizes to GSSG. Previously, we found that the oxidation rate of GSH by $IrCl_6^{2-}$ depends on the base (B) concentration and the pK_a of its conjugate acid BH^+, so the concerted pathway GSH + $IrCl_6^{2-}$ + B = GS$^\bullet$ + $IrCl_6^{3-}$ + BH^+ was proposed as the rate determining step. In the current study, this investigation was extended to include oxidant-base pairs that could be used to obtain apparent exothermic and endothermic values of $^{app}\Delta G^{\circ}{}'$ for electron transfer (ET) and proton transfer (PT). The experiments were conducted by electrochemical mediation, whereby GSH reacts with the electrogenerated oxidant M^+ and the mechanism is inferred from digital simulations. When the oxidant-base pair coincide to furnish the most thermoneutral ET, $^{app}\Delta G^{\circ}{}'_{ET} = 0$, the concerted pathway appears to be the primary pathway, whereas the further $^{app}\Delta G^{\circ}{}'_{ET}$ gets from zero, the stepwise pathways seem to be more common. This work supports the prevailing notion that conditions that stabilize charged intermediates of ET or PT lead to stepwise reactions, but concerted pathways occur when those intermediates are unstable. Understanding the interplay between ET and PT will help in designing catalysts for energy harvesting processes that rely on proton-coupled electron transfer.

2.2 Introduction

Proton-coupled electron transfer (PCET) is a type of reaction that involves the occurrence of a proton transfer (PT) and an electron transfer (ET) in coupled fashion, such that they can take

place in consecutive steps (PT-ET, ET-PT), or in a single kinetic event known as concerted proton-electron transfer (CPET).[1][2][3][4][5][6][7] These reactions underlie processes that convert low-energy content molecules into high-energy products for metabolic functions, such as photosynthesis and respiration.[8][9] Concerted pathways in such natural processes increase efficiency by avoiding charged intermediates with high energy that otherwise would appear in the corresponding stepwise mechanisms.[10][11][12][13] Chemical conversions like CO_2 and O_2 reduction, which are technologically relevant for producing renewable energy, also rely on PCET, but implementing the advantage of concerted mechanisms in such systems has not been as effective as in nature. In part, this is because despite significant strides made since the first report suggesting PCET as a unique type of transfer,[14] understanding all the factors that affect the interplay between PT and ET control PCET reactivity still remain unclear. In this research, we studied the oxidation kinetics of the natural thiol, glutathione (GSH), under conditions that yielded both the apparent exothermic and endothermic values of $^{app}\Delta G^{\circ'}_{ET}$ for ET and PT using oxidants and bases that respectively had appropriate redox potentials and pK_a values. The goal in this case was to understand the ways in which ET and PT affect each other to dictate either a concerted or a stepwise mechanism.
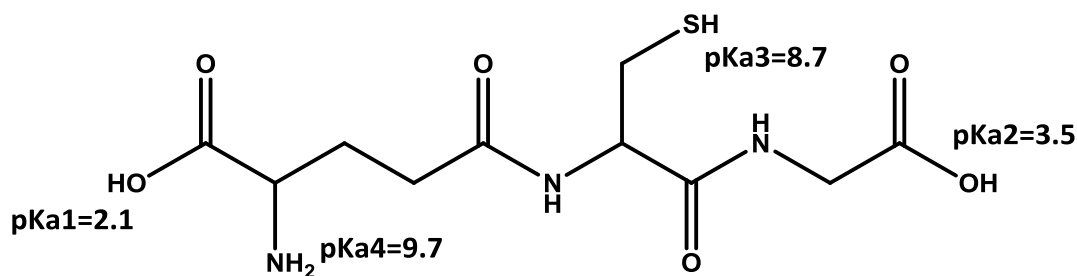
Scheme 2.1 GSH with pK_a values

Glutathione is a tripeptide (Scheme 2.1) made of the aminoacids glutamate, cysteine and glycine, with the thiol group of the cysteine residue dominating the redox chemistry of GSH and

displaying a pK_{aSH} of 8.7. The other three proton-active groups, two carboxylates (pK_{a1} = 2.1 and pK_{a2} = 3.5) and one amine (pK_{a4} = 9.7), convey a net charge (-1, -2 or -3) to GSH that depends on the pH. Previously we studied the oxidation of GSH by the electrogenerated mediator $IrCl_6^{2-}$, which initially produces the thiyl radical GS$^•$, that in turn dimerizes into GSSG in a diffusion limited rate.[15] [16] The key findings of that work, can be summarized as follows: first, the kinetic control of the rate determining step (RSD) was dictated by the concentration of GSH, $IrCl_6^{2-}$ and the base (B) in the buffer system (B/BH$^+$). Second, the reaction exhibited a Bronsted linear relationship between the observed rate-constant k_{obs} and the pK_a of the conjugate of acid BH$^+$, displaying higher rates with stronger bases. Third, consistent with a degree of concerted mechanism, a kinetic isotope effect (KIE) that declined when an increasing buffer concentration was detected. This signaled the occurrence of stepwise pathways. Finally, the influence of B in the RDS was also corroborated when the sluggish oxidation of GSH in dilute buffer was speeded up by electrochemically recycling the mediator during fast voltammetric scans (Scheme 2.2).
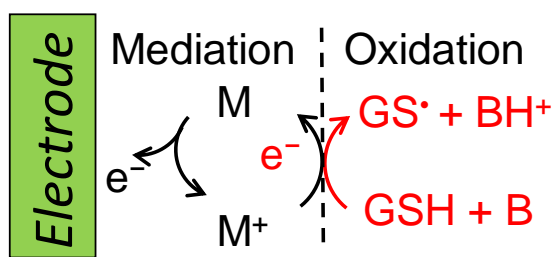
Scheme 2.2 Mediated oxidation of GSH

In the light of such evidence and aided by digital simulations, we proposed the concerted reaction GSH + B + $IrCl_6^{2-}$ = GS$^•$ + BH$^+$ + $IrCl_6^{3-}$, including some contribution from the stepwise pathway, to be the RDS. The buffers studied had pK_a < pK_{aSH} in the range of pH 5.0 to

7.0.[15][16] In this work, we extended this investigation by comparing several oxidants of varying redox potentials ($E_M^{°'}$), which were generated electrochemically and acted as mediators ($M^+ = Mo(CN)_8^{3-}$, $IrCl_6^{2-}$, $Fe(bpy)_3^{3+}$, $Fe(phen)_3^{3+}$) to oxidize GSH (Scheme 2.2). The comparison also included buffers of pK_a above and below pK_{aSH} in the range of pH 4.76 to 10.0. Because GSH does not react directly at the electrode but primarily with M^+ through ET mediation (Scheme 2.2), the kinetics of the reaction can be easily extracted from digital simulations of experimental cyclic voltammograms.

2.3 Experimental Section

2.3.1 Reagents and Materials

L-Glutathione reduced (L-GSH, Sigma-Aldrich, ≥ 98.0%), potassium octacyanomolybdate(IV) hydrate ($K_4Mo(CN)_8$, Aldrich, 99.99%), sodium chloride (NaCl, Fluka, ≥ 99.999%), sodium phosphate dibasic (Na_2HPO_4, Fluka, 99.999%), sodium phosphate monobasic (NaH_2PO_4, Fluka, 99.999%), sodium acetate (CH_3COONa, Fluka, 99.999%), sodium hydroxide (NaOH, Aldrich, 99.9%), hydrochloric acid (HCl, Fisher Scientific, 37.5%), deuterium oxide (D_2O, Acros Organics, 99.8 atom % D), sodium deuteroxide (NaOD, Aldrich, 40 wt. % solution in D_2O, 99+ atom % D), deuterium chloride (DCl, Aldrich, 35 wt. % solution in D_2O, 99 atom % D), and potassium dideuterium phosphate (KD_2PO_4, Aldrich, 98 atom % D) were all used as supplied without further purification. Tris(1,10-phenantroline) iron (II) sulfate ($Fe(phen)_3SO_4$) was synthesized according to reported literature procedures.[17] Deionized water (DI) with a resistivity of 18.2 MΩ cm was purified with a Millipore ultrapure water purification system (Billerica, MA) and used to prepare all aqueous solutions. The pH of all solutions was measured with a Fisher Science Education pH meter (pH/Ion 510), calibrated with pH 7.00 ±

0.01, 4.00 ± 0.01, 10.00 ± 0.01 buffers (RICCA Chemical Company, Arlington, TX). The Henderson-Hasselbalch equation was used to calculate the concentration of buffer components. The desired pH was adjusted using diluted NaOH and/or HCl. For deuterated experiments, deuterated phosphate buffer solutions were prepared by mixing KD_2PO_4 and D_2O. Diluted NaOD and DCl were used to attain the desired pD. The formula pD = pH + 0.4 was used to convert the measured pH by pH meter (pH/Ion 510) to pD.[18]

2.3.2 Electrochemical Methods

All cyclic voltammetry experiments were performed in a 10 mL glass cell using a potentiostat (CH Instruments, Austin, TX), and a three-electrode cell equipped with a glassy carbon (GC) working electrode (area = 0.07 cm^2), a Pt-wire counter electrode, and Ag/AgCl reference electrode (1.0 M NaCl). Cyclic voltammograms (CV's) were recorded by monitoring the system responses. All solutions were deaerated with nitrogen for 15 minutes before measurements and with headroom deoxygenation continued throughout the experiments. The GC electrode was polished with a mixture of 0.05 μm alumina and DI water over a Buehler cleaning pad (Lake Bluff, Illinois), and rinsed with DI water before experiments. The reference electrode Ag/AgCl and the counter electrode Pt-wire were purchased from CH Instruments (Austin, TX). Working solutions contained a mixture of the metal and GSH dissolved in 10.00 mL of x M aqueous buffer, adding NaCl to maintain an ionic strength of 1.0 M. Such a high concentration of supporting electrolyte was used to mitigate double layer effects (Debye length^{-1} for 1.0 M is 3.0 Å),[19] and minimize the influence on activity coefficients, by maintaining a high baseline of ionic strength. All rate constants in this work are apparent (not corrected for double layer effects), however the impact from reactant additions (< 10% of 1.0 M) in kinetic measurements, was expected to be small and constant because in some cases the effect is systematic, as with ions of

similar charge ($Mo(CN)_8^{3-}$ and $IrCl_6^{2-}$ or $Fe(bpy)_3^{3+}$ and $Fe(phen)_3^{3+}$). In sequence, a background scan of the buffer was collected first, a scan of the buffer with metal complex, and then a scan of buffer with metal complex and L-GSH. All the CV's were background subtracted and recorded at room temperature ($\sim23 \pm 1$ °C) with an inert atmosphere during experiments.

2.3.3 Digital Simulation

Digital simulations were performed using DigiSim™ version 3.03 (Bioanalytical Systems, Inc., West Lafayette, IN). Tables 1 and 2 show the mechanisms that were entered in Digisim™.[15] The key parameters that mattered the most to match the electrochemical peak potentials and currents in the experimental CV's are also listed on the Tables and a corresponding description of their source is presented below. However, all thermodynamic, kinetic and diffusion constants used for simulations are listed in Appendix as supporting information. Initially, unknown equilibrium and rate-constants (i.e. K_4 , K_5 and k_{obs}, k_{s3}, k_{f4}, k_{f5} in Table 2.1) were allowed to vary iteratively while keeping one of them constant at a time, until a close match to the experimental CV was obtained. This procedure continued until a satisfying agreement of peak potentials and currents with the experimental CV was attained and was consistent at all the scan rates probed. For a particular buffer-mediator-GSH combination, CV's at five scan rates from 0.1 to 1.0 V s^{-1}, were recorded and the fitted parameters were reported as averages with variations at each scan rate reported as standard deviations. The diffusion coefficient for GSH (D_{GSH}) in D_2O was measured by Pulsed Gradient Echo experiments on a Varian Inova 400 MHz NMR at 25 °C as done previously.[15][20] The average D_{GSH} after correction for viscosity was 5.13 ± 0.05 x 10^{-6} cm^2 s^{-1} , and the same value was used for GS$^-$ and GS$^{\bullet}$. Values for $D_{M/M}{}^+$, determined from fitted CV's of the pure mediator were comparable to those found in the literature.[21][22][23][24]

Table 2.1 Concerted mechanism

Eq.	Reaction	Parameter
1	$M = M^+ + e^-$	$E_1^{\circ\prime}$, k_{s1}, D_M
2	$(GSH + B) + M^+ = M + (GS^{\bullet} + BH^+)$	k_{obs}, D_{GSH}, K_2
3	$GSH = GSH^{\bullet} + e^-$	k_{s3}, $E_3^{\circ\prime}$
4	$GS^{\bullet} + GS^{\bullet} = GSSG$	K_4, k_{f4}
5	$GS^{\bullet} + M^+ = M + GS^*$	K_5, k_{f5}
6	$M^+ = P$	K_6, k_{f6}

Table 2.2 Stepwise mechanism

Eq.	Reaction	Parameter
2a	$GSH + B = BH^+ + GS^-$	K_{2a}, k_{f2a}
2b	$GS^- + M^+ = M + GS^{\bullet}$	K_{2b}, K_{f2b}, D_{GSH}
3a	$GS^- = GS^{\bullet} + e^-$	k_{s3a}, $E_{3a}^{\circ\prime}$

2.4 Results and Discussion

2.4.1 Mechanistic pathways

For the concerted mechanism, the six reactions listed in Table 2.1 were considered. Reaction 1 is the oxidation of mediator M at the electrode with electrochemical parameters, $E_1^{\circ\prime}$ (standard redox potential) and k_{s1} (heterogeneous rate-constant), which were determined from fitted experimental CV's of M solution under the corresponding conditions. Reaction 2 represents the concerted homogeneous oxidation of GSH by the electrogenerated mediator M^+. The rate-constant in the forward direction of reaction 2, was regarded as $k_{obs} = k_B [B]$ (depending

on buffer concentration and pH), and k_B is the forward rate-constant for the concerted reaction with respect to B. Therefore, each fitted CV provided a value of k_{obs} for a particular ratio of [B]/[BH$^+$]. Given that, at 25 °C K = $10^{nE°/0.059}$, K$_2$ was calculated from E$_2$°' by Digisim^{TM} once E$_1$°' and E$_3$°' were entered.

$$E_{app}^{\circ}(GS^{\bullet}, H^+/GS^-) = E^{\circ}(GS^{\bullet}/GS^-) + 0.059 \log\left(1 + \frac{H^+}{K_{aSH}}\right) \qquad \text{Equation 2.7}$$

The values of E3°' at different pH values were calculated using Equation 2.7, as reported by Madej,[25] who showed that in buffered solution, the apparent redox reduction potential (E°$_{app}$) for GS$^{\bullet}$,H$^+$/GSH, follows a pH Nernstian behavior with an approximate slope of ~0.06 V/ pH-unit in the pH range 3.0 to 8.0. This slope becomes 0 V/ pH-unit above pH ~10.0 when all functional groups in GSH are deprotonated and then E°$_{app}$ = E°(GS$^{\bullet}$/ GS$^-$). We used pK$_{aSH}$ = 8.7 and E°(GS$^{\bullet}$/GS$^-$) = 0.8 V vs NHE (0.58 V vs Ag/AgCl), which were the values employed by Madej as well.[25] Reaction 3 is the electrochemical oxidation of GSH directly at the electrode, which made a marginal contribution to the current and was added in some cases because, although control experiments showed no voltammetric peaks, modest amounts of current were still detected in pure GSH solution. Reaction 4 is the radical dimerization where GSSG denotes the dimer. Reaction 5 accounts for parallel oxidation pathways of the thiyl radical to produce "overoxidation" species (G*) with higher oxidation states of sulfur.[26][27] This reaction has been reported to occur when thiols are oxidized by metal complexes. [26][27] Reaction 6, in which P represents degradation products, takes into account low yield decomposition of the metal complexes used as mediators in this study.[22][24] The parameters for reaction 6 were estimated from fitted CV's of the mediator solutions under the corresponding conditions.

Table 2.2 shows the PT-ET steps that replaced concerted reaction 2 in Table 2.1. The equilibrium constant K_{2a} was calculated with pK_a values for GSH and BH^+, but k_{f2a} was allowed to be fit. Equilibrium constant K_{2b} was automatically set by DigiSim^{TM} once the values of $E_1^{\circ'}$ and $E_4^{\circ'}$ were entered. For reaction 3a, $E_{3a}^{\circ'}$ ($GS^{\bullet}/GS^-$) was set to the value reported by Madej.[25] The rest of the reactions were 1, 4, 5, and 6 in Table 2.1.

2.4.2 Experimental results simulated with concerted mechanism

Best fits to experimental cyclic voltammograms (CV's) in the range of pH values below pK_{aSH} (8.7) were obtained with the reactions of the concerted mechanism listed in Table 2.1, with Reaction 2 being the concerted RDS followed by the fast dimerization of the thiyl radical (Reaction 4, Table 2.1).

In addition to the fact that self-annihilation reactions of sulfur radicals are known to be diffusion controlled,[28] other studies have revealed that production of the thiyl radical in Reaction 2 (Table 2.1) is also the RDS for chemical oxidations of GSH by $IrCl_6^{2-}$ and other inorganic oxidants.[29] Parallel pathways of $GS^{\bullet}$ leading to products of higher oxidation states of sulfur (Reaction 5, Table 2.1), sometimes dubbed as overoxidation, do not invalidate this kinetic model, because the overall kinetics is still controlled by the rate of the RDS. Therefore, a rate law for the oxidation of GSH can be given by Equation 2.8 or 2.9:[15][16]

$$Rate = k_B[B][GSH][M^+] \qquad \text{Equation 2.8}$$

$$Rate = k_{obsB}[GSH][M^+] \qquad \text{Equation 2.9}$$

where k_B is the forward rate constant related to B in the proposed concerted RDS and k_{obsB} is the observed rate constant dependent on [B], $k_{obsB} = k_B[B]$, that is estimated from the experimental

CV's at different pH values (B/BH$^+$ ratios) and/or buffer concentration. The analysis however, should also incorporate other species in the system that can act as proton acceptors, such as water (w), hydroxide ions (OH$^-$), and even BH$^+$.[30] Therefore, the overall k_{obs} should be written as:

$$k_{obs} = k_w[H_2O] + k_{OH}[OH^-] + k_B[B] + k_{BH}[BH^+]$$ Equation 2.10

There will be as many reactions 2 as bases present in solution, with contributions depending on their concentration and the pK$_a$ of their conjugate acids.[31] Given that H$_2$O is such a weak base to deprotonate GSH and that the concentration of OH$^-$ at pH < 7.0 is negligible, their contribution to Equation 2.10 is also very small. For a component B, a plot of k_{obsB} vs [B] is expected to be linear and k_B can be extracted from the slope.[32] Previously, we showed that for the case of phosphate buffer at pH 7.0,[33] such a plot had two linear regions reflecting two slopes that were attributable to H$_2$PO$_4^-$ and HPO$_4^{2-}$, as a result of the pK$_a$ difference for their corresponding conjugated acids.[16] Because of the complication when simulating Reaction 2 with several bases, we only considered one B term in Equation 2.10, which in the end did not change the interpretation of the results.
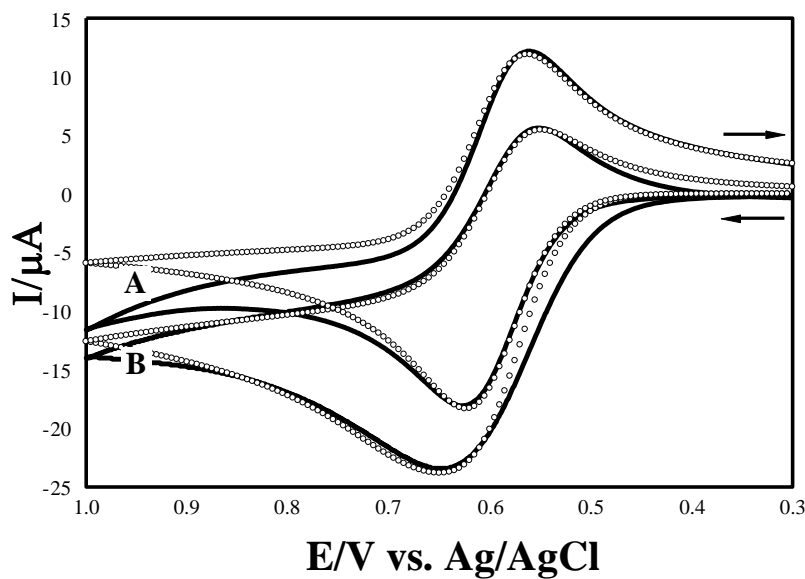
Figure 2.1. Experimental (solid line) and simulated (circles) CV's of 1.00 mM GSH + 1.00 mM Mo(CN)$_8^{4-}$, in the presence of 50.0 mM phosphate buffer at pH 4.76 (A) and 10.0 (B), 1.0 M NaCl (0.1 V s^{-1}).
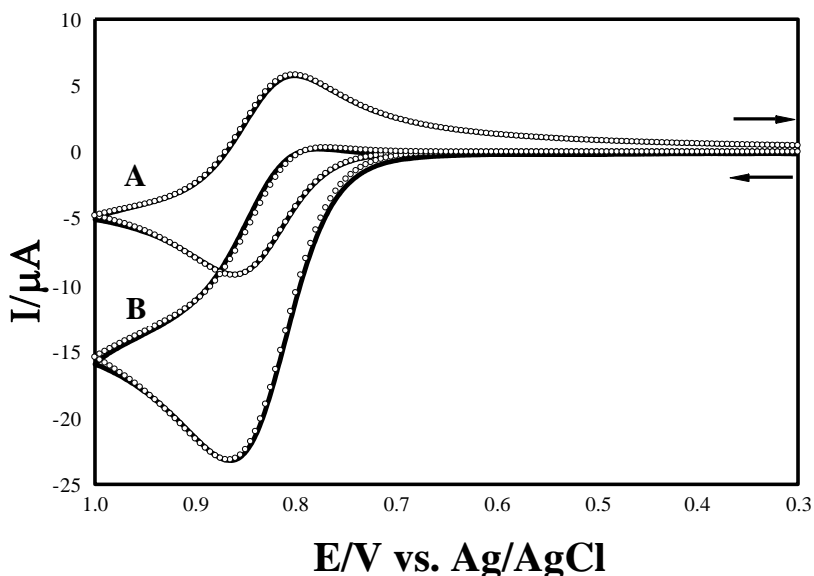
Figure 2.2 Experimental (solid line) and simulated (circles) CV's of 1.00 mM pure Fe(phen)$_3^{2+}$ (A), 1.00 mM GSH + 1.00 mM Fe(phen)$_3$SO$_4$ (B), in 50.0 mM phosphate buffer at pH 4.76, 1.0 M NaCl. Scan rate = 0.1 V s^{-1}.

Figures 2.1 and 2.2 show CV's recorded for the mediated oxidation of GSH by two electrogenerated oxidants, M$^+$, with increasing oxidizing strength at 0.05 M concentration of phosphate buffer at pH 4.76. Each figure displays a CV of the pure mediator M along with a CV for the equimolar (0.001 M) mixture of GSH and M. The superimposed circles represent fitted simulations following the mechanism outlined in Table 2.1. In the forward scan starting at 0.3 V vs Ag/AgCl, the CV's for pure M showed an anodic peak from the oxidation of M to M$^+$, whereas the reduction of M$^+$ back to M appeared as a cathodic peak in the reverse scan. The symmetrical shape of the CV for the pure mediators in each panel confirms that the reversible

conversion M $\leftrightarrow$ M$^+$ was unperturbed and that neither species, M or M$^+$, participated in the solution reactions. In contrast, when GSH was added to M solutions, the scenario was drastically altered and the electrogenerated M$^+$ reacted with GSH (Scheme 2.2) making the peak in the cathodic scan decrease and disappear. At the same time, the extra M produced by way of M$^+$ reacting with GSH, causes an increase in the anodic oxidation peak (Scheme 2.2). All the CV shapes shown throughout this paper are well-documented cases of electrochemical mediation,[19] [32] in which the reaction between generated oxidant M$^+$ and a marginally electroactive substrate (GSH) is the RDS in a subsequent complex mechanism in solution.[32] In fact, such an approach is often used to measure the kinetic reactivity of substrates of interest with standard reversible mediators because the speed of the two-way conversion M $\leftrightarrow$ M$^+$ can be externally controlled with the voltammetric scan rate.[32] Additionally, the rate constant for the reaction between the substrate and M$^+$ can be estimated from the electrochemical current if the CV shape matches one of the two landmark conditions on the kinetic zone diagram established for this case.[32] Three major zones have been identified, the first one being the extreme scenario with no mediation in which the CV looks exactly like for pure M even after adding substrate.[32] The second and third zones involve slow and fast kinetics, respectively, for the RDS in relation to the subsequent reaction path. For either zone, the CV response is a function of two dimensionless parameters, one is the kinetic factor λ, which at 298 K is 0.02569($k C_M°/\nu$), where k is the rate constant of the reaction (k_{obsB}, GSH-M$^+$), ν is the scan rate in V/s, and $C_M°$ is the bulk concentration of M.[32] The second parameter is the excess factor $\gamma = C_{GSH}°/C_M°$, which accounts for which bulk concentration is in excess.[32] Typically one sets experimental conditions by manipulating $C_M°$, $C_{GSH}°$ and ν, so that λ and γ, to produce one of the landmark CV shapes and a representative equation to estimate k (k_{obsB}). However digital simulations allow the same estimate under any

condition (see below).[15] Therefore, the CV shape is a quick diagnostic for determining kinetic effects. Accordingly, the cathodic peak current disappeared when going from $Mo(CN)_8^{3-}$ to $Fe(phen)_3^{3+}$, as shown in Figures 2.1 and 2.2. This is a sign of rate increase. In this
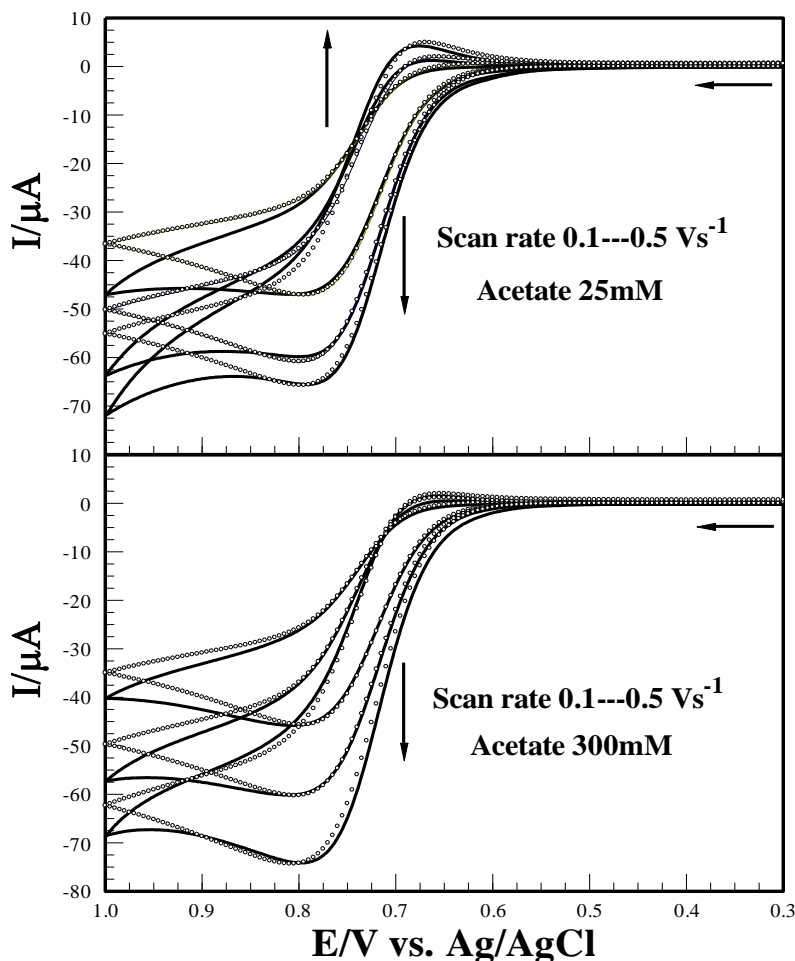
Figure 2.3. Experimental (solid line) and simulated (open circles) CV response for GSH (3.00 mM) + K_3IrCl_6 (1.00 mM) in acetate buffer pH = pK_a=4.76.

situation, the participation of the base in the proposed concerted RDS is verified by slowing down the reaction between GSH and M^+ with dilute buffer, so that the electrochemical conversion $M \leftrightarrow M^+$ ends up outrunning the oxidation of GSH and the cathodic peak of M

reappears at high scan rates. This result was observed with $IrCl_6^{2-}$ in the presence of several dilute buffers with various scan rates (Figure 2.3).[15]
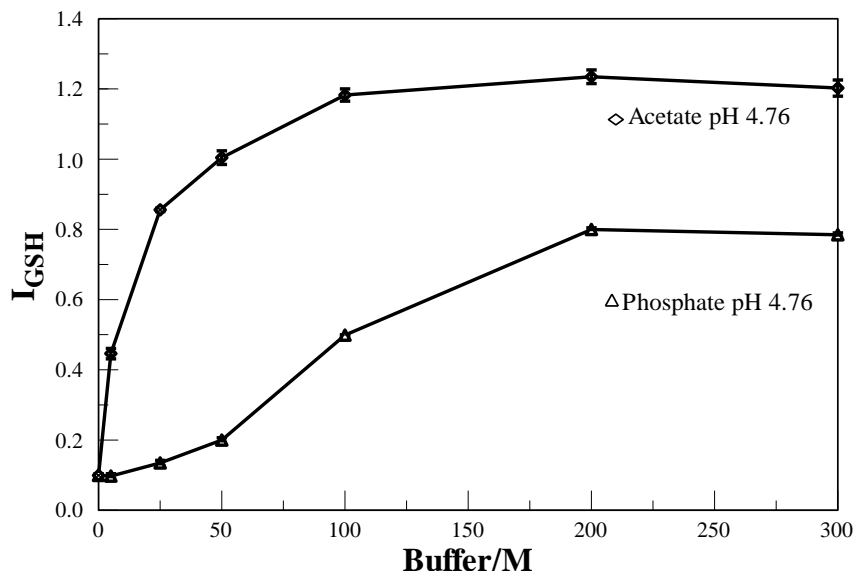
Figure 2.4 I_{GSH} (0.5 Vs^{-1}) for GSH (3.00 mM) + K_3IrCl_6 (1.00 mM) at different concentration of phosphate buffer (99.4% $H_2PO_4^-$, pK_a=2.12) and acetate buffer (50.1% $CH_3CO_2^-$, pK_a=4.76) at pH 4.76.

Figure 2.4 shows the normalized current (I_{GSH}) of the mediated oxidation of GSH by $IrCl_6^{2-}$ in two buffer systems. To illustrate the comparison, the GSH and M concentrations were maintained constant and the pH of the solutions was set to the same value, 4.76. The I_{GSH}, is defined as ($\frac{I_{M-GSH}}{I_M}$ - 1), where $I_{M\text{-}GSH}$ is the oxidation peak current for the mixture of mediator (M) and GSH and I_M is the oxidation peak current for pure M.[15] The parameter I_{GSH} has no units but expresses the increase in the GSH oxidation with respect to the current for the mediator alone. The I_{GSH} for the acetate buffer showed a steeper rise and a higher plateau value than that of the phosphate buffer solutions, indicating an acceleration of the oxidation rate as buffer pK_a increased (pKa $_{H3PO4/H2PO4-}$ = 2.12, pKa $_{CH3COOH/CH3CO-}$ = 4.76). When the buffer concentration was maintained constant at 0.3 M, the simulated forward rate constant for the mediated oxidation

of GSH in acetate buffer was $(7 \pm 2) \times 10^3 \ M^{-1}s^{-1}$, which is larger than that with phosphate buffer $(4.7 \pm 0.2) \times M^{-1}s^{-1}$. In summary, all figures 2.1, 2.2, 2.3 and 2.4, illustrate an acceleration in the oxidation rate of GSH caused by increasing $E_M°'$ and buffer pK_a.

Table 2.3, obtained previously by our research group, exhibits the values for k_{obs} estimated from simulations using the concerted mechanism in Table 2.1 for selected mediators and buffers. It appears that k_{obs}, is ultimately dictated by the interplay between $E_M°'$ and pK_a. This effect can be conveyed more quantitatively by examining the Bronsted plots in Figure 2.5, which are graphical representations of the log of k_{obs} versus the pK_a given by the empirical relationship in Equation 2.11.[30] [31] In this case β is the Bronsted slope; C is a constant with no physical

$$\log k = \beta p K_a + \log C \qquad\qquad \text{Equation 2.11}$$

meaning and k is the reaction rate-constant, which is usually replaced by k_{obs}.[30] [31] After linear regression, the values of β were 0.42 ± 0.02 for $Mo(CN)_8^{3-}$, 0.69 ± 0.05 for $IrCl_6^{2-}$, and 0.92 ± 0.05 for $Fe(phen)_3^{3+}$, indicating that β gradually increases as the oxidant strength of the mediator intensifies. Accordingly, when the malic buffer is replaced by phosphate, entailing a 2 unit pK_a increase, there is a 7-fold rise in k_{obs} for the oxidation with $Mo(CN)_8^{3-}$. However, for $IrCl_6^{2-}$ and $Fe(phen)_3^{3+}$, the increase is 30 and 90-fold, respectively. Therefore, the higher the value of β, the greater the increase in k_{obs} per unit of pK_a and the more effective is B at enhancing the oxidation of GSH. For organic reactions that involve PT in their mechanism, typical values of β range from 0 to 1, and its magnitude is interpreted as the extent of the PT in the transition state of the reaction.[30] [31]Thus, a value of 1 signals that B has completely deprotonated the substrate (GSH) at the transition state, while 0 denotes no deprotonation. Consequently, intermediate values of β

between 0 and 1 reflect intermediate degrees of PT at the transition state. [30] [31]Using this analysis and examining the Bronsted slopes in Figure 2.5, it can be asserted that $IrCl_6^{2-}$ is the oxidant that

Table 2.3 Apparent values of k_{obs} as a function of pK_a and $E°'$

	$Mo(CN)_8^{3-}$	$IrCl_6^{2-}$	$Fe(phen)_3^{3+}$
$E°'/V$	0.583 ± 0.003	0.730 ± 0.006	0.827 ± 0.002
pK_a		$k_{obs} / M^{-1} s^{-1}$	
5.1	$1.1 \pm 0.1 \times 10^3$	$5.0 \pm 0.2 \times 10^3$	$1.10 \pm 0.01 \times 10^5$
5.6	$1.6 \pm 0.2 \times 10^3$	$1.3 \pm 0.1 \times 10^4$	$4.6 \pm 0.1 \times 10^5$
6.2	$3.2 \pm 0.5 \times 10^3$	$4.1 \pm 0.5 \times 10^4$	$1.3 \pm 0.1 \times 10^6$
6.5	$4.6 \pm 0.2 \times 10^3$	$3.7 \pm 0.5 \times 10^4$	$3.0 \pm 0.2 \times 10^6$
7.2	$7.7 \pm 0.4 \times 10^3$	$1.5 \pm 0.2 \times 10^5$	$9.8 \pm 0.6 \times 10^6$
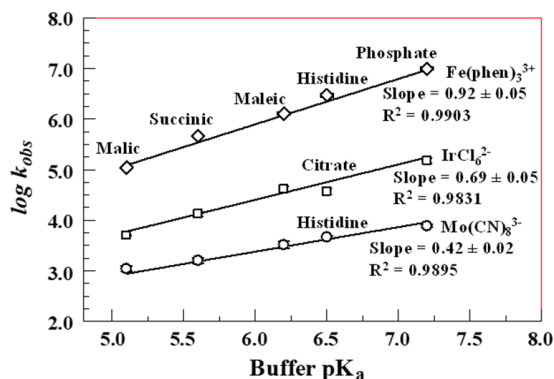
Figure 2.5 Bronsted plots for different mediators

Has the most concerted character in the transition state, whereas $Mo(CN)_8^{3-}$ and $Fe(phen)_3^{3+}$ produce ones with less participation of the concerted pathway. In congruence with this perspective, concerted character contributions have been assigned to base-catalysed nucleophilic reactions that show Bronsted slopes between 0.2-0.8.[33] [34]

2.4.3 Interplay of PT and ET

Not only does the oxidation rate of GSH increase with the strength of the oxidant in the normal region of ET, as predicted by Marcus theory,[35] but also does it increases when a stronger base is present as the proton acceptor. Furthermore, there is a reciprocal effect between PT and ET that boosts the reaction rate, whereby increments in pK_a are more effective with a stronger oxidant and gains in oxidant strength are more efficient in the presence of a stronger base. For instance, when $Mo(CN)_8^{3-}$ was replaced with $Fe(phen)_3^{3+}$ as the oxidant, k_{obs} increased by a factor of ~1272 in the phosphate buffer but only ~100-fold in the malic buffer. Conversely, when replacing malic with phosphate as the buffer, k_{obs} increases by a factor of 89.9 for $Fe(phen)_3^{3+}$ and only 7-fold for $Mo(CN)_8^{3-}$.

2.4.4 Kinetic isotope effect (KIE) at $pK_a < pK_{aSH}$

Table 2.4 KIE in phosphate buffer (PB) pD 7.0

[PB] / M	k_{obsH}/k_{obsD}	
	$Mo(CN)_8^{3-}$	$Fe(phen)_3^{3+}$
0.010	2.53 ± 0.30	2.08 ± 0.14
0.050	1.17 ± 0.10	1.72 ± 0.13

Table 2.4 shows the estimated KIE (k_{obsH}/k_{obsD}) values with two different concentrations of phosphate buffer (PB) at pD 7.0 using mediators $Mo(CN)_8^{3-}$ and $Fe(phen)_3^{3+}$. The KIE values for both mediators were larger than 1.0 confirming the presence of B in breaking the S-H bond in the *transition state* of the RDS.[36] The KIE measured at 298 K for the homolysis of a S-H/S-D bond, whose IR stretches appear at 2524 and 1837 cm^{-1}, respectively,[37] should be approximately 5.4. However, if the S-H bond is only partially broken in the *transition state* or a new bond starts to form, a KIE that is attenuated from this value can be expected.[38] As was found with $IrCl_6^{2-}$, the KIE values decline as the buffer concentration is raised.[39]

In the case of $Mo(CN)_8^{3-}$ the KIE went from 2.53 ± 0.30 to 1.17 ± 0.10 when [PB] was increased from 0.010 to 0.050 M. This effect can be attributed to the parallel pathway PT-ET becoming more prominent as the reaction rate becomes zero order in B.

2.4.5 Stepwise mechanism and KIE at $pK_a > pK_{aSH}$

The best fits to the experimental CV's at pH 10.0 of PB occurred with the stepwise mechanism outlined in Table 2.2, in which the reaction between GSH and M^+ (Reaction 2) is split into the basic PT (Reaction 2a) and ET (Reaction 2b) steps. The forward rate constant k_{f2b} is the *stepwise* ET rate that will be compared with the k_{obs} of the *concerted* mechanisms. Figure 2.6, shows the CV's for the oxidation of GSH in equimolar mixture with M (0.001M) and PB 0.100 M. Only mediators $Mo(CN)_8^{3-}$ and $Fe(phen)_3^{3+}$ were studied because $IrCl_6^{2-}$ exhibited significant decomposition at pH 10.0. The CV shape for a slow reaction between GSH and M^+ is evident with oxidant $Mo(CN)_8^{3-}$, which shows a single anodic peak and a cathodic bump on the reverse scan, revealing the presence of some unreacted M^+. When the scan rate was increased to 0.2 V/s, the cathodic peak grew back because additional M^+ was being freed from the reaction with GSH because the latter cannot keep up at the imposed scan rate. In contrast, $Fe(phen)_3^{3+}$ displayed the split peak characteristic of a rapidly mediated reaction. Moreover, Figure 2.7 shows the addition of excess GSH, so that the reaction became limited by M^+ and the CV shape morphed into the S-shape expected for the kinetic zone when the substrate (GSH) is in excess.[32]

Table 2.**5** Kinetic data for GSH at 0.100 M PB pH 10.0

Oxidant	k_{f2a} /M^{-1} s^{-1}	k_{f2b} /M^{-1} s^{-1}	KIE
$Mo(CN)_8^{3-}$	2.0×10^9	$4.2 \pm 0.7 \times 10^3$	0.44 ± 0.08
$Fe(phen)_3^{3+}$	2.0×10^9	$1.3 \pm 0.4 \times 10^8$	0.85 ± 0.27

Table 2.5 shows the simulated values of k_{f2a}, k_{f2b} and KIE for experiments at pH 10.0 in PB 0.100 M. The major bases making up the system at this pH are ~0.100 M of HPO_4^{2-} (pK_a = 12.6) and ~1.0 x10^{-4} M of OH^- (pK_a = 15.76), therefore GSH is expected to be in a PT equilibrium with almost complete deprotonation of the thiol and only ~1% in the SH form. Although, the oxidation rate of GSH with oxidant $Mo(CN)_8^{3-}$ at pH 10.0, remained in the same order of magnitude as k_{obs} for $pK_a < pK_{aSH}$ (Table 2.3), $Fe(phen)_3^{3+}$ showed a 43-fold increase with a base that has a pK_a of 12.6. The KIE values at pH 10.0 are inverse which due to isotopic substitutions at a site other than the bond breaking site in the rate determining step of the mediated oxidation of GSH.[40] The nature of solvent and GSH interactions may also different by changing H_2O to D_2O. This can change the energy of the transition states during PECT reactions of GSH and leads to the reverse KIE affects, which has been proposed for multistep reactions with fast equilibration preceding the RDS.[36] Such is the present case, given the exothermic character of the PT step from GSH to PO_4^{3-} (or OH^-) and the rapid forward rate constant k_{f2a} (Table 2.5). Even though, the high oxidant strength of $Fe(phen)_3^{3+}$ could facilitate the presence of the intermediate $GSH^{\bullet+}$ to allow the ET-PT route, the expected pK_a (< -1.74, H_3O^+) of the radical cation, limits this option because of the solvent "leveling effect", that does not allow an acid stronger than hydronium ion to exist in water.[15]
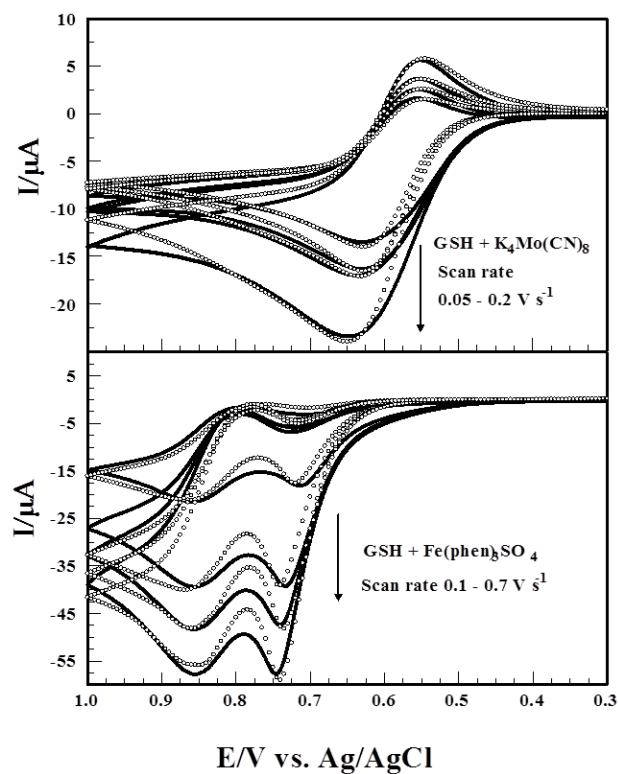
Figure 2.6 Experimental (solid line) and simulated (open circles) CV response of GSH and mediators (0.001 M), in 0.100 M PB pH = 10.0
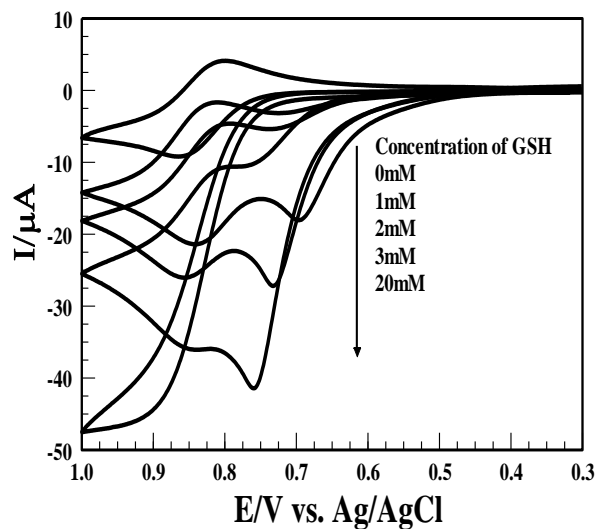
Figure 2.7 CV responses for the mediated oxidation of GSH + 1.0 mM Fe(phen)$_3$SO$_4$ at 100.0mM buffer at pH 10.0. The concentrations of GSH were 0.0, 1.0, 2.0, 3.0, 10.0 and 20.0 mM (0.1 V/s).

2.4.6 Thermoneutral condition for concerted character

Figure 2.8 shows a Gibbs free energy plot in which $\Delta G^{\circ\prime}_{PT}$ and $^{app}\Delta G^{\circ\prime}_{ET}$ with respect to GSH have been assigned to the cartesian coordinates X and Y, respectively. The plotted data points correspond to the oxidant-base pairs in Table 2.3, so that each point represents a value of $^{app}\Delta G^{\circ\prime}_{ET}$ and $\Delta G^{\circ\prime}_{PT}$ calculated (eV) from the equilibrium constants $^{app}K_{ET}$ and K_{PT} respectively (Table 2.6). The axes are *thermoneutral* lines ($\Delta G^{\circ\prime} = 0$), that divide endo- and exothermic regions of the PT and ET reactions with GSH. Therefore, the five-step change of the buffer pK_a (0.12 eV) from 5.1 to 7.2 in Table 2.3 can easily be visualized for all oxidants given that values of $^{app}\Delta G^{\circ\prime}_{ET}$ with GSH can be taken from the simulations or estimated with Equation 2.7. When the same exothermic change of 0.12 eV in $\Delta G^{\circ\prime}_{PT}$ (Figure 2.8 and Table 2.6), was applied to all the oxidants, only $IrCl_6^{2-}$ was able to pass through an ET-*thermoneutral* point. In contrast, $Mo(CN)_8^{3-}$ is so far into the ET-endothermic region that, although the imposed $\Delta G^{\circ\prime}_{PT}$ moves it toward the center, its position is still ~0.1 eV away from the closest *thermoneutral* line. The oxidant $Fe(phen)_3^{3+}$, which is already at exothermic levels of $^{app}\Delta G^{\circ\prime}_{ET}$, would require weaker bases to get to the closest *thermoneutral* line. We postulate here that being at a *thermoneutral* point for either ET or PT or being sufficiently close to one is a requirement for rendering partial or total *concerted* character to a PCET reaction. In congruence with this assertion, $IrCl_6^{2-}$ is the mediator with the largest KIE that is most resistant to being reduced by buffer concentration increments, in contrast to $Mo(CN)_8^{3-}$ and $Fe(phen)_3^{3+}$ whose KIE vanish rather quickly under similar conditions (Table 2.4). The relationship between the magnitude of KIE and $\Delta G^{\circ\prime}$ of a

Table 2.6. Values of $\Delta G^{\circ\prime}$ (eV) versus GSH with Oxidant-Base Pairs

Buffer pK_a	$\Delta G^{\circ\prime}{}_{PT}$	$\Delta G^{\circ\prime}{}_{ET}$		
		$Mo(CN)_8{}^{3-}$	$IrCl_6{}^{2-}$	$Fe(phen)_3{}^{3+}$
5.1	0.212871	0.209410	0.062408	-0.034594
5.6	0.183306	0.179924	0.032921	-0.064081
6.2	0.147827	0.144583	-0.002419	-0.099421
6.5	0.130088	0.126963	-0.020039	-0.117041
7.2	0.088696	0.086299	-0.060703	-0.157705

Reaction is clearer when realizing that in a *thermoneutral* state the H being transferred is in a symmetrical *transition state* that is energetically equidistant from the products and reactants, such that the difference in the zero-point energy between the reactants and the *transition state* is maximum for several vibration modes.[30] Such a *thermoneutral* effect has been demonstrated in KIE studies of simple acid-base chemistry.[30] For instance, the deprotonation of nitroethane ($CH_3CH_2NO_2$ or $CH_3CD_2NO_2$) by amines has a maximum KIE when the pK_a of the conjugate acid of the amine base matches the pK_a of nitroethane.[38] Given the interplay of ET and PT, the same principle should be operative in PCET reactions. An ET in a *thermoneutral transition state* that is also coupled to a PT would place the latter into a partial symmetrical state (respect to ET only) that would display a sufficient difference in the zero-point energy of the vibrational modes between the reactants and the *transition state* that a KIE will be elicited. Consequently, a partial contribution of the *concerted* pathway would occur. From this argument, it must follow that the maximum level of *concertedness* should be attained when an oxidant-base pair of the appropriate $E^{\circ\prime}$ and pK_a with respect to GSH would furnish a total *coupled thermoneutral* state. That is, both $^{app}\Delta G^{\circ\prime}{}_{ET}$ and $\Delta G^{\circ\prime}{}_{PT}$ are equal or very close to zero and the oxidation of GSH will be located at the center of the coordinates in Figure 2.8. In this ideal condition, the *concerted* pathway will be

the dominant contributor to the PCET mechanism, its rate will reach a "*concerted limit*" value, and the energetic efficiency of the *concerted* pathway without intermediates will approach its theoretical maximum. Based on the slopes and intercepts calculated for the mediators in Figure 2.8, it can be seen that if $Mo(CN)_8^{3-}$ is paired with a base whose conjugate acid has a pK_a close to pK_{aSH} (~8.7), the reaction will intercept the vertical *thermoneutral* axis just 0.0019 eV from the center. Such a base will confer the highest degree of *concerted* behavior to $Mo(CN)_8^{3-}$ because $IrCl_6^{2-}$ and $Fe(phen)_3^{3+}$ will intercept the same *thermoneutral* line at points of exothermic bias towards ET, -0.1489 and -0.2459 eV, respectively. At the *thermoneutral* point for PT, the KIE for $Mo(CN)_8^{3}$ is expected to be higher than for $IrCl_6^{2-}$ and $Fe(phen)_3^{3+}$.

The aforementioned interpretation generally supports the notion of a "sweet spot" for *concerted* mechanisms of PCET, which has been noted before,[39] including evidence for it.[12] Most importantly, the predictive power of this analysis relies purely on considerations of the pK_a and $E°'$ for the species involved, including $E°'$-pH profiles (Pourbaix plots or the like). If this interpretation is true and can be verified with other systems, it will be useful in the design of catalysts for the different energy harvesting technologies that depend on PCET. We will be addressing some of the predictions made above in upcoming reports.
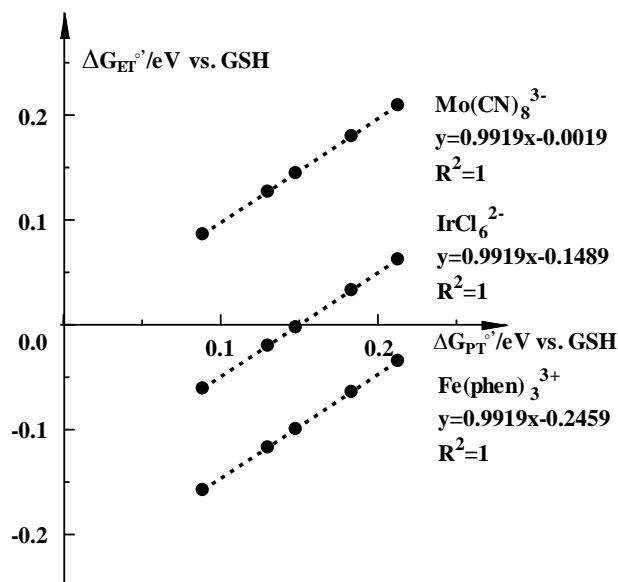
Figure 2.8 Values of $\Delta G^{\circ\prime}$ (eV) for Oxidant-Base Pairs in Table 2.6

The figure shows a plot with y-axis labeled $\Delta G_{ET}^{\circ\prime}/eV$ vs. GSH and x-axis labeled $\Delta G_{PT}^{\circ\prime}/eV$ vs. GSH, with three data series:

Mo(CN)$_8^{3-}$
y=0.9919x-0.0019
R^2=1

IrCl$_6^{2-}$
y=0.9919x-0.1489
R^2=1

Fe(phen)$_3^{3+}$
y=0.9919x-0.2459
R^2=1

2.5 Conclusions

Here we have described the oxidation of GSH by various electrogenerated oxidants in the presence of bases with pK_a above and below pK_{aSH} (8.7), so that negative and positive $\Delta G^{\circ\prime}_{PT}$ could be investigated. Similarly, given that GSH has an apparent redox potential that depends on the medium pH for values below 10.0, we also selected oxidants and pH conditions that would render $^{app}\Delta G^{\circ\prime}_{ET}$ above and below zero. The proposed mechanisms were fitted to digital simulations of experimental cyclic voltammograms carried out in the pH range 5.0 to 10.0 and at various buffer concentrations. We found that all the mediators made a partial contribution to the PCET pathways comprising mostly the PT-ET and the *concerted* routes with varying values of KIE. The fact that the acidity of the radical cation GSH$^{\bullet+}$ can be expected to be stronger than that of the hydronium ion, thus precluding its existence in water, was the reason for not proposing the ET-PT sequence. For H-isotope effects in identical conditions, the KIE for IrCl$_6^{2-}$ was the highest and consequently attributed the largest contribution of the *concerted* pathway in

comparison to $Mo(CN)_8^{3-}$ and $Fe(phen)_3^{3+}$. This assignment was explained as arising because $IrCl_6^{2-}$ is the closest to a *thermoneutral* point of $^{app}\Delta G^{\circ\prime} = 0$ for ET with GSH. Here the rationale lies on the well-documented observation that the highest KIE's in acid-base PT are measured when $\Delta pK_a = 0$. The same principle should operate in PCET because an ET *thermoneutral* point will still render a partial upper bound of difference in zero-point energy for vibrational modes between the reactants and the *transition state*, so that a KIE is educed. We took this rationale further to propose that the maximum level of *concerted* character for a PCET reaction should occur when PT and ET coincide at a *thermoneutral* point or very close to it by virtue of the pK_a and $E^{\circ\prime}$ values of the species involved. In this ideal *thermoneutral* state, the rate of the *concerted* pathway should reach its limit value and attain the maximum thermodynamic efficiency that stems from avoiding highly charged intermediates. Because our analysis is merely based on easily measured parameters like pK_a, $E^{\circ\prime}$, and $E^{\circ\prime}$-pH profiles, if corroborated with other systems, its predictive power will be useful in designing catalysts for energy harvesting processes that rely on PCET.

2.6 List of references

1.   Huynh, M. H. V.; Meyer, T. J., Proton-coupled electron transfer. *Chem. Rev.* **2007,** *107* (11), 5004-5064.

2.   Mayer, J. M., Proton-coupled electron transfer: A reaction chemist's view. *Annu. Rev. Phys. Chem.* **2004,** *55*, 363-390.

3.   Hammes-Schiffer, S.; Stuchebrukhov, A. A., Theory of Coupled Electron and Proton Transfer Reactions. *Chem. Rev.* **2010,** *110* (12), 6939-6960.

4.   Wenger, O. S., Proton-coupled electron transfer with photoexcited ruthenium(II), rhenium(I), and iridium(III) complexes. *Coord. Chem. Rev.* **2015,** *282*, 150-158.

5.   Forman, H. J.; Zhang, H. Q.; Rinna, A., Glutathione: Overview of its protective roles, measurement, and biosynthesis. *Mol. Asp. Med.* **2009,** *30* (1-2), 1-12.

6.   Warren, J. J.; Tronic, T. A.; Mayer, J. M., Thermochemistry of Proton-Coupled Electron Transfer Reagents and its Implications. *Chem. Rev.* **2010,** *110* (12), 6961-7001.

7.   Saveant, J. M., Electrochemical approach to proton-coupled electron transfers: recent advances. *Energy & Environmental Science* **2012,** *5* (7), 7718-7731.

8.   Meyer, T. J.; Huynh, M. H. V.; Thorp, H. H., The possible role of proton-coupled electron transfer (PCET) in water oxidation by photosystem II. *Angew. Chem.-Int. Edit.* **2007,** *46* (28), 5284-5304.

9.   Migliore, A.; Polizzi, N. F.; Therien, M. J.; Beratan, D. N., Biochemistry and Theory of Proton-Coupled Electron Transfer. *Chem. Rev.* **2014,** *114* (7), 3381-3465.

10.   Fecenko, C. J.; Thorp, H. H.; Meyer, T. J., The role of free energy change in coupled electron-proton transfer. *Journal of the American Chemical Society* **2007,** *129* (49), 15098-+.

11.   Gagliardi, C. J.; Murphy, C. F.; Binstead, R. A.; Thorp, H. H.; Meyer, T. J., Concerted Electron-Proton Transfer (EPT) in the Oxidation of Cysteine. *J. Phys. Chem. C* **2015,** *119* (13), 7028-7038.

12.   Bourrez, M.; Steinmetz, R.; Ott, S.; Gloaguen, F.; Hammarstrom, L., Concerted proton-coupled electron transfer from a metal-hydride complex. *Nat. Chem.* **2015,** *7* (2), 140-145.

13.   Lennox, J. C.; Dempsey, J. L., Influence of Proton Acceptors on the Proton-Coupled Electron Transfer Reaction Kinetics of a Ruthenium-Tyrosine Complex. *Journal of Physical Chemistry B* **2017,** *121* (46), 10530-10542.

14.   Binstead, R. A.; Moyer, B. A.; Samuels, G. J.; Meyer, T. J., Proton-Coupled Electron Transfer Between $Ru(bpy)_2(py)OH_2^{2+}$ and $Ru(bpy)_2(py)O^{2+}$ - A Solvent Isotope Effect (K_{H_2O}-K_{D_2O}) of 16.1. *Journal of the American Chemical Society* **1981,** *103* (10), 2897-2899.

15.   Medina-Ramos, J.; Oyesanya, O.; Alvarez, J. C., Buffer Effects in the Kinetics of Concerted Proton-Coupled Electron Transfer: The Electrochemical Oxidation of Glutathione Mediated by IrCl6 (2-)at Variable Buffer pK(a) and Concentration. *J. Phys. Chem. C* **2013,** *117* (2), 902-912.

16.   Medina-Ramos, J.; Oyesanya, O.; Alvarez, J. C., Reply to "Comment on 'Buffer Effects in the Kinetics of Concerted Proton-Coupled Electron Transfer: The Electrochemical Oxidation of Glutathione Mediated by IrCl6 (2-) at Variable Buffer pK(a) and Concentration". *J. Phys. Chem. C* **2014,** *118* (1), 743-745.

17.   Desimone, R. E.; Drago, R. S., Magetic Resonance Studies of Some Low-Spin D5 Tris Diimine Complexes. *Journal of the American Chemical Society* **1970,** *92* (8), 2343-+.

18.   Covington, A. K.; Paabo, M.; Robinson, R. A.; Bates, R. G., Use of the glass electrode in deuterium oxide and the relation between the standardized pD (paD) scale and the operational pH in heavy water. *Analytical Chemistry* **1968,** *40* (4), 700-706.

19.   Bard, A. J.; Faulkner, L. R., Electrochemical methods : fundamentals and applications. 2nd ed.. ed.; New York : Wiley: 2001; p 833.

20.   Alligrant, T. M.; Alvarez, J. C., The Role of Intermolecular Hydrogen Bonding and Proton Transfer in Proton-Coupled Electron Transfer. *J. Phys. Chem. C* **2011,** *115* (21), 10797-10805.

21.   Petrovic, S., Cyclic Voltammetry of Hexachloroiridate(IV): An Alternative to the Electrochemical Study of the Ferricyanide Ion. *The Chemical Educator* **2000,** *5* (5), 231-235.

22.   Nekrassova, O.; Kershaw, J.; Wadhawan, J. D.; Lawrence, N. S.; Compton, R. G., Oxidation of cysteine by electrogenerated octacyanomolybdate(v). *Physical Chemistry Chemical Physics* **2004,** *6* (6), 1316-1320.

23.   Carter, M. T.; Rodriguez, M.; Bard, A. J., oltammetric Studies of the Interaction of Metal-Chelates with DNA. 2. Tris-Chelated Complexes of Cobalt (III) and Iron (II) with 1,10-Phenanthroline and 2,2'-Bipyridine. *Journal of the American Chemical Society* **1989,** *111* (24), 8901-8911.

24.   Kavan, L.; Rapta, P.; Dunsch, L.; Bronikowski, M. J.; Willis, P.; Smalley, R. E., Electrochemical tuning of electronic structure of single-walled carbon nanotubes: In-situ Raman and vis-NIR study. *Journal of Physical Chemistry B* **2001,** *105* (44), 10764-10771.

25.   Madej, E.; Wardman, P., The oxidizing power of the glutathione thiyl radical as measured by its electrode potential at physiological pH. *Arch. Biochem. Biophys.* **2007,** *462* (1), 94-102.

26.   Sun, J. F.; Stanbury, D. M., Kinetics and mechanism of oxidation of thioglycolic acid by hexachloroiridate(IV). *J. Chem. Soc.-Dalton Trans.* **2002,** (5), 785-791.

27.   Wang, X. G.; Stanbury, D. M., Direct oxidation of L-cysteine by Fe-III(bpy)(2)(CN)(2) (+) and Fe-III(bpy)(CN)(4) (-). *Inorganic Chemistry* **2008,** *47* (3), 1224-1236.

28.   Hoffman, M. Z.; Hayon, E., One-electron reduction of the disulfide linkage in aqueous solution. Formation, protonation, and decay kinetics of the RSSR- radical. *Journal of the American Chemical Society* **1972,** *94* (23), 7950-7957.

29.   Bhattarai, N.; Stanbury, D. M., Oxidation of Glutathione by Hexachloroiridate(IV), Dicyanobis(bipyridine)iron(III), and Tetracyano(bipyridine)iron(III). *Inorganic Chemistry* **2012,** *51* (24), 13303-13311.

30.   Anslyn, E. V.; Dougherty, D. A., *Modern Physical Organic Chemistry*. University Science Books: Sausalito CA, 2006.

31.   Jencks, W. P., *Catalysis in Chemistry and Enzymology*. McGraw-Hill: New York, 1969.

32.   Saveant, J. M., Elements of Molecular and Biomolecular Electrochemistry: An Electrochemical Approach to Electron Transfer Chemistry. John Wiley & Sons, & Inc.: Hoboken, New Jersey, 2006.

33.   Jencks, W. P., General Acid-Base Catalysis of Complex Reactions in Water. *Chem. Rev.* **1972,** *72* (6), 705-&.

34.   Jencks, W. P., Enforced General Acid-Base Catalysis of Complex-Reactions and its Liminations. *Accounts of Chemical Research* **1976,** *9* (12), 425-432.

35.   Marcus, R. A.; Sutin, N., Electron Transfer in Chemistry and Biology. *Biochimica Et Biophysica Acta* **1985,** *811* (3), 265-322.

36.   Laidler, K. J., Chemical Kinetics. Prentice Hall: 1987.

37.   Qian, W.; Krimm, S., Biopolymers. 1994; Vol. 34.

38.   Dixon, J. E.; Bruice, T. C., Dependence of the primary isotope effect (kH/kD) on base strength for the primary amine catalyzed ionization of nitroethane. *Journal of the American Chemical Society* **1970,** *92* (4), 905-909.

39.   Dempsey, J. L., Proton-Coupled Electron Transfer Metal hydrides find the sweet spot. *Nat. Chem.* **2015,** *7* (2), 101-102.

40.   McMurry, J., Organic Chemistry. Brooks & Cole: Belmont, CA, 2004.

Chapter 3: Oxidation mechanism of Trolox in aqueous and non-aqueous media using electrochemistry and UV-vis spectroscopy at variable pH

3.1 Abstract

Electrochemical oxidation of Trolox in aqueous and non-aqueous solutions was investigated by voltammetric techniques in the presence of supporting electrolytes. The hydroxyl group at the 6-position of Trolox can be electrochemically oxidized in a $-2e^-/-H^+$ process to form the phenoxonium cation. Subsequent chemical reactions of phenoxonium ions are different in the presence of different nucleophiles. In aqueous solutions at pH 11.91, Trolox immediately forms the phenolate anion, which can be oxidized in two sequential one-electron steps to form phenoxonium cation. Phenoxonium cation is stable and can be reduced back to Trolox on the cyclic voltammetry time scale. However, some of phenoxonium ions react with water to form electroactive quinone as the final product. Because the quinone can adsorb on the surface of the working electrode, it could be monitored by voltammetric experiments since it has different formal electrode potentials from that of Trolox. In acetonitrile at pH 6.81, Trolox can be electrochemically oxidized by one electron to form the cation radical, which then quickly dissociates into neutral radical. The phenoxyl radical is further oxidized at the electrode surface by one electron to form the phenoxonium cation. A cross-conjugated ketone was formed by simultaneous intramolecular cyclization of the carboxylate to the phenoxonium cation, which would not happen to analogues with an extended hydrocarbon chain at the 2-position instead of a carboxyl moiety. With trace water present in acetonitrile, some of phenoxonium cations undergo hydrolysis reactions to ultimately convert into quinones but in low yields. Cross-conjugated ketone is the main product for the oxidation of Trolox in non-aqueous solutions. In situ UV-vis

experiments were performed before and after the bulk electrolysis of Trolox. The band detected at 291 nm was identical to that of Trolox at approximately neutral pH and the band at 308 nm was due to the phenolate anion. The appearance of a strong absorption at 269 nm indicated the presence of quinone. The appearance of a band at 233 nm was identical to that observed in the UV-vis spectrum of cross-conjugated ketones. The related thermodynamic and kinetic parameters for the proposed reaction mechanism were estimated with the data modeled using digital simulation techniques.
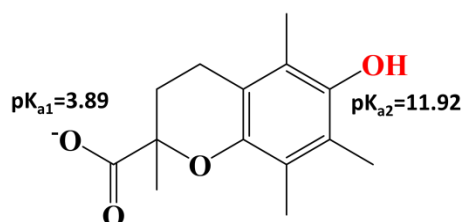
Scheme 3.1. Deprotonated Trolox (TOH)

3.2 Introduction

Natural and synthetic antioxidants have been gaining increasing interest recently since they play an important role in biological and industrial processes. For example, knowing the antioxidant content and antioxidant capacity of nutritional components can provide guidance to diet design and commercial antioxidant-rich products. Numerous antioxidants have frequently been compared to identify the most potent ones. Several methods are currently used to evaluate the antioxidative power of various compounds and materials. Trolox Equivalent Antioxidant Capacity (TEAC) assay, which was originally described by Miller et al., is one of the most widely used methods.[1] The measurement procedures of the TEAC assay occurred by two principal steps. The first step was to generate the ABTS [2,2' – azinobis-(3-ethylbenzothiazoline-

6-sulfonic acid)] radical cation by activation of metmyoglobin with hydrogen peroxide in the presence of ABTS. The long-lived blue-green $ABTS^{\bullet+}$ has absorption maxima at wavelengths 645 nm, 734 nm, and 815 nm.[2][3] The second step was to add a certain concentration of the antioxidant sample to scavenge the $ABTS^{\bullet+}$. The extent of decolorization as percentage inhibition of the $ABTS^{\bullet+}$ was related to that of Trolox as a standard and gave the TEAC value of that antioxidant. This assay has gained wide recognition because it is not expensive and the procedure is straight forward. Although it has been improved by other researchers and used with success,[4][5][6][7] it is also criticized as a result of its limitations.[8]

Trolox (6-hydroxy-2,5,7,8-tetramethylchroman-2-carboxylic acid) is used as a standard in the TEAC assay (Scheme 3.1). In comparison to α-tocopherol, the most biologically active and naturally abundant component of vitamin E, Trolox has a carbonyl group at the 2-position instead of the extended phytyl hydrocarbon chain. The proton-coupled electron transfer reactions of Trolox are associated with the OH group at the 6-position. Consequently, Trolox is an analogue of α-tocopherol but is more hydrophilic, which enables the TEAC assay to study both water-soluble and lipid-soluble antioxidants.

The TEAC assay is a useful tool for evaluating the antioxidant capacity of antioxidants and ranking them. Despite its advantages, it is reported that the TEAC values of a single compound or sample differed in various solvents or pH values.[5] Another impediment of this assay is that it may not reflect the antioxidant effect of only one structure. The TEAC values represent the antioxidant power of the parent compound plus the potential antioxidant capacity of the reaction product(s) because any products with a redox potential lower than that of $ABTS^{\bullet+}$ may react with this radical.[8] Therefore, a deeper and more thorough understanding of the electrochemical reaction mechanisms of Trolox is required. Previous chemical oxidations of

Trolox were carried out in aqueous solutions and related thermodynamic and kinetic data were estimated indirectly from pulse-radiolysis measurements.[9] [10] [11] [12] Malyszko et al. reported electrochemical experiments of Trolox in water[13] (without proposing any mechanism), methanol and ethanol,[14] and acetic acid[15] (proposed similar oxidation mechanisms) but without identifying any generated oxidized forms of Trolox. Webster et al. studied the electrochemical oxidation of α-tocopherol with a combination of electrochemical and spectroscopic experiments.[16] [17] They demonstrated that the intermediate phenoxonium cation is long-lived in dry organic solvents but quickly reacts with the trace water to form a hemiketal.[18] It is very interesting to compare the electrochemical properties of Trolox in aqueous and nonaqueous solutions and there is still a lack of information to interpret its oxidation mechanism difference in the two different environments.

In this chapter, the anodic oxidation of Trolox, in 0.5 M NaCl and 0.1 M phosphate buffer at pH 11.91 and separately in acetonitrile with 0.25 M Bu_4NPF_6 at pH 6.81 were investigated. This presented work is focused on comparing the electrochemical behaviors of Trolox in water and acetonitrile solvents to determine whether they undergo the same mechanism or not. It was discovered that after the bulk electrolysis of Trolox the final products in two different environments were different based on the UV-vis spectroscopic characterization results. The voltammetric data were then simulated by DigiElch software to estimate related thermodynamic parameters and rate constants for electrochemical reactions of Trolox.

3.3 Experimental Section

3.3.1 Reagents and Materials

Trolox ((±)-6-hydroxy-2,5,7,8-tetramethylchromane-2-carboxylic acid, 97%) and sodium hydroxide (NaOH, 99.9%) were purchased from Sigma-Aldrich. Tetrabutylammonium

hexafluorophosphate(Bu$_4$NPF$_6$, 99.0%), sodium chloride (NaOH, $\geqslant$ 99.999%), sodium phosphate dibasic (Na$_2$HPO$_4$, 99.999%), and sodium phosphate monobasic (NaH$_2$PO$_4$, 99.999%) were obtained from Fluka. Acetonitrile (ACN, 99.9% for residue analysis) was obtained from Acros Organics. Hydrochloric acid (HC, 37.5%) was obtained from Fisher Scientific. All reagents and solvents were used as received without further purification. All aqueous solutions were prepared from Millipore water ($\geq$18.2 M$\Omega\bullet$cm, Billerica, MA). Various pH values of buffer solutions were calculated by the Henderson-Hasselbalch equation. Desired pH values were adjusted by diluted NaOH and/or HCl and were measured by the Fisher Scientific Education pH/Ion 510 pH meter, calibrated with pH 4.00 $\pm$ 0.01, 7.00 $\pm$ 0.01, 10.00 $\pm$ 0.01 reference standard buffers (RICCA chemical company, Arlington, TX) at room temperature.

3.3.2 Electrochemical Methods

All electrochemical experiments were conducted with a CHI 660C potentiostat (CH Instruments, Austin, TX), a three-electrode regular glass cell, and a Faraday cage. Glassy carbon (GC, diameter 3.0 mm) and platinum (Pt, diameter 2.0 mm) were used as working electrodes in aqueous and non-aqueous solutions, respectively. Their surface was polished by a mixture of 0.05 μm alumina and Millipore water on a cleaning pad (Lake Bluff, Illinois) and rinsed with Millipore water before use. Pt wire and Ag/AgCl/ 1.0 M KCl were used as auxiliary and reference electrodes, respectively, in 0.5 M NaCl solutions containing 0.6 mM Trolox and 0.1 M phosphate buffer. The potential was scanned from -1.0 V to 0.6 V vs. Ag/AgCl/ 1.0 M KCl. Ag wire was used as the quasi-reference electrode in non-aqueous solutions containing 2.1 mM Trolox and 0.25 M Bu$_4$NPF$_6$ in acetonitrile. The potential was scanned from -0.6 V to 1.3 V vs. Ag wire. All solutions were freshly prepared with Millipore water and purged with N$_2$ prior to the experiments, and the operating potential window was determined by running blank solutions

to avoid complicated effects to the system caused by O_2 and H_2O. All cyclic voltammograms were recorded at various scan rates and background subtracted at room temperature, 23 ± 1 °C.

Bulk electrolysis with coulometry was used to calculate the number of electrons transferred during the oxidation process and study the products of the Trolox reaction. Bulk electrolyzed solutions, auxiliary and reference electrodes were the same as those used for performing cyclic voltammetry experiments. Pt mesh was used as the working electrode. The solution was simultaneously deoxygenated and stirred using bubbles of N_2 gas. Faraday's law, Equation 3.1, was used to determine the number of electrons transferred during the bulk oxidation process. Here, Q is the charge passed, in coulombs; n is the number of electrons transferred; N is the number of moles of the starting compound; F represents the Faraday constant (96485 C mol^{-1}).

$$n = \frac{Q}{NF}$$
Equation 3.1

3.3.3 UV-Vis Spectroscopic Measurement

UV-Vis spectra of Trolox and related oxidized products were obtained on 8453 spectrophotometer, incorporating a 1-mm pathlength quartz cell (Agilent Technologies). In UV-Vis measurements; the solvent solutions with supporting electrolytes were used to blank the spectra.

3.3.4 Digital Simulation

Experimental cyclic voltammograms obtained under different experimental conditions were simulated using the DigiElch 7 (ElchSoft, Kleinromstedt, Germany) software package, whose theoretical basis has been described in previous reports.[19] [20] [21] [22] [23] The electrochemical mechanisms depicted in Scheme 3.2 and 3.3 were entered into DigiElch software. Simulations of

experimental cyclic voltammograms were performed by successively refining related parameters until the simulated voltammograms closely matched the experimental curves. Simulated parameters are given in Table 4.1 and Table 4.2. These values matched all the experimental voltammograms over a range of scan rates in order to obtain optimal kinetic and electrochemical data.

3.4 Results and Discussion

3.4.1 Electrochemistry and UV-vis spectroscopy of Trolox in aqueous solutions

Figure 3.1 shows multicycled voltammograms of aqueous solutions of 0.6 mM Trolox recorded on a 3 mm diameter GC electrode at pH 11.91. The potential scale was referred to the Ag/AgCl reference electrode. The potential range was between -1.0 and 0.6 V and the starting potential was -1.0 V. A new anodic peak centered at -0.41 V appeared as a second positive-going scan (blue line in Figure 3.1) only after the first CV cycle (red line in Figure 3.1) had returned to the beginning point of -1.0 V. The newly appearing anodic peak increased for the first few cycles and reached a maximum peak current (black line in Figure 3.1). Another anodic peak current centered at 0.03 V decreased for the first few scan cycles. Observed phenomena suggest that the first anodic peak (at about -0.41 V) came from the oxidized forms of Trolox. The product(s) from the oxidation process of Trolox adsorbed on the surface of the working electrode and blocked the active surface of GC, resulting in a decrease of the second anodic peak current (at about 0.03 V).

Figure 3.1 Cyclic voltammograms of 0.6 mM Trolox in 0.5 M NaCl with 0.1 M PB recorded at a 3 mm diameter GC electrode at pH 11.91 for the first four runs. Scan rate is 0.2 V/s.

To gain more insight into the oxidation mechanism of Trolox in aqueous solutions, voltammograms with different potential ranges were recorded as shown in Figure 3.2. In Figure 3.1 A, no oxidation and reduction peaks were observed when scanning the potential only between -1.0 and 0.2 V. This suggests an electron transfer of Trolox to the electrode could not occur when the applied potential was less than 0.2 V. An extended potential window between -1.0 to 0.6 V was used to record electrochemical reactions of Trolox within the same solutions. The voltammogram shows an oxidation process with an anodic peak at approximately 0.03 V, and a reverse reduction process with two cathodic peaks centered at approximately -0.025 and -0.45 when the scan direction was switched, as given in Figure 3.2 B. The anodic peak is associated with the $-2e^-/-H^+$ proton-coupled electron transfer process of Trolox to form a phenoxonium cation (Scheme 3.2).[12, 14-15, 24] A new anodic peak at approximately -0.41 V appeared due to the electroactive product generated from decomposition reactions of the oxidized form of Trolox, and ultimately converted into quinone.[25] [26] [27] The quinones are electroactive and adsorbed on the surface of the GC electrode. The voltammetric peaks in Figure

3.2 D are associated with electrochemical reactions between quinone and hydroquinone. After polishing the surface of the GC working electrode, no redox reaction was detected within the potential window between -1.0 to 0.2 V as shown in Figure 3.2 E. The reverse reductive peak detected at approximately -0.025 V suggests the existence of phenoxonium cations (TO^+). The lifetime of TO^+ was investigated by observing the reverse reductive peak at various scan rates (Figure 3.3). At a scan rate of 0.1 V/s, the first reductive peak current at about 0.025 V was smaller than the second reductive peak current at approximately -0.45 V. At a scan rate of 2 V/s, the first reductive peak current was much higher than that of the second reductive peak when the scan direction was reversed. This implies the phenoxonium cation of Trolox is stable in aqueous solution for at least several minutes and its peak current increases in size as the scan rate is increased.

The electrochemical responses observed for Trolox in Figure 3.2 can be interpreted based on the mechanism in Scheme 3.2. At pH 11.91, TOH immediately forms the phenolate anion (TO^-), which can be oxidized in two sequential one-electron steps to form phenoxyl radical ($TO^\bullet$) and TO^+. When the scan direction is reversed, the reductive peak at about -0.025 V is

Scheme 3.2 Electrochemical oxidation mechanism of Trolox in water at pH 11.91 used in digital simulations. The homogeneous chemical equilibrium, forward rate and backward rate constants, and heterogeneous electron transfer values are given in Table 4.1. R = COO^-.
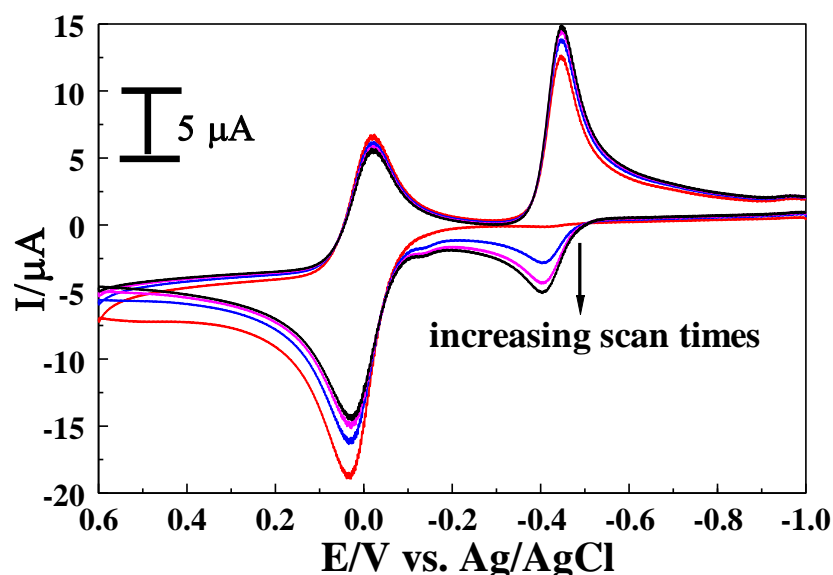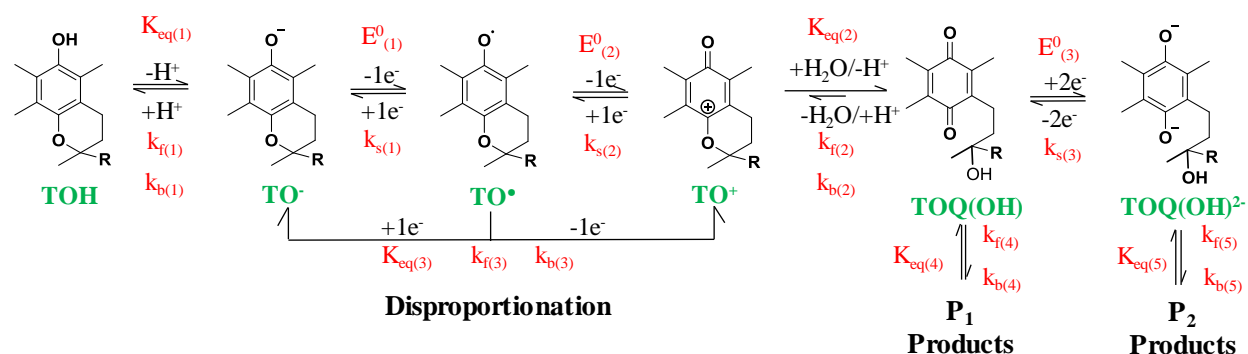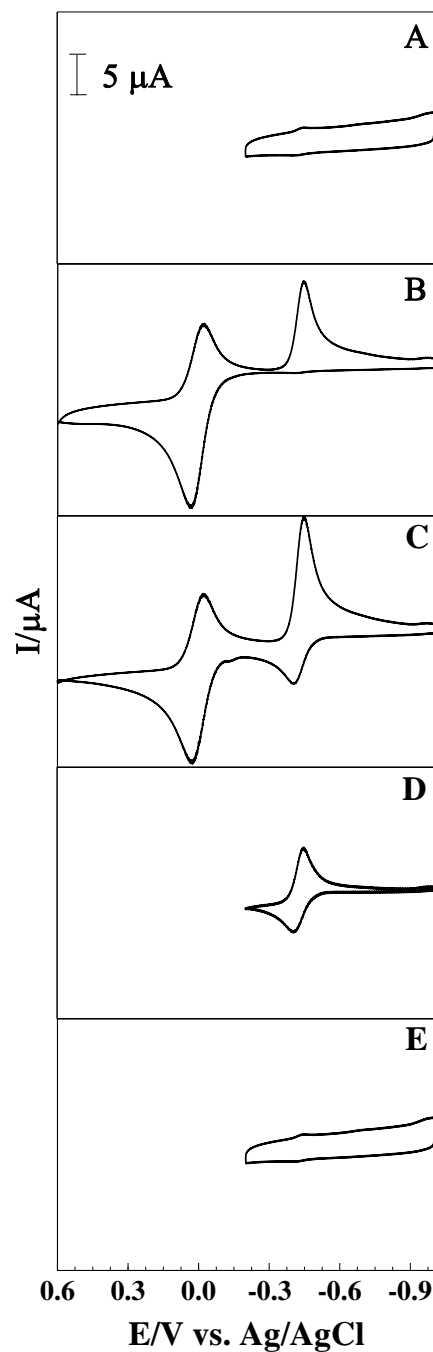
Figure 3.2 Cyclic voltammograms of 0.6 mM Trolox in 0.5 M NaCl with 0.1 M PB recorded at a 3 mm diameter GC electrode at pH 11.91. Scan rate is 0.2 V/s. (A: scan -1.0—0.2— -1.0 V, B: first time scan -1.0—0.6— -1.0 V, C: fourth time scan -1.0—0.6— -1.0 V, D: before polishing the electrode -1.0—0.2— -1.0 V, E: after polishing the electrode -1.0—0.2— -1.0 V.) B, C, and D are voltammograms after the background subtraction. A and E are curves with the background current.

associated with the reverse reaction to regenerate the starting phenol (TOH). The TO$^\bullet$ has a short lifetime in this condition and could not be detected by UV-vis spectroscopy and electrochemical experiments. The phenoxyl radicals can be consumed by a heterogeneous electron transfer process to form TO$^+$, or homogeneous disproportionation reaction.[26][27] Some of the TO$^+$ undergoes a hydrolysis reaction to form hemiketal, and ultimately form an electroactive quinone.[12,28] TO$^+$ and quinone can be differentiated by voltammetric methods because they have different formal potentials and long lifetimes.

Figure 3.3 Cyclic voltammograms with various scan rates of 0.6 mM Trolox in 0.5 M NaCl with 0.1 M PB recorded at a 3 mm diameter GC electrode at pH 11.91. Scan rates are 0.1, 0.2, 0.5, 1, 2 V/s.

Bulk electrolysis experiments were performed to gain more mechanistic information for the oxidation of Trolox. As shown in Figure 3.4, the black line represents the voltammetric curve of Trolox before bulk electrolysis. The red line is the CV obtained after the electrolysis reaction occurred for 800 s. The blue line shows the CV after 1600 s bulk electrolysis. The oxidation and reduction peaks at potentials -0.025 and 0.03 V decreased as the electrolysis time increased

because the applied potential 0.2 V was positive enough to oxidize Trolox and because the concentration of Trolox in the bulk solution decreased. The redox peaks at potentials -0.41 and -0.45 V increased with a longer electrolysis time. The experimental data of bulk electrolysis experiments confirmed that the phenoxonium cation is relatively long-lived. Some of the TO^+ was reduced back to the starting material and led to a relatively small cathodic peak at -0.025 V. Some of the TO^+ decomposed and reacted with water to form quinone. The redox peaks at -0.4 to -0.5 V were due to the secondary reaction products as shown in Scheme 3.2. The secondary reaction products were electroactive and showed redox peaks at potentials around -0.42 V, indicating that the oxidized products are long-lived. The number of electrons transferred in the oxidation process of Trolox was calculated to be 1.86 based on the charge obtained during the 1.5 hours of bulk electrolysis, which agrees with previous literature results.[14-15] Additional small peaks at about -0.06 and -1.0 V appeared after exhaustive oxidative electrolysis. This suggests that several different kinds of species were formed associated with the decomposition reaction of phenoxonium ions. The exact structures of the oxidized forms of Trolox are still not clear because it is difficult to isolate them from the solution. Various secondary reaction products were formed which may be because phenoxonium cations have resonance structures and are captured by different nucleophiles to form different chromanones and quinones.[25-27, 29]

UV-vis spectra obtained during the bulk electrolysis of 1.0 mM Trolox at room temperature are shown in Figure 3.5. The intermediates TO^+ and $TO^\bullet$ in water were not detected by the UV-vis experiments because $TO^\bullet$ is unstable and was further oxidized to TO^+; and the instability of TO^+ was due to an immediate hydrolysis reaction at room temperature.[29-30] The spectrum of the Trolox solution at pH 11.91 in a prior bulk electrolysis experiment showed an absorbance at 308 nm and was attributed to the phenolate anion TO^- (black in Figure 3.5).[29, 31]

When a potential of -0.2 V was applied to the Trolox solution for 600 s, a spectrum with the same band position and similar intensity absorbance was obtained because -0.2 V is not positive enough to oxidize TO⁻, as shown in Figure 3.5 (open circles). Applying a potential 0.2 V for 600 s, which is sufficiently positive to oxidize Trolox led to the appearance of a band at 269 nm (Figure 3.5 solid circles). The product quinone (Scheme 3.2) is characterized by the appearance of a strong absorption at 269 nm.[24, 29-30]
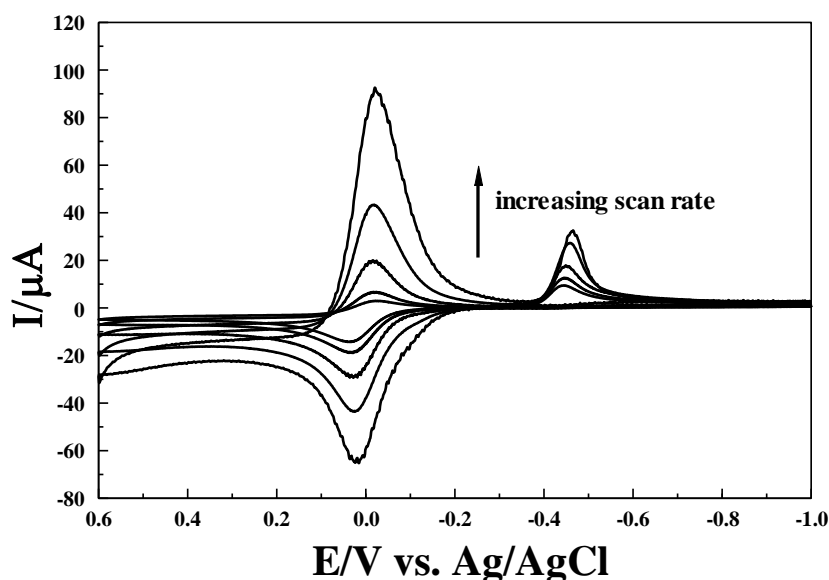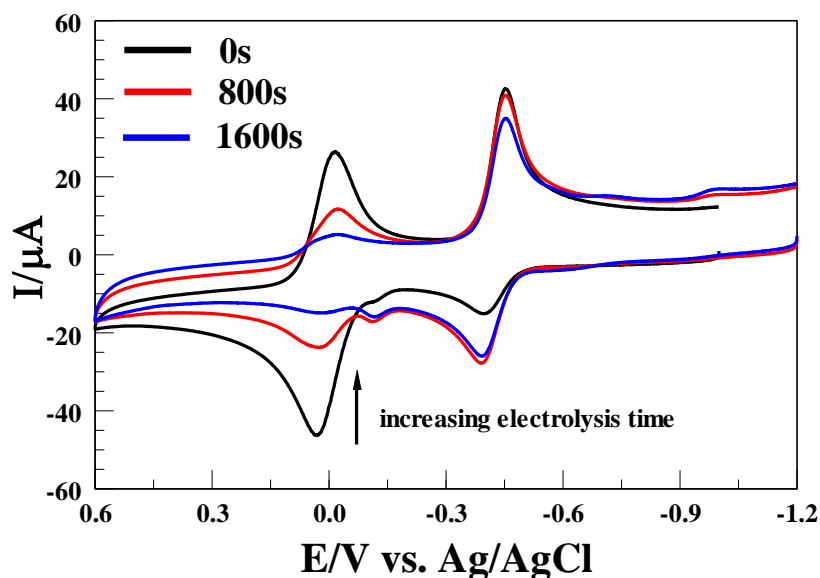

Figure 3.4 Cyclic voltammograms of 1.0 mM Trolox in 0.5 M NaCl with 0.1 M PB recorded at a 3 mm diameter GC electrode at pH 11.91 with different electrolysis times (0s, 800s, 1600s, respectively). Scan rate is 0.5 V/s. The applied potential is at 0.2 V.
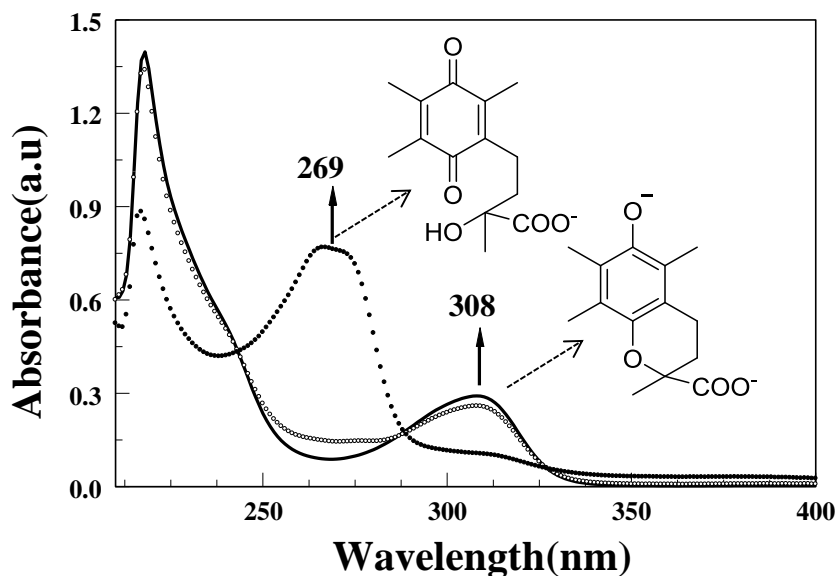
Figure 3.5 UV-vis spectra obtained with 1.0 mM Trolox in 0.5 M NaCl with 0.1 M PB at pH 11.91; prior to the bulk oxidation of Trolox (black line); after the oxidation of Trolox over 600s at -0.2V (open circles); after the oxidation of Trolox over 600s at 0.2 V (solid circles).

3.4.2 Electrochemistry and UV-vis spectroscopy of Trolox in nonaqueous solutions

Cyclic voltammograms of Trolox in acetonitrile with 0.25 M Bu_4NPF_6 at pH 6.81 were obtained as shown in Figure 3.6. The curve in Figure 3.6 A was different from those in Figure 3.1 because different solvents affect the shapes of the voltammetric curves. The proposed oxidation mechanism of Trolox in acetonitrile shown in Scheme 3.3 was slightly different from the proposed mechanism of Trolox in aqueous solutions shown in Scheme 3.2.

Figure 3.6 B shows the cyclic voltammogram of 2.1 mM Trolox in acetonitrile (containing 0.25 M Bu_4NPF_6 as a supporting electrolyte) at a scan rate of 0.2 V/s recorded at a 2 mm diameter Pt working electrode. The CV shows an oxidative peak at approximately 0.90 V vs. Ag/AgCl and a reverse reductive peak at approximately -0.10 V vs. Ag/AgCl. The forward process is due to the two-electron oxidation of Trolox and the reverse reductive peak is

associated with the reduction reaction of quinone (TOQ(OH)) according to the mechanism in Scheme 3.3.
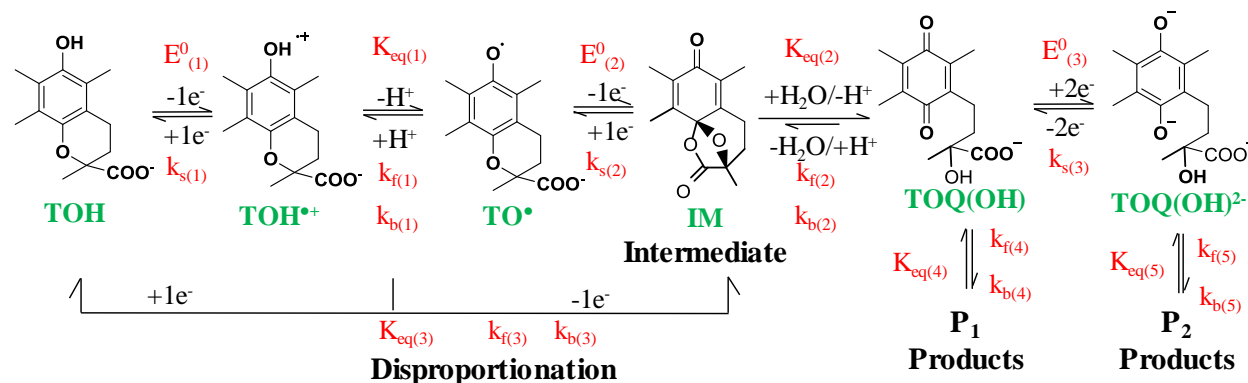
Scheme 3.3 Electrochemical oxidation mechanism of Trolox in acetonitrile at pH 6.81 used in digital simulations. The homogeneous chemical equilibrium, forward rate and backward rate constants, and heterogeneous electron transfer values are given in Table 4.2.

The reductive peak at about -0.10 V can only be detected after the first cyclic voltammogram cycle has been returned to the starting point because no Faraday current was observed in the potential range between -0.6 V and 0.4 V (Figure 3.6 A). No new peak appeared after multicycled voltammograms in an extended potential window between -0.6 V and 1.3 V (Figure 3.6 C). None of the starting materials, intermediates and products were adsorbed on the surface of the working electrode as shown in Figure 3.6 D and Figure 3.6 E, a finding which is different from that of Trolox in aqueous solutions.

Since the reverse reductive peak is widely separated from the forward oxidative peak ($\Delta Ep = 1.0$ V), we propose that the reverse peak at about -0.1 V was not generated from the reduction of phenoxonium cation (TO$^+$). The digital simulation data as described later also confirmed our proposed mechanism as given in Scheme 3.3. Bulk electrolysis and UV-vis spectroscopy experiments were performed to gain more information for the oxidation mechanism

of Trolox in acetonitrile. In Figure 3.7, the oxidative peak at about 0.90 V disappeared after the bulk electrolysis process for 1200 s, since the applied potential 1.2 V was sufficiently positive to completely oxidize the Trolox. When a potential of 0.4 V was applied to electrolyze Trolox solution for 600s, the components of the solution stayed the same because 0.4 V is not positive enough to oxidize Trolox. The UV-vis spectrum of the 0.1 mM Trolox solution prior to the bulk electrolysis (black line) is almost the same as the spectrum of the same solution after 600 s electrolysis applying a potential of 0.4 V (open circles), as given in Figure 3.8. Trolox is characterized by the strong absorption at 291 nm which agrees with previously published reports.[24, 26, 29] Bulk electrolysis experiments can provide information about the oxidized compounds with a longer lifetime (minutes). Cyclic voltammetry experiments can gain mechanistic information about oxidized and reduced species that are stable at least on the time scale of the CV experiment (second).[24] After the bulk electrolysis of the same Trolox solution (applying a potential of 1.2 V), the reductive peak at approximately -0.1 V disappeared and a strong absorbance at 233 nm and a weak absorbance at 270 nm were observed. The new band at 233 nm is due to the cross-conjugated ketone as shown in Figure 3.8 and this intermediate is not electroactive as confirmed by other research groups.[9, 12, 16, 29] The disappearance of the reductive peak was due to the slow transformation of cross-conjugated ketone into quinone as described in Scheme 3.3. At pH 6.81, Trolox is oxidized by one electron to form the cation radical ($TOH^{\bullet+}$), which quickly dissociates into $TO^{\bullet}$ and H^+. $TO^{\bullet}$ is further oxidized to form a phenoxonium cation (TO^+).[32] Surprisingly, TO^+ has a short lifetime in this environmental condition and immediately converts into the cross-conjugated ketone by intramolecular cyclization of the carboxylate to the resonance of TO^+.[29] The cross-conjugated ketone undergoes a slow hydrolysis to form quinone.[9, 32] With low levels of water in acetonitrile, the generated

Figure 3.6 Cyclic voltammograms of 2.1 mM Trolox in CH_3CN with 0.25 M Bu_4NPF_6 recorded at a 2 mm diameter Pt electrode at pH 6.81. Scan rate is 0.2 V/s. (A: scan -0.6—0.4— -0.6 V, B: first time scan -0.6—1.3— -0.6 V, C: fourth time scan -0.6—1.3— -0.6 V, D: before polishing the electrode -0.6—0.4— -0.6 V, E: after polishing the electrode -0.6—0.4— -0.6 V.)
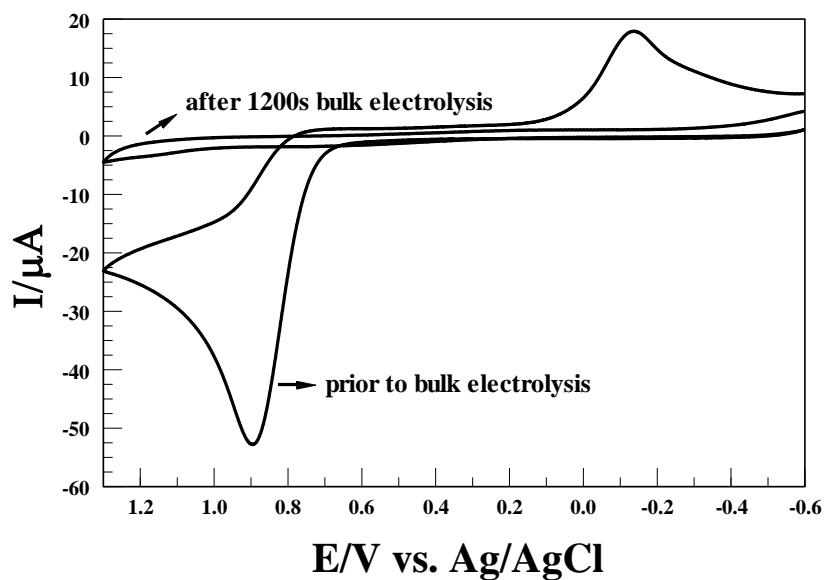
Figure 3.7 Cyclic voltammograms of 2.1 mM Trolox in CH_3CN with 0.25 M Bu_4NPF_6 recorded at a 2 mm diameter Pt electrode at pH 6.81 before and after bulk electrolysis at 1.2 V. Scan rate is 0.2 V/s.
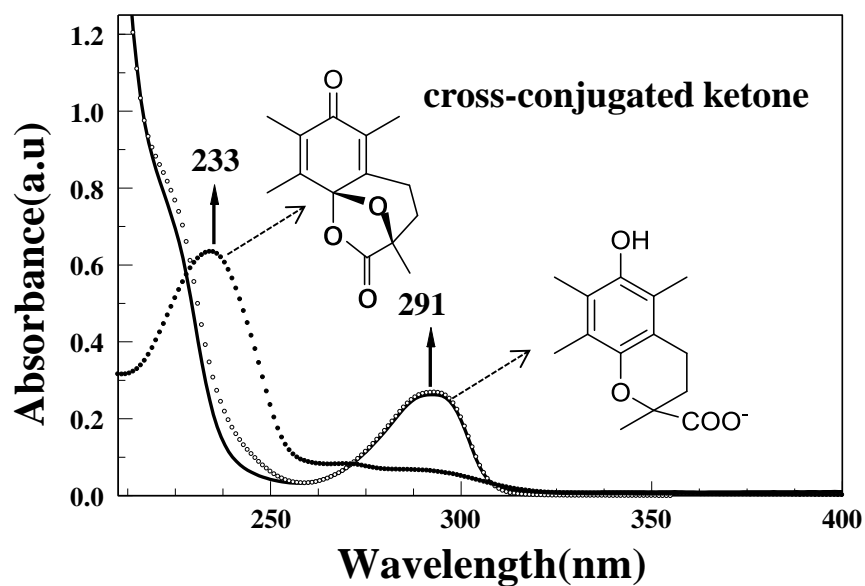
Figure 3.8 UV-vis spectra obtained during the bulk oxidation of 0.1 mM Trolox in CH_3CN with 0.25 M Bu_4NPF_6 at pH 6.81; prior to the bulk oxidation of Trolox (black line), after the oxidation of Trolox by 600s at 0.4V (open circles), after the oxidation of Trolox by 600s at 1.2V (solid circles).

quinone was found in extremely low yields, leading to the weak absorbance intensity at 270 nm and the disappearance of the reductive peak at approximately -0.10 V after the bulk electrolysis of Trolox.

3.4.3 Digital simulation of experimental voltammograms of Trolox in aqueous and nonaqueous solutions

Digital simulations of the experimental CV data were performed to estimate the thermodynamic and kinetic parameters for the electrochemical oxidation of Trolox. The simulations were based on the mechanisms described in Scheme 3.2 and 3.3. At pH 11.91, Trolox was deprotonated, followed by two successive one-electron transfer reactions to form phenoxonium cations.[14, 29] As shown in Figure 3.9, when the scan rate was progressively increased, the peak associated with the reduction of phenoxonium cations at approximately -0.025 V increased in size. Because the hydrolysis reactions of TO^+ were outrun at faster scan rates, the oxidation peak current of TO^+ was higher than that of quinones at approximately -0.50 V at a scan rate of 1 V/s. At pH 6.81, the proton transfer and electron transfer reactions of Trolox undergo a $-e^-/-H^+/-e^-$ process.[14, 29] In an organic solvent, the voltammograms of Trolox, as given in Figure 3.10, are markedly different from those in aqueous solutions. The disappearance of the reductive peak was related to the chemical instability of phernoxonium cations which are reactive toward nucleophiles.[33] The carboxylate anion at the 2-position of Trolox exhibits strong nucleophilic properties compared to OH^- and H_2O.[15, 33] Intramolecular cyclization of the carboxylate to the unsaturated ring reaction can happen quickly to form a cross-conjugated ketone which is not electroactive on the surface of Pt working electrode.[29, 33] A single oxidation wave of Trolox was observed because the second electron transfer is thermodynamically more facile than the first one ($E°_{(2)} - E°_{(1)} < 0$). The potentials

70
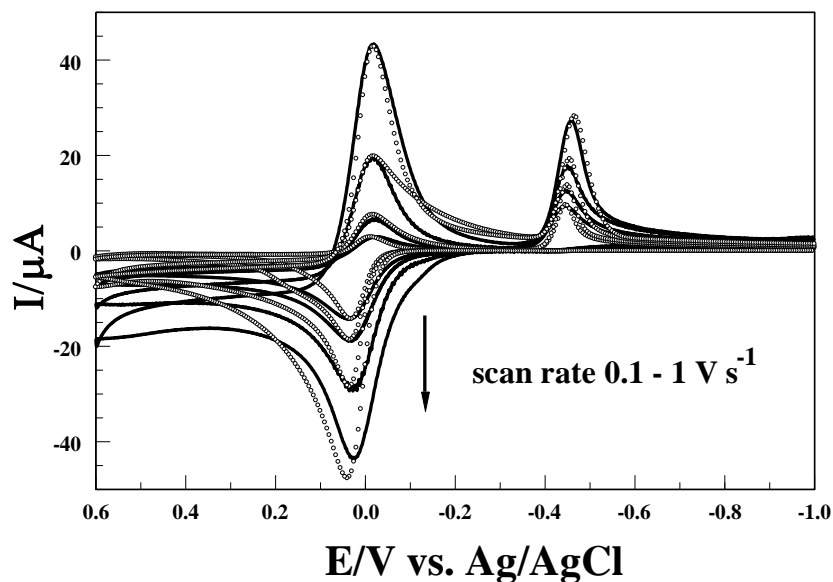
Figure 3.9 Experimental (solid line) and simulated (open circles) CV response of 0.6 mM Trolox in 0.5 M NaCl with 0.1 M PB recorded at a 3 mm diameter GC electrode at pH 11.91. Scan rates were 0.1, 0.2, 0.5 and 1.0 V/s.

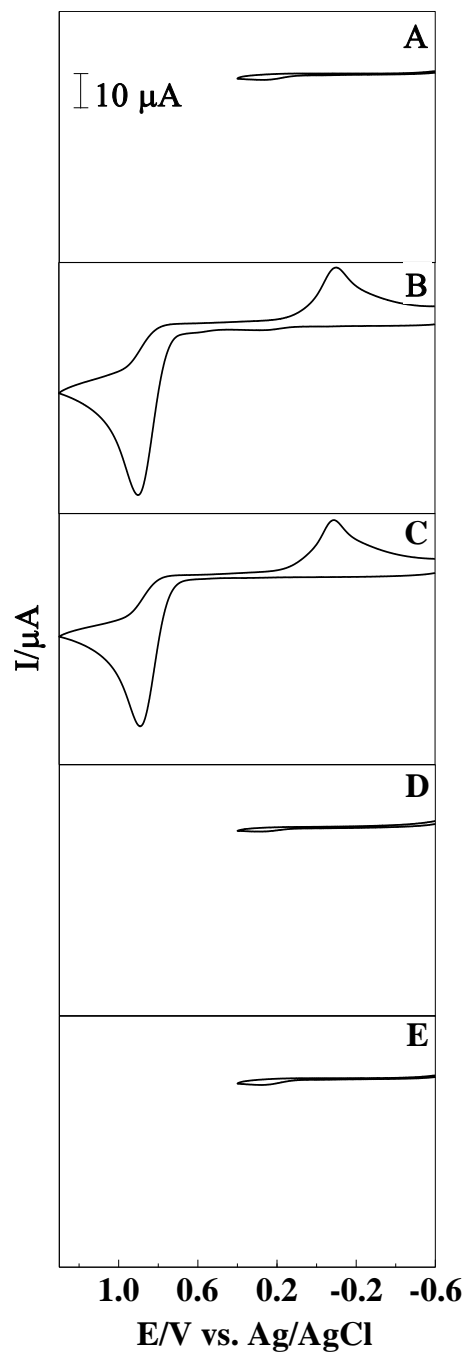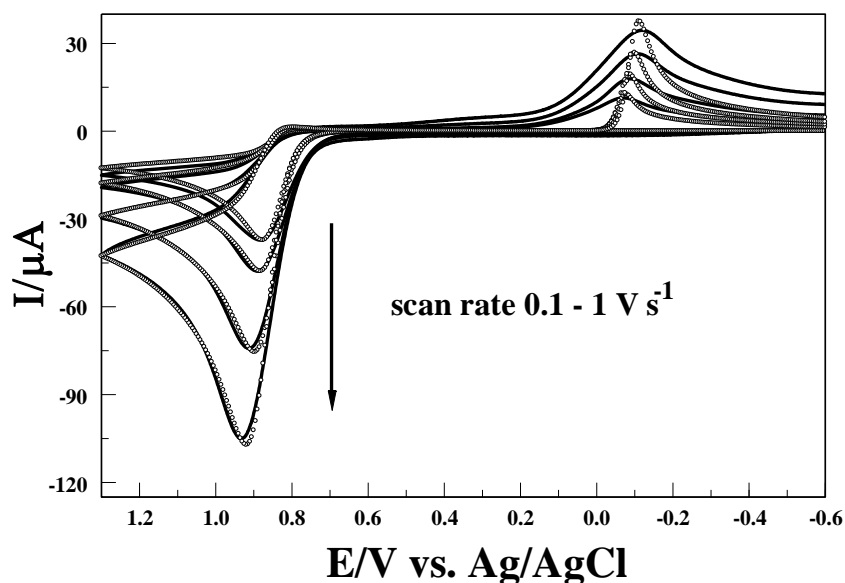**Figure 3.10** Experimental (solid line) and simulated (open circles) CV response of 2.1 mM Trolox in CH_3CN with 0.25 M Bu_4NPF_6 recorded at a 2 mm diameter Pt electrode at pH 6.81. Scan rates were 0.1, 0.2, 0.5 and 1.0 V/s.

Table 3.1 Associated thermodynamic and kinetic parameters obtained by digital simulation of voltammetric data for the reaction mechanism of Trolox in aqueous solution at pH 11.91 given in Scheme 3.2

Electrochemical Reactions	E	k_s	α
$TO^{\bullet} + e^- = TO^-$	0.026 ± 0.007	0.1	0.5
$TO^+ + e^- = TO^{\bullet}$	-0.004	0.1	0.5
$TOQ(OH) + 2e^- = TOQ(OH)^{2-}$	-0.433	0.1	0.5
Chemical Reactions	**K**	k_f	k_b
$TOH = TO^- + H^+$	1×10^{-12}	5×10^5	4.17×10^{17}
$TO^+ + H_2O = TOQ(OH) + H^+$	0.2	0.01	0.05
$2TO^{\bullet} = TO^+ + TO^-$	3.3 ± 0.8	20000	$(5.2 \pm 0.5) \times 10^3$
$TOQ(OH) = P_1$	0.01	1	100
$TOQ(OH)^{2-} = P_2$	1	0.1	0.1

Table 3.2 Associated thermodynamic and kinetic parameters obtained by digital simulation of voltammetric data for the reaction mechanism of Trolox in nonaqueous solution at pH 6.81 given in Scheme 3.3

Electrochemical Reactions	E	k_s	α
$TOH^{\bullet+} + e^- = TOH$	0.87 ± 0.01	0.1	0.5
$IM + e^- = TO^{\bullet}$	0.85 ± 0.01	0.1	0.5
$TOQ(OH) + 2e^- = TOQ(OH)^{2-}$	$(-0.09) \pm 0.01$	0.1	0.5
Chemical Reactions	**K**	k_f	k_b
$TOH^{\bullet+} = TO^{\bullet} + H^+$	5×10^{-5}	3000	6×10^7
$IM + H_2O = TOQ(OH) + H^+$	3000	1000	0.33
$TOH^{\bullet+} + TO^{\bullet} = IM + TOH$	1.16 ± 0.01	3.0×10^7	$(2.57 \pm 0.01) \times 10^7$
$TOQ(OH) = P_1$	1000	2 ± 0.2	$(1.9 \pm 0.2) \times 10^{-3}$
$TOQ(OH)^{2-} = P_2$	1000	10	0.01

($E^{\circ}_{(1)}$, $E^{\circ}_{(2)}$ in Table 3.1 and 3.2), measured approximately from the voltammetric waves, do not correspond to the thermodynamic formal potentials since they are influenced by the kinetics of the homogeneous reactions, as shown in Schemes 3.2 and 3.3. All the parameters in Tables 3.1 and 3.2 were used for each simulation. To obtain the optimal kinetic and electrochemical parameters, parameters values given in Tables 3.1 and 3.2 had to match all the experimental data

over a range of scan rates (Figures 3.9 and 3.10). Reaction 4 and 5 in Schemes 3.2 and 3.3 are homogeneous reactions of quinone and hydroquinone, respectively.

3.5 Conclusions

The electrochemical and spectroscopic results in the present work provide insights into differences of the oxidation mechanisms of Trolox in aquesous and nonaqueous solutions. Considering the voltammetric behavior and the results of the digital simulation, we can conclude that the stability of phenoxonium cations is strongly influenced by nucleophiles in the background electrolyte. Since these ions are expected to mainly react slowly with water as the weak neclephile, the phenoxonium ions are stable and can be detected in the CV time scale in aqueous solutions. The instabilities of TO^+ in acetonitrile are due to the intramolecular cyclization of the carboxylate to the unsaturated ring to form a cross-conjugated ketone as the major product. Moreover, the effects of trace water in organic solvents should be considered when interpreting the electrochemical behaviour of phenols in organic solvents. The lifetime of phenoxonium cations will vary in the presence of varous amounts of water since water is always an impurity in organic solvents. Finally, although the Trolox Equivalent Antioxidant Capacity (TEAC) assay is applicable to both aqueous and lipophilic systems; various solvents and pH values will affect the antioxidant capacities of the same antioxidant when applying the TEAC assay. A standarization procedure still needs to explore when the TEAC assay is used to measure and rank antioxidants in biological fluids and natural products.

3.6 List of references

1.   Miller, N. J.; Riceevans, C.; Davies, M. J.; Gopinathan, V.; Milner, A., A Novel method for Measuring Antioxidant Capacity and its Application to Monitoring the Antioxidant Status in Premature Neonates. *Clinical Science* **1993,** *84* (4), 407-412.

2.   Riceevans, C.; Miller, N. J., Total Antioxidant Status in Plasma and Body-Fluids. *Oxygen Radicals in Biological Systems, Pt D* **1994,** *234*, 279-293.

3.   Miller, N. J.; RiceEvans, C. A., Spectrophotometric determination of antioxidant activity. *Redox Rep.* **1996,** *2* (3), 161-171.

4.   Arts, M.; Haenen, G.; Voss, H. P.; Bast, A., Masking of antioxidant capacity by the interaction of flavonoids with protein. *Food and Chemical Toxicology* **2001,** *39* (8), 787-791.

5.   van den Berg, R.; Haenen, G.; van den Berg, H.; Bast, A., Applicability of an improved Trolox equivalent antioxidant capacity (TEAC) assay for evaluation of antioxidant capacity measurements of mixtures. *Food Chemistry* **1999,** *66* (4), 511-517.

6.   Erel, O., A novel automated direct measurement method for total antioxidant capacity using a new generation, more stable ABTS radical cation. *Clinical Biochemistry* **2004,** *37* (4), 277-285.

7.   Rezk, B. M.; Haenen, G.; van der Vijgh, W. J. F.; Bast, A., The antioxidant activity of phloretin: the disclosure of a new antioxidant pharmacophore in flavonoids. *Biochemical and Biophysical Research Communications* **2002,** *295* (1), 9-13.

8.   Arts, M.; Haenen, G.; Voss, H. P.; Bast, A., Antioxidant capacity of reaction products limits the applicability of the Trolox Equivalent Antioxidant Capacity (TEAC) assay. *Food and Chemical Toxicology* **2004,** *42* (1), 45-49.

9.   Davies, M. J.; Forni, L. G.; Willson, R. L., Vitamin-E Analog Trolox -C Electron Spin Resonance and Pulse-Radiolysis Studies of Free Radical Reactions. *Biochem. J.* **1988,** *255* (2), 513-522.

10.   Jovanovic, S. V.; Steenken, S.; Tosic, M.; Marjanovic, B.; Simic, M. G., FLAVONOIDS AS ANTIOXIDANTS. *Journal of the American Chemical Society* **1994,** *116* (11), 4846-4851.

11.   Bors, W.; Michel, C.; Schikora, S., Interaction of Flavonoids with Ascorbate and Determination of Their Univalent Redox Potentials - A Pulse Radiolysis Study. *Free Radic. Biol. Med.* **1995,** *19* (1), 45-52.

12.   Nakamura, M.; Hayashi, T., Oxidation Mechanism of Vitamin-E Analog (Trolox-C, 6-Hydroxy-2,2,5,7,8-Pentamethylchroman) and Vitamin-E by Horseradish-Peroxidase and Myoglobin. *Arch. Biochem. Biophys.* **1992,** *299* (2), 313-319.

13.   Malyszko, J.; Mechanik, M., Anodic oxidation of trolox in aqueous solutions. *Polish Journal of Chemistry* **2004,** *78* (9), 1575-1582.

14.   Karbarz, M.; Malyszko, J., Voltammetric behavior of trolox in methanol and ethanol solutions. *Electroanalysis* **2008,** *20* (17), 1884-1890.

15.   Malyszko, J.; Karbarz, M., Electrochemical oxidation of trolox and alpha-tocopherol in acetic acid: A comparative study. *J. Electroanal. Chem.* **2006,** *595* (2), 136-144.

16.   Lee, S. B.; Lin, C. Y.; Gill, P. M. W.; Webster, R. D., Transformation of alpha-tocopherol (vitamin E) and related chromanol model compounds into their phenoxonium ions by chemical oxidation with the nitrosonium cation. *J. Org. Chem.* **2005,** *70* (25), 10466-10473.

17.   Peng, H. M.; Choules, B. F.; Yao, W. W.; Zhang, Z. Y.; Webster, R. D.; Gill, P. M. W., Long-lived radical cations as model compounds for the reactive one-electron oxidation product of vitamin E. *Journal of Physical Chemistry B* **2008,** *112* (33), 10367-10374.

18.   Tan, Y. S.; Chen, S. S.; Hong, W. M.; Kan, J. M.; Kwek, E. S. H.; Lim, S. Y.; Lim, Z. H.; Tessensohn, M. E.; Zhang, Y. L.; Webster, R. D., The role of low levels of water in the electrochemical oxidation of alpha-tocopherol (vitamin E) and other phenols in acetonitrile. *Physical Chemistry Chemical Physics* **2011,** *13* (28), 12745-12754.

19.   Rudolph, M., Attaining exponential convergence for the flux error with second- and fourth-order accurate finite-difference equations. I. Presentation of the basic concept and application to a pure diffusion system. *J. Comput. Chem.* **2005,** *26* (6), 619-632.

20.   Rudolph, M., Attaining exponential convergence for the flux error with second- and fourth-order accurate finite-difference equations. Part 3. Application to electrochemical systems comprising second-order chemical reactions. *J. Comput. Chem.* **2005,** *26* (11), 1193-1204.

21.   Rudolph, M., Digital simulations on unequally spaced grids. Part 3. Attaining exponential convergence for the discretisation error of the flux as a new strategy in digital simulations of electrochemical experiments. *J. Electroanal. Chem.* **2004,** *571* (2), 289-307.

22.   Rudolph, M., Digital simulations on unequally spaced grids. Part 1. Critical remarks on using the point method by discretisation on a transformed grid. *J. Electroanal. Chem.* **2002,** *529* (2), 97-108.

23.   Rudolph, M., Digital simulations on unequally spaced grids. Part 2. Using the box method by discretisation on a transformed equally spaced grid. *J. Electroanal. Chem.* **2003,** *543* (1), 23-39.

24.   Peng, H. M.; Webster, R. D., Investigation into phenoxonium cations produced during the electrochemical oxidation of chroman-6-ol and dihydrobenzofuran-5-ol substituted compounds. *J. Org. Chem.* **2008,** *73* (6), 2169-2175.

25.   Yue, Y. N.; Novianti, M. L.; Tessensohn, M. E.; Hirao, H.; Webster, R. D., Optimizing the lifetimes of phenoxonium cations derived from vitamin E via structural modifications. *Organic & Biomolecular Chemistry* **2015,** *13* (48), 11732-11739.

26.   Durckheimer, W.; Cohen, L., The Chemistry of 9-Hydroxy-α-tocopherone, a Quinone Hemiacetal. *Journal of the American Chemical Society* **1964,** *86* (20), 4388-4393.
27.   Marcus., M. F.; HAWLEY., M., Electrochemical studies of the redox behavior of α-tocopherol. *Biochimica et Biophysica Acta* **1970,** *201* (1), 1-8.

28.   Costentin, C., Electrochemical approach to the mechanistic study of proton-coupled electron transfer. *Chem. Rev.* **2008,** *108* (7), 2145-2179.

29.   Thomas, M. J.; Bielski, B. H. J., Oxidation and Reaction of Trolox-C, α-Tocopherol Analog, in Aqueous-Solutions - A Pulse-Radiolysis Study. *Journal of the American Chemical Society* **1989,** *111* (9), 3315-3319.

30.   Williams, L. L.; Webster, R. D., Electrochemically Controlled Chemically Reversible Transformation of α-Tocopherol (Vitamin E) into Its Phenoxonium Cation. *Journal of the American Chemical Society* **2004,** *126* (39), 12441-12450.

31.   Advances in Physical Organic Chemistry, Vol 50. In *Advances in Physical Organic Chemistry, Vol 50*, Williams, I. H.; Williams, N. H., Eds. Academic Press Ltd-Elsevier Science Ltd: London, 2016; Vol. 50, pp 1-282.

32.   Parker, V. D., Anodic Alkyl Transfer from Hydroquinone Ethers. 2. Anodic Oxidation of an alpha-Tocopherol Model Compound. *Journal of the American Chemical Society* **1969,** *91* (19), 5380-&.

33.   McMurry, J., *Organic Chemistry, sixth ed.* Brooks Cole: 1999.

Chapter 4: Electrochemical studies of α-tocopherol via collisions of oil-in-water emulsion droplets on an ultramicroelectrode

4.1 Abstract

α-Tocopherol (α-TOH), the most biologically stable and active component of vitamin E, display voltammetric features which enabled electrochemical mechanistic studies of vitamin E. A combination of electrochemical and spectroscopic experiments have shown that α-TOH undergoes a -2e$^-$/H$^+$ oxidation process to form long-lived phenoxonium ions (α-TO$^+$) in dry organic solvents such as acetonitrile and dichloromethane. In the presence of trace water in organic solvent, phenoxonium ions (α-TO$^+$) are susceptible to nucleophilic attack to form hemiketals (α-TOQ(OH)) through hydrolysis reactions. Ultimately, the hemiketals can convert into quinones. Most chemical studies on vitamin E focused on its antioxidant properties due to the existence of α-TOH and its associated phenoxyl radical (α-TO$^\bullet$). However, other oxidized forms of α-TOH, generated through electrochemical reactions, are also worthy of consideration when interpreting its unique biological functions. The long-lived phenoxonium ions (α-TO$^+$) in organic solvent, unlikely to react with free radicals, may play a role in its non-antioxidant actions, but the stability of α-TOH decrease in phospholipid bilayers. The problem is that the electrochemical results obtained in organic solution may not be entirely relevant for its functions in a real biological system. Therefore, it is important to find a model to examine the oxidative behavior of vitamin E within phospholipids. In the present work, the particle collision electroanalysis (PCE) method was used to explore the biological functions of α-TOH in an environment that is similar to the biological environment. α-TOH with an ionic liquid in toluene

emulsion droplets were prepared as described later. The current response was quantitatively analyzed to obtain additional electrochemical behaviors of α-TOH in the oil/water interfaces.
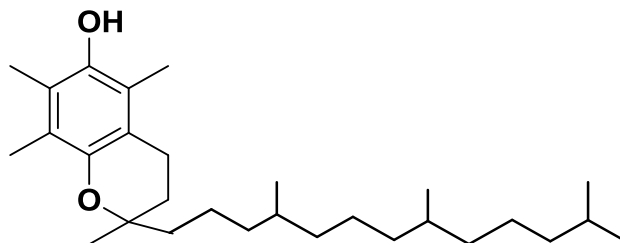
Scheme 4.1 Structure of α-tocopherol (α-TOH)

4.2 Introduction

Vitamin E refers to eight different naturally occurring compounds, four tocopherols and four tocotrienols.[1] Vitamin E compounds with a saturated alkyl chain are designated tocopherols while the side chain of tocotrienols contains three double bonds.[2] α-Tocopherol (α-TOH) is by far the most biologically active, naturally abundant, and fully methylated of the four (α, β, γ, and δ) structurally related components of vitamin E (Scheme 4.1). Although vitamin E (α-TOH) has long been recognized as the major antioxidant in membranes for decades, its exact function has taken on a degree of controversy in recent years.[3][4] The majority of studies have argued that α-TOH plays an important role as an antioxidant in mammalian tissues to protect living cell membranes (lipids) by reacting with free radicals.[5][6][7] α-TOH has been proposed to inhibit the free radical chain autoxidation cycle by two principal steps.[6-7] First, one α-TOH molecule reacts with an oxidized site in a cell membrane (LOO$^\bullet$) to obtain the lipid hydroperoxide (LOOH) and the tocopheroxyl radical (α-TO$^\bullet$), as shown in Equation 4.1. Second, one α-TO$^\bullet$ molecule reacts with another LOO$^\bullet$ radical, which is shown in Equation 4.2. This chemistry suggests that one α-

TOH molecule is able to inhibit two LOO$^\bullet$ sites. Moreover, the orientation and dynamics of α-TOH within a bilayer affected by the nature of bulk phospholipids is thought to be critical for explaining its antioxidant actions in membranes.[3-4, 6] On the other hand, there is a growing body of evidence that the main purpose of α-TOH is to act as a cellular signaling molecule by interacting with other proteins and enzymes of the cell.[8 9 10] For example, protein kinase C (PKC), a family of isoenzymes, plays an important role in cellular transduction and regulates cellular growth, differentiation, and secretion.[11] α-TOH can cause the inhibition of PKC translocation, which relates to its growth-inhibitory effects on vascular smooth muscle cells.[8, 11]

$$LOO^\bullet + \alpha\text{-}TOH \longrightarrow LOOH + \alpha\text{-}TO^\bullet \qquad \textbf{Equation 4.1}$$

$$LOO^\bullet + \alpha\text{-}TO^\bullet \longrightarrow (\alpha\text{-}TO)OOL \qquad \textbf{Equation 4.2}$$
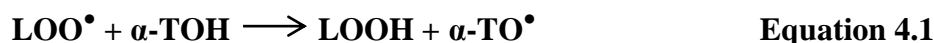
It is generally true that many natural occurring phenols have an antioxidative function in biological systems. The neutral compound (α-TOH) and its associated phenoxyl radical (α-TO$^\bullet$) are thought to be involved in the biological chemistry of its antioxidative cases.[12 6-7] Proton and electron transfer reactions occurring at the hydroxyl group of α-TOH to reduce free radicals and the extended phytyl chain at the 2-position allows for penetration into phospholipid bilayers. Nevertheless, extensive electrochemical experiments have demonstrated the existence of additional semistable oxidized compounds since α-TOH undergoes -2e$^-$/-H$^+$ chemically reversible proton and electron transfer reactions.[13 14 15] Other generated forms of α-TOH, like phenoxonium cation (α-TO$^+$), cation radical (α-TOH$^{+\bullet}$), dication (α-TOH^{2+}), phenolate anion (α-TO$^-$), hemiketal (α-TOQ(OH)), and p-quinones were determined by a combination of electrochemical and in situ spectroscopic analyses in organic solvents under various pH environments.[15 16 17] The phenoxonium cation (α-TO$^+$) has a long lifetime compared to other phenols, at least on a cyclic voltammetry time-scale.[18] Richard's research group has proposed

that phenoxonium cation (α-TO$^+$) may have importance in α-TOH's biologically non-antioxidant cases since it is unlikely that phenoxonium cation has any role in the antioxidant mechanism.[18] Therefore, all of the oxidized forms of vitamin E are worthy of consideration when considering chemical reasons for α-TOH's non-antioxidant actions.[14] Currently, there are no detailed mechanisms in existence to explain how those properties of α-TOH affect its non-antioxidant functions.

Most of the earlier electrochemical and spectroscopic experiments designed to form the basis for interpreting α-TOH's electrochemical behavior were performed in organic solution.[14, 16, 18] The effects of low levels of water in the hydrophobic environment on the electrochemical properties of α-TOH were also studied. In aprotic organic solvents at approximately neutral pH, electrochemically induced transformation of α-TOH containing trace water is shown in our proposed mechanism; see Scheme 4.2 below. For vitamin E, proton transfer and electron transfer steps occur via a consecutive -1e$^-$/-H$^+$/-1e$^-$ chemically reversible electrochemical oxidation process to form a cation radical (α-TOH$^{+\bullet}$), neutral radical (α-TO$^\bullet$), and phenoxonium ion (α-TO$^+$).[14] A corresponding reduction peak is observed when the scan direction is reversed at fast scan rates due to the reduction of phenoxonium ion (α-TO$^+$) to generate the starting material α-TOH. The associated long-lived phenoxonium ions of α-TOH are reactive with trace water present in the solvent to form hemiketals through hydrolysis reactions. The final products were p-quinones but in low yields (Scheme 4.2).[13] Most associated forms of α-TOH can be monitored by voltammetric methods since they are electroactive and have different formal potentials.[17] Even the electrochemical studies of α-TOH are important for interpreting and identifying detailed reaction mechanisms; those results may not be entirely relevant for its action in phospholipid bilayers. It is necessary to determine whether these proposed reactions in Scheme

4.2 can occur within lipid bilayers. A considerable amount of work has focused on the study of its physical location in biological membranes.[6-7][19] Katsaras et al. studied the vertical position of α-TOH within membranes and reported that the hydroxyl phenolic head is positioned at the lipid/water interface to have easy access to polar soluble reducing agents, while the hydrophobic phytyl chain is pointed into the lipid bilayer.[19] The stability of the phenoxonium ion and other oxidized forms of α-TOH will decrease since the chromanol heads are positioned at the lipid/water interface and they are reactive with water. Therefore, a lipid/water model having a similar biological environment is necessary to examine the oxidative behavior of α-TOH.
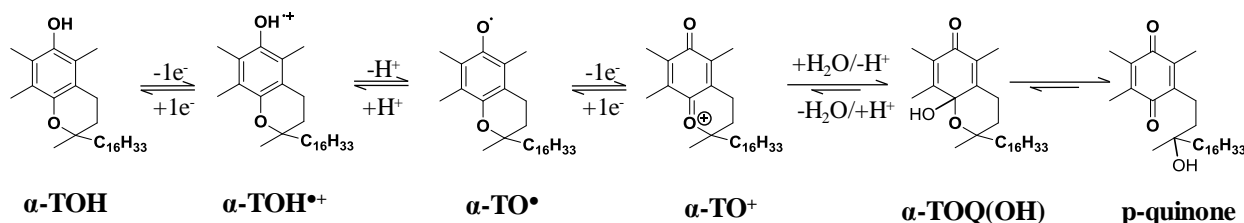
Scheme 4.2 Electrochemical oxidation mechanism for α-tocopherol in organic solvent containing trace water.

Particle collision electroanalysis (PCE) is an emerging methodology that is currently being used to characterize oil/water emulsion droplets. The "emulsion droplet reactor" (EDR) can be used to study the electrochemical behavior of α-TOH by observing single emulsion droplet collisions at an ultramicroelectrode.[20] In the present work, toluene with a low dielectric constant was used as the dispersed phase. The active redox species, α-TOH, is only soluble in toluene. Water was used as the continuous phase. The ionic liquid, trihexyltetradecylphosphonium bi(trifluoromethylsulfonyl)amide (IL-PA), was used as the supporting electrolyte to increase the conductivity of the oil phase as well as the emulsifier to

stabilize the emulsion droplets (Scheme 4.3). When the toluene droplet collides with the active surface of ultramicroelectrode, electron transfer reactions occur and current spikes are observed as α-TOH is oxidized at the toluene/water/platinum boundaries, which are similar to the lipid/water interfaces.[19, 21] By quantitatively analyzing the single soft particle collision data, the emulsion droplet size distribution, droplet contents, and detailed oxidation process of α-TOH will be obtained.
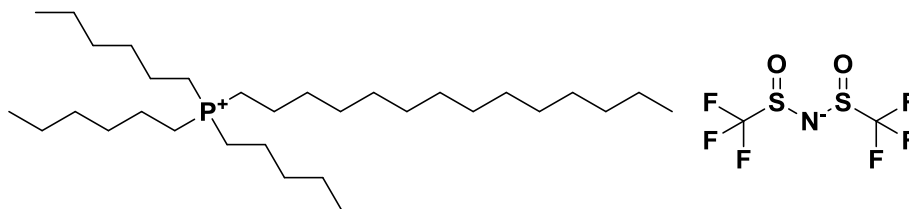
Scheme 4.3 Structure of ionic liquid trihexyltetradecylphosphonium bi(trifluoromethylsulfonyl)amide (IL-PA)

4.3 Experimental Section

4.3.1 Reagents and Materials

All reagents and solvents were used as received. α-Tocopherol (≥99.5%), trihexyltetradecylphosphonium bi(trifluoromethylsulfonyl)amide (IL-PA) (≥95.0%), ferrocenemethanol powder (97%), and toluene (99.8%, anhydrous) were obtained from Sigma-Aldrich. Deionized water (DI, ≥18.2 MΩ•cm, Millipore, Billerica, MA) was used to prepare all aqueous solutions. Aqueous and non-aqueous solvents were deoxygenated with nitrogen (N_2) before use. An N_2 atmosphere was maintained inside the electrochemical cell during the performance of the experiments at room temperature (23 ± 1 °C). A platinum (Pt, 10 µm

diameter) microelectrode was obtained from CH Instruments, Inc. (Austin, TX). A Pt minielectrode (1mm disk) was purchased from eDAQ (EE014 Minielectrode Kit – PEEK).

4.3.2 Instrumentation and Electrochemical Analysis

All electrochemical experiments were performed using a CHI 660C potentiostat (CH Instruments, Austin, Texas) with a three-electrode cell inside a Faraday cage. For cyclic voltammetry experiments, a planar Pt electrode of 1.0 mm diameter was used as the working electrode. An ultramicroelectrode Pt (10 μm in diameter) was used as the working electrode for amperometric i-t experiments. The same counter (Pt wire) and quasi-reference (Ag wire) electrodes were applied to toluene solutions and toluene droplet emulsions. All solutions and emulsions were degassed thoroughly with nitrogen and an N_2 atmosphere was maintained above the solutions during the measurements. Votex (Votex Genie 2^{TM}, Fisher Brand) and Bransonic ultrasonic cleaner (1510 Branson) were used to create emulsions. The dynamic light scattering (DLS) experiments were performed using Zetasizer Nano Series equipment (Malvern, Westborough, MA). SingleCounter software developed by Dario Omanovic (Centre for Marine and Environmental Research, Ruder Boskovic Institude, Croatia) was used to analyze current response (spikes) resulting from particles colliding with the ultramicroelectrode.

4.3.3 Preparation of the Toluene Emulsions

The toluene/water emulsions were prepared by dissolving 30 mM α-tocopherol and 500 mM IL-PA in toluene. A 0.1 mL mixture of toluene (α-tocopherol + IL-PA) was added to 4.9 mL of Millipore water. After that, the solution was vortexed vigorously for 20 s, and immediately sonicated for 4 minutes. The average diameter of the toluene (α-tocopherol + IL-PA)/water emulsion droplets was 3.7 ± 0.3 μm measured by DLS. The concentration of the toluene (α-

tocopherol + IL-PA)/water emulsion droplets was approximately calculated from the total toluene (α-tocopherol + IL-PA) volume (0.1 mL) divided by the average single emulsion droplet volume (26.5 pL), and the calculated value was 0.12 pM.

4.4 Results and Discussion

4.4.1 Cyclic voltammetric studies of α-tocopherol in toluene solution

After the preparation of α-tocopherol in toluene solution, the electrochemical behavior of ensembles was investigated using cyclic voltammetry. Toluene is a low dielectric medium which has a dielectric constant, ε of 2.38.[22] To reduce the ohmic drop of the solution, a hydrophobic ionic liquid, IL-PA was used as the supporting electrolyte (Scheme 4.3).[20] Voltammetric responses of 30 mM α-tocopherol in bulk toluene solution with 500 mM IL-PA were recorded and are shown in Figure 4.1 and Figure 4.2.
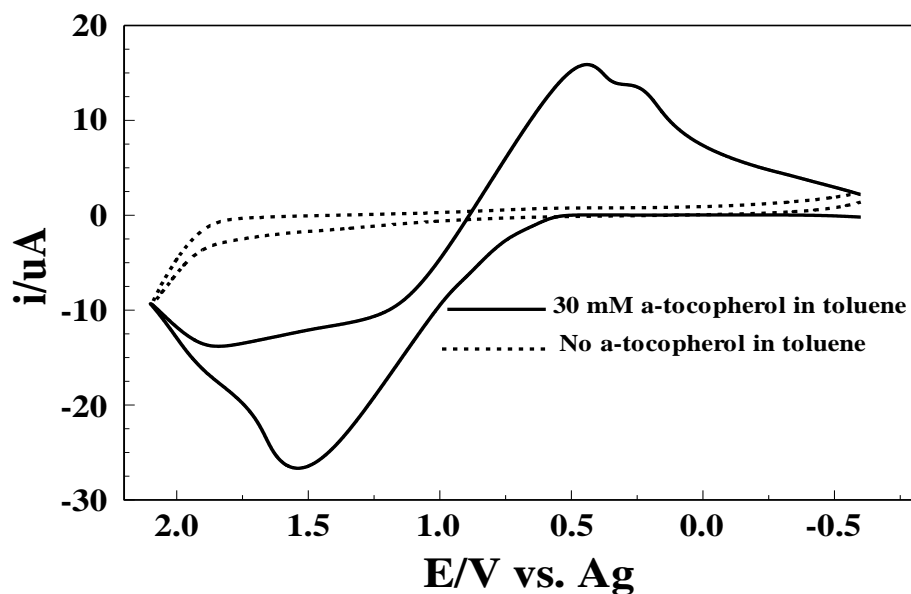

Figure 4.1 Voltammograms of Pt (diameter = 1 mm) in 30 mM a-tocopherol solution (black solid curve) and without a-tocopherol (black dashed curve) in 500 mM IL-PA in toluene at a scan rate of 0.1 V/s.

As shown in Figure 4.1, two peaks were seen centered at around 1.65 V and 0.38 V vs. Ag wire corresponding to the oxidation of α-TOH, and reduction of α-TO$^+$, respectively.[14] α-Tocopherol, like most phenolic compounds, undergoes a consecutive electron and proton transfer oxidation process (-1e$^-$/-H$^+$/-1e$^-$), as shown in Scheme 4.2.[18, 23] It has been demonstrated that α-TOH is initially oxidized by one electron to form a radical cation (α-TOH$^{+\bullet}$). The neutral radical (α-TO$^\bullet$) is formed rapidly by proton transfer of the radical cation, which is then immediately further oxidized to form the phenoxonium cation (α-TO$^+$).[14, 23] Therefore, the forward reaction process involves -1e$^-$/-H$^+$/-1e$^-$ steps to form α-TO$^+$. When the scan direction is reversed, the reduction process involves the transformation of α-TO$^+$ back to the starting material.[16] The peaks difference between the forward and reverse reactions is about 1.27 V. The relatively wide separation is because the electron transfers occur in two consecutive one-electron steps. Each step has a different formal electrode potential.[16, 24] Control experiments were conducted with the same experimental conditions, except without α-TOH in the solution. No redox signal was observed on the Pt working electrode for the potential scan range between -0.5 V to 2.1V vs. Ag wire, evidencing no interference signal from the supporting electrolyte and solvent. Figure 4.2 shows the voltammograms on a 10 μm Pt UME in bulk toluene solution with 500 mM IL-PA in the presence and absence of 30 mM α-TOH. The inset shows the oxidative potential window for toluene and IL-PA on the same working electrode for comparison. The sigmoidal wave shows the two-electron oxidation of α-TOH, and the oxidation starts at approximately 0.61 V vs. Ag wire and reaches a steady-state value at 1.5 V. Furthermore, the diffusion coefficient of α-TOH in toluene (500 mM IL-PA) was calculated by the steady-state current equation to be 3.26 x 10^{-6} cm^2 s^{-1}.[25] The electrochemical voltammograms of α-TOH in toluene solution indicate the potential range that

can be applied in the emulsion droplet collision experiments.
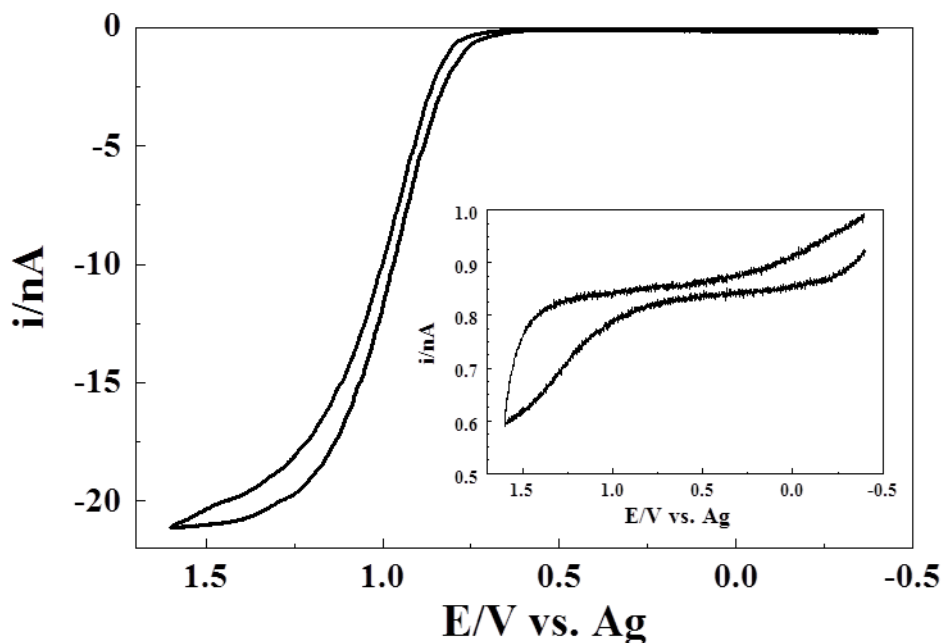
Figure 4.2 CV of 30 mM a-tocopherol and 500 mM IL-PA in toluene at Pt UME (diameter = 10 μm) at a scan rate of 60 mV/s. The potential scale was referred to the Ag quasi-reference electrode. The inset shows the potential window (60 mV/s) for 500 mM IL-PA in toluene without a-tocopherol on the same Pt UME vs. Ag as background.

4.4.2 Collision experiments of the toluene (α-tocopherol + IL-PA)/water emulsion droplets

The same toluene composition in 0.1 mL, by mixing with 4.9 mL of water, was used to create the emulsion for the collision experiments. The as-prepared emulsion was stable for at least 12 hours. Chronoamperometry (amperometric i-t curve) was used to observe the collisions of toluene (α-TOH + IL-PA)/water emulsion droplets on a Pt UME, which has been shown to be an effective method to study stochastic single electrochemical events.[20, 26] In Figure 4.3 (A), many current spikes with individual current transient behaviors appeared on a chronoamperogram of the toluene (α-TOH + IL-PA)/water emulsion. These current spikes are generated whenever a single emulsion droplet collides on the surface of Pt UME, resulting in the oxidation of α-TOH to α-TO$^+$ inside the toluene emulsion droplets. A background experiment

was performed under identical experimental conditions, except without α-TOH inside emulsion droplets. As shown in Figure 4.3 (B), no current spikes were detected during the collision experiments, which means these current spikes are only due to oxidation of α-TOH in the emulsion droplet. Typical oxidation (Faradaic) spikes are magnified and shown in Figure 4.3 (C-D). This observation supports the mechanism presented in Scheme 4.2, which shows current spikes are only observed when redox active species inside droplets are oxidized. The number of current spikes in Figure 4.3 (A) is related to diffusion flux and possibly migration of emulsion droplets to the electrode surface. The diffusion coefficient of a spherical emulsion droplet (D_{ems}) can be estimated by the Stokes-Einstein Equation 4.3, and the collision frequency (f) of emulsion droplets by diffusion can be calculated by Equation 4.4.

$$D_{ems} = \frac{k_B T}{6\pi\eta r_{ems}}$$
<div align="right">Equation 4.3</div>

$$f = 4D_{ems}C_{ems}r_{electrode}N_A$$
<div align="right">Equation 4.4</div>

where k_B is the Boltzmann constant, T is temperature, η is the viscosity of water at 25 °C, and r_{ems} is the radius of droplet, given by Equation 4.3; where f is the collision frequency, C_{ems} is the concentration of the emulsion droplets, $r_{electrode}$ is the radius of the Pt UME, and N_A is Avogadro's number, given by Equation 4.4. The diffusion coefficient of a 3.7 μm diameter emulsion droplet, calculated via the Stokes-Einstein approximation Equation 4.3, is 1.16×10^{-9} cm^2/s. Using Equation 4.4, the predicted collision frequency of toluene (30 mM α-TOH + 500 mM IL-PA)/water emulsion droplet by diffusion is 0.007 Hz. The experimentally observed frequency is 0.04 ± 0.01 Hz, which is nearly 6 times larger than the frequency predicted by diffusion alone. The discrepancy may be caused by the migration of droplets. However, migration effects are not significant compared with diffusion because there is a small

background faradaic reaction contributed by the migrational electric field.[27]

Figure 4.3 (A) Amperometric i-t curve of the collisions of the 0.12 pM toluene emulsion droplets (30 mM a-tocopherol + 500 mM IL-PA) on the Pt UME (diameter = 10 μm) biased at 1.2 V vs. Ag wire. (B) i-t curve for toluene (0 mM a-tocopherol + 500 mM IL-PA) emulsion droplets; (C-D) Magnified i-t curves showing the clear spike-type responses. The experimental data were sampled every 50 ms.

Chronoamperograms in deaerated toluene emulsion were recorded with various applied potentials with a duration time of 1000 s. The applied potentials turned out to affect the individual current spikes as shown in Figure 4.4 (A). The current spikes were not detected when the applied potential was lower than 0.30 V. As the potential became larger, more current spikes appeared and larger peak currents (i_{spike} as shown in Figure 4.3 (D)) were obtained. The average peak currents ($i_{spike-avg}$) were calculated and plotted against the applied potential, ranging from
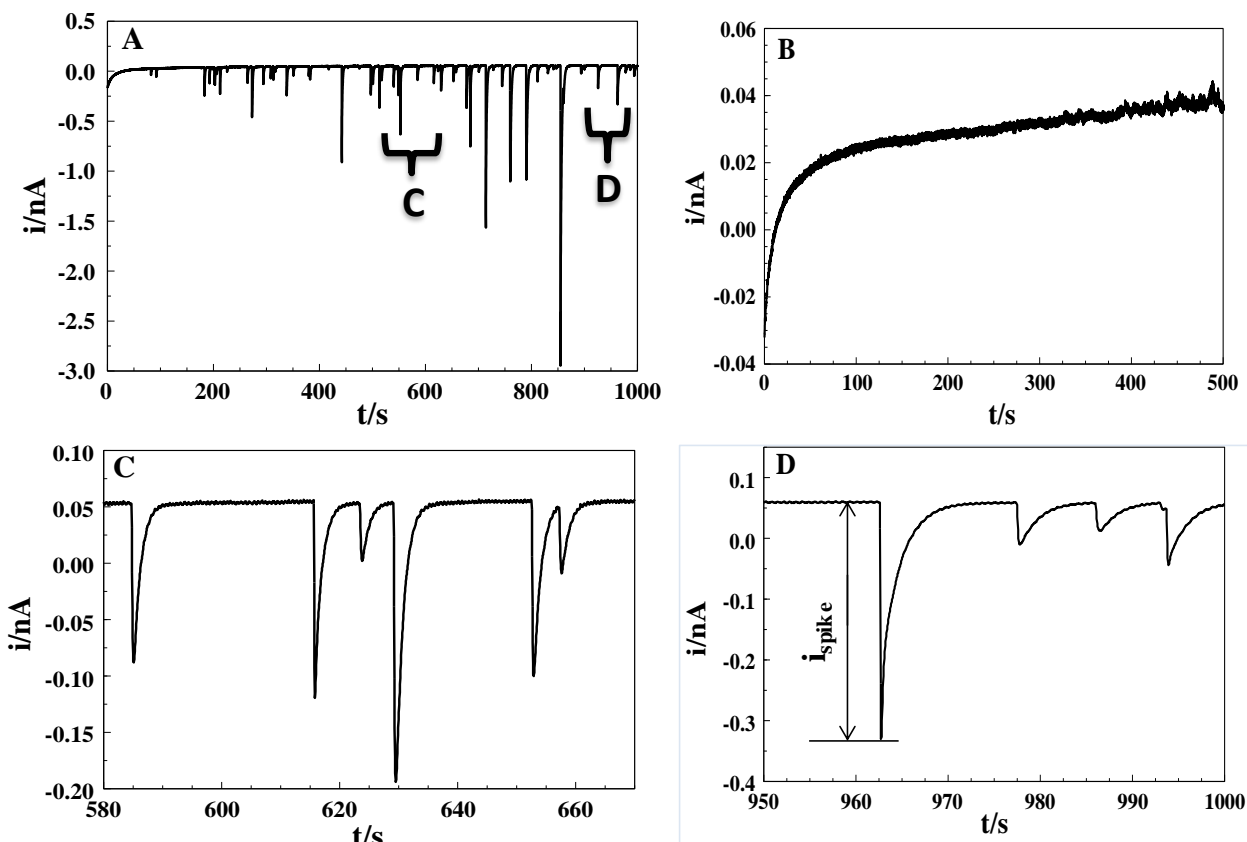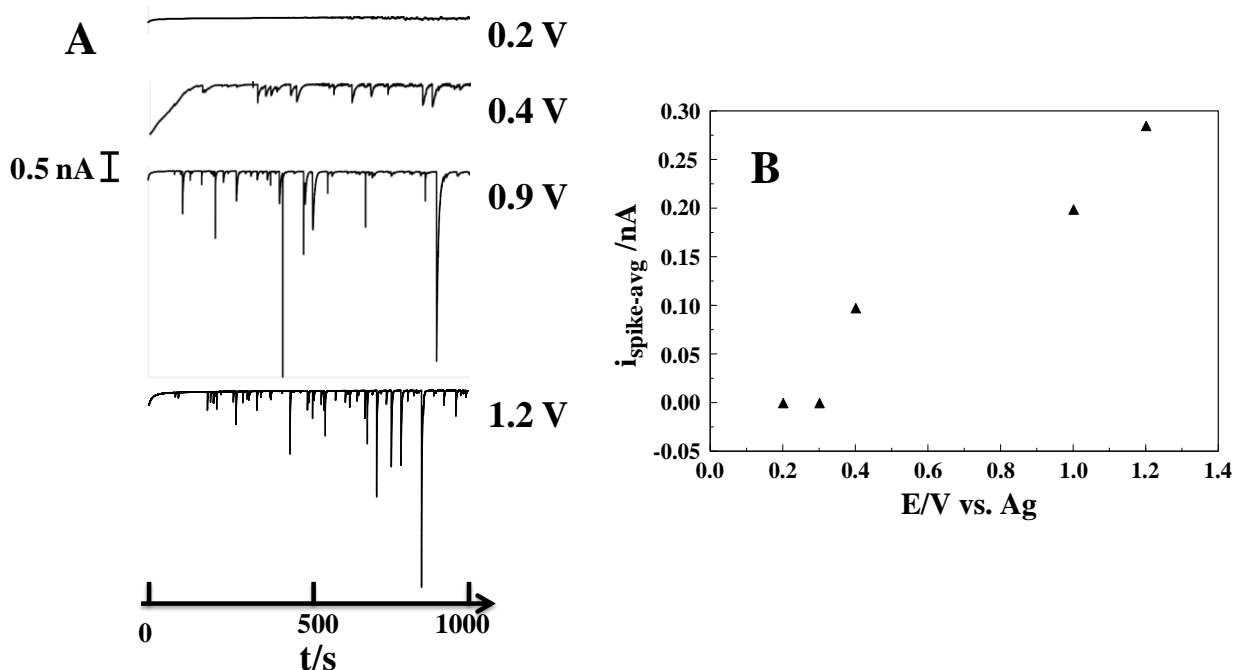
Figure 4.4 (A) Amperometric i-t curve of the collisions of the 0.12 pM toluene emulsion droplets (30 mM a-tocopherol + 500 mM IL-PA) on the Pt UME (diameter = 10 μm) by stepping potentials from 0.2 V to 1.2 V. (B) $i_{spike-avg}$ (black triangle) obtained from individual current spikes in chronoamperograms of the same emulsion droplets.

0.2 to 1.2 V. In Figure 4.4 (B), $i_{spike-avg}$ increased rapidly from 0.3 to 1.2 V. The curve can be obtained by connecting these $i_{spike-avg}$ points which can be considered as the polarization curve of the electro-oxidation of α-TOH in toluene solution because the current spike is entirely from toluene droplet. Interesting, Figure 4.4 B is correlated to the cyclic voltammogram of Figure 4.2. It shows that electro-oxidation of α-TOH on Pt UME occurs similarly in both the bulk toluene solution and toluene emulsion droplets.[28] The onset potential for the electro-oxidation of α-TOH in toluene droplets is less than 0.4 V, while the value for α-TOH in the bulk toluene solution is greater than 0.5 V. This finding means that it is easier to electro-oxidize α-TOH in toluene emulsion droplets than it is in toluene solution because the hydrogen-bonding interactions between the phenolic hydrogen atom and trace water in toluene shift the oxidation peak potential

of α-TOH to less positive potentials, which was similarly observed for the electrochemical

oxidation of α-TOH in acetonitrile with low levels of water reported by Webster et al.[29]

Upon collision with the electrode surface, α-TOH in the droplet is electrolyzed. The

current blip response can be integrated versus time to yield the amount of charge passed in a

single emulsion droplet. Faraday's Law, as shown in Equation 4.5, can be employed to calculate

the charge. From the calculated charge, the diameter of the droplets in this system can be

estimated by using Equation 4.6. The following equations are used to obtain the size distribution

of droplets:

$$Q = \int i dt \qquad \qquad \text{Equation 4.5}$$

$$d_{drop} = \sqrt[3]{\frac{6Q}{n\pi F C_{redox}}} \qquad \qquad \text{Equation 4.6}$$

where Q is the integrated charge from the spike peak, n is the stoichiometric number of electrons,

F is the Faraday's constant, and C_{redox} is the concentration of redox active species in the

dispersed phase. The mean charge (Q_{avg}) of individual spikes was calculated and plotted as a

function of potential, as shown in Figure 4.5. The charge values of 0 pC were given when the

applied potential was less than 0.3 V since no spikes were observed from the collision

experiments. A sigmoidal-shaped curve, in which Q_{avg} increased rapidly from 0.3 V to 0.9 V and

then leveled off at 1.2 V, was obtained. A representative chronoamperogram at 1.2 V is shown in

Figure 4.3 (A), assuming the redox active species inside the droplet were completely

electrolyzed at this potential, which was reported by Bard et al.[20-21, 26, 28] Each droplet has

spherical geometry and the concentration of α-TOH is 30 mM throughout the range of droplet

sizes. The calculated average size of the droplets was 4.2 ± 0.4 μm. The calculated size

distribution by Equation 4.6 agreed with the DLS data in Figure 4.6, indicating that the

assumption of bulk electrolysis was reasonable in interpreting the electrochemical results.[30] An

electrochemical size distribution (histogram) suggests that most of the droplets were 3.2 − 4.8 µm in diameter. The DLS (red line) indicates that the peak diameter was 3.7 µm. The size distributions from the two techniques are quite similar. Even DLS is an important tool for charactering the size of particles in solutions, the particles in heterogeneous samples with broad size distributions (PdI > 0.7) can be problematic. The presence of the larger particles will dominate the light scattering signal and mask the presence of small particles. The very small (< 20 nm) nanoparticles are mostly absorbing and will scatter very little light which will lead to inaccurate results. Therefore, some large droplets 5 - 6.5 µm and small droplets < 1.5 µm were detected by electrochemical collision experiments which were not detected by DLS methodology, demonstrating the advantage of the particle collision method presented here.[28, 30]
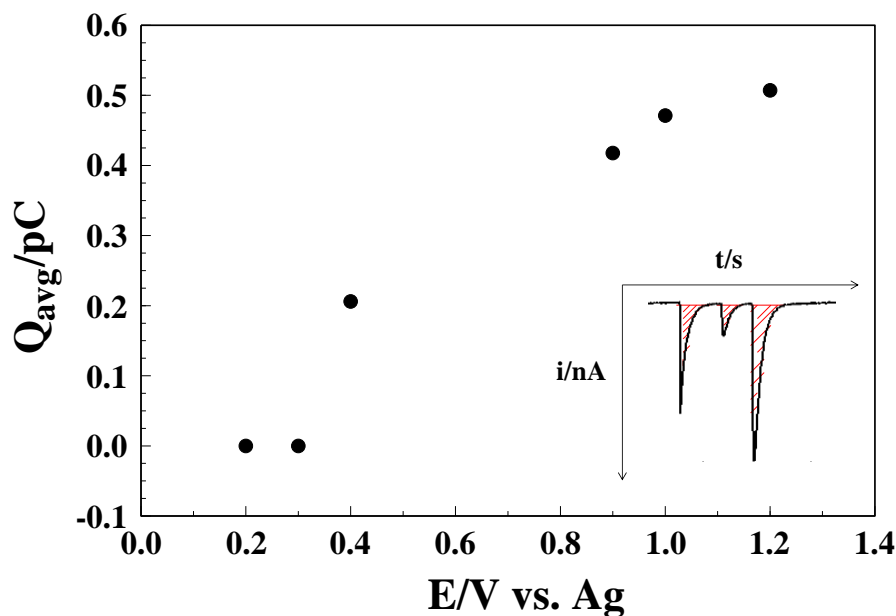
Figure 4.5 Calculated charge average (Q_{avg}) of the collisions of the 0.12 pM toluene emulsion droplets (30 mM a-tocopherol + 500 mM IL-PA) on the Pt UME (diameter = 10 µm) by stepping potentials from 0.2 V to 1.3 V. The inset shows the i-t curve can be integrated to calculate the charge transferred to the electrode for a given collision event from α-TOH oxidation in the droplet.
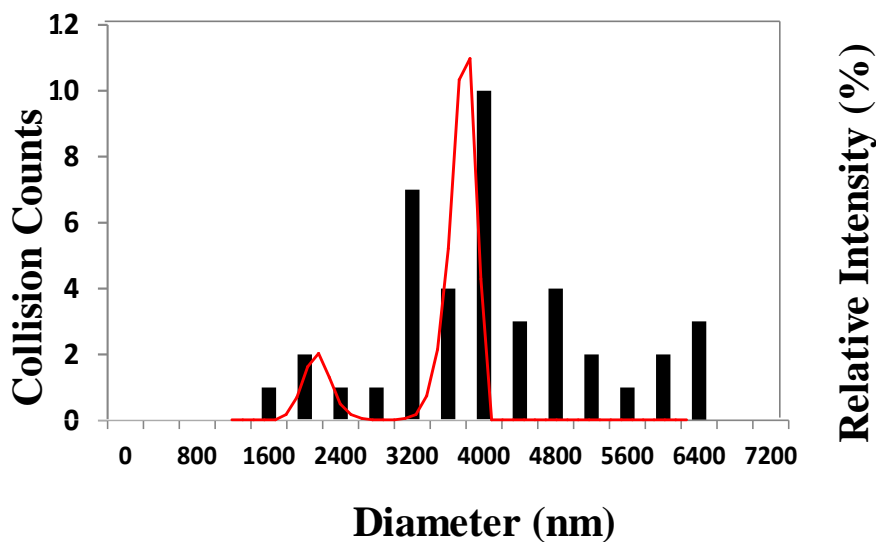
Figure 4.6 Comparison of calculated data vs DLS data. Black bars represent the calculated data and the red solid line represents the DLS data.

As shown in Figure 4.3 (C-D), the shape of the current spikes decayed exponentially with time after a rapid increase. The time when a droplet collides and adsorbs on the Pt UME surface, varies from 0.5 to 5 s. The thickness of the diffusion layer (δ) of α-TOH in toluene solution was estimated to be 18.1 to 57.1 μm by the following equation:

$$\delta = \sqrt{2Dt}$$

Equation 4.7

where δ is the thickness of diffusion layer, D is the diffusion coefficient of α-TOH in toluene solution (3.26×10^{-6} cm^2/s), and t is the time for the homogeneous electrolysis processing of α-TOH in toluene. The single toluene droplet can be considered as a small electrochemical reactor. The diffusion layer of α-TOH in toluene solution was larger than the diameter of the calculated droplet diameter (4.2 ± 0.4 μm). This suggests α-TOH inside the droplet can be fully electrolyzed. The bulk electrolysis model was applied for this emulsion system which agrees with results reported by several research groups.[20-21, 28, 31] It suggests that when the droplet

attaches to the surface of the working electrode upon collision, the reactor will open up and expose its contents to the active surface of Pt for electrolysis.[30] Therefore, an increase in contact area which represents the electrochemical droplet touching the electrode surface, will result in an increase in the current at each current spike. The decay of the current is because of the depletion of α-TOH in the droplet during the electrolysis, which is consistent with the i-t behavior of α-TOH in toluene solution. Overall, these results indicate that the hydrophobic redox active species in the toluene emulsion droplet follows the bulk electrolysis model.

4.5 Conclusions

In the present work, the oxidation of α-tocopherol in toluene emulsion droplets was first observed by the single particle collision method using an ultra-microelectrode. First, we demonstrated the electrochemical oxidation of α-tocopherol in toluene organic solvent with extremely low dielectric constants. The current spikes showed up when the collisions occurred during the experiment. By quantitatively analyzing the spike-type current response, the diffusion coefficient, collision frequency, and size distribution of the emulsion droplets were also addressed. The voltammetric behavior of α-tocopherol in a single toluene droplet was similar to that in the toluene solution. It suggests that the electroactive redox contents in the toluene droplets follow the bulk electrolysis model, and that bulk electrolysis can be achieved in a few seconds in these femtolitre reactors. The work presented here also showed that in the presence of water, the onset potential for the oxidation of α-TOH in single droplet shifts to a less positive value compared with that in pure toluene bulk solution. It indicated that the phenolic hydrogen atom most likely undergoes weak hydrogen-bonding interactions with water. The oxidized product diamagnetic cation can quickly react with water to form hemiketal.[29] Our results imply that the three-phase boundary (toluene/water/platinum) and the toluene/water

boundary are important in electrolysis considerations about this droplet system.[21] It would be possible to use particle collision strategy as an analytical technique to examine the oxidative behavior of vitamin E within phospholipids, ultimately to gain more mechanistic details for the functions of vitamin E in biological systems.

4.6 List of references

1.   Rigotti, A., Absorption, transport, and tissue delivery of vitamin E. *Mol. Asp. Med.* **2007,** *28* (5-6), 423-436.

2.   DellaPenna, D., A decade of progress in understanding vitamin E synthesis in plants. *J. Plant Physiol.* **2005,** *162* (7), 729-737.

3.   Azzi, A., Molecular mechanism of alpha-tocopherol action. *Free Radic. Biol. Med.* **2007,** *43* (1), 16-21.

4.   Atkinson, J.; Epand, R. F.; Epand, R. M., Tocopherols and tocotrienols in membranes: A critical review. *Free Radic. Biol. Med.* **2008,** *44* (5), 739-764.

5.   Burton, G. W.; Ingold, K. U., Vitamin E Application of the Principles of Physical Organic Chemistry to the Exploration of its Structure and Function. *Accounts of Chemical Research* **1986,** *19* (7), 194-201.

6.   Niki, E.; Noguchi, N., Dynamics of antioxidant action of vitamin E. *Accounts of Chemical Research* **2004,** *37* (1), 45-51.

7.   Wang, X. Y.; Quinn, P. J., The location and function of vitamin E in membranes (review). *Mol. Membr. Biol.* **2000,** *17* (3), 143-156.

8.   Boscoboinik, D.; Szewczyk, A.; Hensey, C.; Azzi, A., Inhibition of Cell Proliferation by Alpha- Tocopherol Role of Protein Kinase C. *J. Biol. Chem.* **1991,** *266* (10), 6188-6194.

9.   Traber, M. G.; Arai, H., Molecular mechanisms of vitamin E transport. *Annu. Rev. Nutr.* **1999,** *19*, 343-355.

10.   Ricciarelli, R.; Zingg, J. M.; Azzi, A., The 80th anniversary of vitamin E: Beyond its antioxidant properties. *Biological Chemistry* **2002,** *383* (3-4), 457-465.

11.   Tasinato, A.; Boscoboinik, D.; Bartoli, G. M.; Maroni, P.; Azzi, A., d-alpha-tocopherol inhibition of vascular smooth muscle cell proliferation occurs at physiological concentrations, correlates with protein kinase C inhibition, and is independent of its antioxidant properties. *Proceedings of the National Academy of Sciences* **1995,** *92* (26), 12190-12194.

12.   Brown, D. A.; London, E., Structure and origin of ordered lipid domains in biological membranes. *J. Membr. Biol.* **1998,** *164* (2), 103-114.

13.   Wilson, G. J.; Lin, C. Y.; Webster, R. D., Significant differences in the electrochemical behavior of the alpha-, beta-, gamma-, and delta-tocopherols (vitamin E). *Journal of Physical Chemistry B* **2006,** *110* (23), 11540-11548.

14.   Webster, R. D., New insights into the oxidative electrochemistry of vitamin E. *Accounts of Chemical Research* **2007,** *40* (4), 251-257.

15.   Peng, H. M.; Choules, B. F.; Yao, W. W.; Zhang, Z. Y.; Webster, R. D.; Gill, P. M. W., Long-lived radical cations as model compounds for the reactive one-electron oxidation product of vitamin E. *Journal of Physical Chemistry B* **2008,** *112* (33), 10367-10374.

16.   Lee, S. B.; Lin, C. Y.; Gill, P. M. W.; Webster, R. D., Transformation of alpha-tocopherol (vitamin E) and related chromanol model compounds into their phenoxonium ions by chemical oxidation with the nitrosonium cation. *J. Org. Chem.* **2005,** *70* (25), 10466-10473.

17.   Peng, H. M.; Webster, R. D., Investigation into phenoxonium cations produced during the electrochemical oxidation of chroman-6-ol and dihydrobenzofuran-5-ol substituted compounds. *J. Org. Chem.* **2008,** *73* (6), 2169-2175.

18.   Yue, Y. N.; Novianti, M. L.; Tessensohn, M. E.; Hirao, H.; Webster, R. D., Optimizing the lifetimes of phenoxonium cations derived from vitamin E via structural modifications. *Organic & Biomolecular Chemistry* **2015,** *13* (48), 11732-11739.

19.   Marquardt, D.; Williams, J. A.; Kucerka, N.; Atkinson, J.; Wassall, S. R.; Katsaras, J.; Harroun, T. A., Tocopherol Activity Correlates with Its Location in a Membrane: A New Perspective on the Antioxidant Vitamin E. *Journal of the American Chemical Society* **2013,** *135* (20), 7523-7533.

20.   Kim, B. K.; Boika, A.; Kim, J.; Dick, J. E.; Bard, A. J., Characterizing Emulsions by Observation of Single Droplet Collisions-Attoliter Electrochemical Reactors. *Journal of the American Chemical Society* **2014,** *136* (13), 4849-4852.

21.   Dick, J. E.; Lebegue, E.; Strawsine, L. M.; Bard, A. J., Millisecond Coulometry via Zeptoliter Droplet Collisions on an Ultramicroelectrode. *Electroanalysis* **2016,** *28* (10), 2320-2326.

22.   Geng, L.; Ewing, A. G.; Jernigan, J. C.; Murray, R. W., Electrochemical Reactions of Solutes and of Electroactive Polymer-Films in Low Dielectric Media - Toluene and Heptane. *Analytical Chemistry* **1986,** *58* (4), 852-860.

23.   Marcus., M. F.; HAWLEY., M., Electrochemical studies of the redox behavior of α-tocopherol. *Biochimica et Biophysica Acta* **1970,** *201* (1), 1-8.

24.   Huynh, M. H. V.; Meyer, T. J., Proton-coupled electron transfer. *Chem. Rev.* **2007,** *107* (11), 5004-5064.

25.   Malyszko, J.; Karbarz, M., Electrochemical oxidation of trolox and alpha-tocopherol in acetic acid: A comparative study. *J. Electroanal. Chem.* **2006,** *595* (2), 136-144.

26.   Kim, B. K.; Kim, J.; Bard, A. J., Electrochemistry of a Single Attoliter Emulsion Droplet in Collisions. *Journal of the American Chemical Society* **2015,** *137* (6), 2343-2349.

27.   Boika, A.; Thorgaard, S. N.; Bard, A. J., Monitoring the Electrophoretic Migration and Adsorption of Single Insulating Nanoparticles at Ultramicroelectrodes. *Journal of Physical Chemistry B* **2013,** *117* (16), 4371-4380.

28.   Park, S.; Kim, H.; Chae, J.; Chang, J., Electrochemical Generation of Single Emulsion Droplets and In Situ Observation of Collisions on an Ultramicroelectrode. *J. Phys. Chem. C* **2016,** *120* (7), 3922-3928.

29.   Tan, Y. S.; Chen, S. S.; Hong, W. M.; Kan, J. M.; Kwek, E. S. H.; Lim, S. Y.; Lim, Z. H.; Tessensohn, M. E.; Zhang, Y. L.; Webster, R. D., The role of low levels of water in the electrochemical oxidation of alpha-tocopherol (vitamin E) and other phenols in acetonitrile. *Physical Chemistry Chemical Physics* **2011,** *13* (28), 12745-12754.

30.   Li, Y.; Deng, H. Q.; Dick, J. E.; Bard, A. J., Analyzing Benzene and Cyclohexane Emulsion Droplet Collisions on Ultramicroelectrodes. *Analytical Chemistry* **2015,** *87* (21), 11013-11021.

31.   Sokolov, S. V.; Eloul, S.; Katelhon, E.; Batchelor-McAuley, C.; Compton, R. G., Electrode-particle impacts: a users guide. *Physical Chemistry Chemical Physics* **2017,** *19* (1), 28-43.

Chapter 5: Summary

Mechanistic studies of proton-coupled electron transfer reactions help to interpret experimental results as well as provide predictions for future experiments. This dissertation has demonstrated that variations in parameters impact the reaction mechanisms of PCET reactions. Specific parameters that have been studied in this work are oxidant potentials, buffer concentration, pH values, solvents, and pK_a values.

In chapter 2, we examined the effects of the oxidant-base pairs to PCET reactions. The results support that the stepwise pathways would be dominate when experimental conditions stabilize the intermediates of electron transfer or proton transfer, while concerted reactions will occur when those intermediates are unstable. Theoretical calculations have indicated that the maximum value of KIE should be reached when the difference in basicity of base and acid is equal to zero. We propose that the maximum level of concerted reactions for a PCET reaction should occur when PT and ET coincide at a thermoneutral point by means of the pKa and E°' of the studied species. The rate of the concerted pathway should reach the maximum value and attain the limit thermodynamic efficiency in this ideal thermoneutral state. Experimental support of this prediction has been lacking. These insights could be applied to design artificial systems for production of energy using more abundant reagents with lower cost and higher efficiency involving PCET reactions. In chapter 3, we provided an explanation for the differences of the oxidation mechanism of Trolox in aqueous and nonaqueous solutions with various pH values. We conclude that nucleophiles in the background electrolyte strongly influence the stability of

phenoxonium cations. The cross-conjugated ketone is the final product for the oxidation of Trolox in acetonitrile, while quinone is the major final product for the redox reaction of Trolox in water solutions. Our results provide a possible way to improve the Trolox Equivalent Antioxidant Capacity (TEAC) assay in both aqueous and lipophilic systems. In chapter 4, the oxidation of α-tocopherol was studied by particle collision methods. The electroactive redox contents in the toluene droplets follow the bulk electrolysis model. The onset potential for the oxidation of α-tocopherol in single droplet shifts in the presence of water. Our results imply that the toluene/water boundaries are useful to examine the oxidation behavior of α-tocpherol within phospholipids in order to gain more information for the functions of vitamin E in biological systems.

In this dissertation we use electrochemical techniques to observe PCET reactions. By studying the oxidation reactions of glutathione, Trolox, and α-tocopherol models, we provided more detailed explanations of their proton transfer and electron transfer mechanisms. All these results can help us to make predictions of how the variation of experimental parameters will affect the experimental systems.

Appendix 2 (Chapter 2)

Appendix 2A. Calculation of $\Delta G^{\circ'}_{PT}$ and $\Delta G^{\circ'}_{ET}$ of Table 2.6

Appendix 2B. Diffusion coefficients of GSH, mediators and buffers components

Appendix 2C. Simulation of experimental CV response of GSH and $Fe(phen)_3SO_4$ at various scan rates.

Appendix 2D. Simulation of experimental CV response of GSH and $K_4Mo(CN)_8$ at various scan rates

Appendix 2E. Parameters used in digital simulations of cyclic voltammograms

Appendix 2F. Determination of heterogeneous rate constants using the method of Nicholson

Appendix 2G. List of references

Appendix 2A. Calculation of $\Delta G^{\circ'}{}_{PT}$ and $\Delta G^{\circ'}{}_{ET}$ of Table 2.6

Detailed procedure for the calculation of $\Delta G^{\circ'}{}_{PT}$ and $\Delta G^{\circ'}{}_{ET}$ shown in Table 2.6 (Chapter 2):

The redox potentials for mediators were determined from half-wave redox potentials of experimental cyclic voltammograms at various scan rates. The apparent redox potentials for mediators were: $E^0{}_{app}(Mo(CN)_8{}^{3-}/Mo(CN)_8{}^{4-})$ = 0.583 V vs. Ag/AgCl; $E^0{}_{app}(IrCl_6{}^{2-}/IrCl_6{}^{3-})$ = 0.730 V vs. Ag/AgCl; $E^0{}_{app}(Fe(phen)_3{}^{3+}/Fe(phen)_3{}^{2+})$ = 0.827 V vs. Ag/AgCl. Eq. S1 reported by Madej was used to calculate the $E^0{}_{app}$ values of GSH in buffered solutions.[1] Here, pK_a value for thiol group of GSH is 8.7 (pK_{aSH}); $E^0(GS^{\bullet}/GS^-)$ = 0.58 V vs. Ag/AgCl, pH = pK_a.

$$E^{\circ}_{app}(GS^{\bullet}, H^+/GS^-) = E^{\circ}(GS^{\bullet}/GS^-) + 0.059 \log\left(1 + \frac{H^+}{K_{aSH}}\right) \qquad \text{Eq. 2A1}$$

When pH = 5.1, $E^0{}_{app}(GS^{\bullet}, H^+/GS^-)$ = 0.58 + 0.059 log (1 + $\frac{10^{-5.1}}{10^{-8.7}}$)= 0.792406 V;

pH = 5.6, $E^0{}_{app}(GS^{\bullet}, H^+/GS^-)$ = 0.58 + 0.059 log (1 + $\frac{10^{-5.6}}{10^{-8.7}}$) = 0.762920 V;

pH = 6.2, $E^0{}_{app}(GS^{\bullet}, H^+/GS^-)$ = 0.58 + 0.059 log (1 + $\frac{10^{-6.2}}{10^{-8.7}}$) = 0.727581 V;

pH = 6.5, $E^0{}_{app}(GS^{\bullet}, H^+/GS^-)$ = 0.58 + 0.059 log (1 + $\frac{10^{-6.5}}{10^{-8.7}}$) = 0.709961 V;

pH = 7.2, $E^0{}_{app}(GS^{\bullet}, H^+/GS^-)$ = 0.58 + 0.059 log (1 + $\frac{10^{-7.2}}{10^{-8.7}}$) = 0.669298 V.

Concerted mechanism was obtained for the mediated oxidation of GSH in the range of pH values below pK_{aSH} (8.7). Eq. 2A2 and Eq. 2A3 show the concerted rate-determining step followed by the fast dimerization of the thiyl radical.

$$GSH + M^+ + B \rightleftharpoons GS^{\bullet} + M + BH^+ \quad \text{Eq. 2A2} \qquad GS^{\bullet} + GS^{\bullet} \rightleftharpoons GSSG \qquad \text{Eq. 2A3}$$
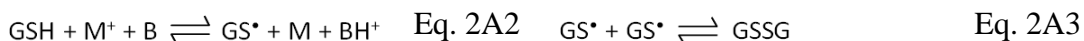
According to the relationship between Gibbs free energy change, $\Delta G^{\circ'}$, and equilibrium constants, the driving force for proton transfer (PT) was calculated by Eq. 2A4, where, R =

8.314462 J mol^{-1} K^{-1}, T = 298 K, 1 eV = 1.60218 x 10^{-19} J, Avogadro constant N$_A$ = 6.022 x 10^{23} mol^{-1}, pH = pK$_a$.

$$\Delta G^{\circ\prime}_{PT} = -RT ln(\frac{K_{aSH}}{K_{a(base)}})$$

Eq. 2A4

When pH = 5.1, $\Delta G^{\circ\prime}_{PT} = -8.314462$ J mol^{-1}K^{-1} 298 K $ln(\frac{10^{-8.7}}{10^{-5.1}})$ = 20.53849 KJ mol^{-1} = $\frac{20.53849 \, X \, 1000}{(1.60218 \, X \, 10^{-19}) \, X \, (6.022 \, X \, 10^{23})}$ = 0.212871 eV;

pH = 5.6, $\Delta G^{\circ\prime}_{PT} = -8.314462$ J mol^{-1}K^{-1} 298 K $ln(\frac{10^{-8.7}}{10^{-5.6}})$ = 17.68593 KJ mol^{-1} = $\frac{17.68593 \, X \, 1000}{(1.60218 \, X \, 10^{-19}) \, X \, (6.022 \, X \, 10^{23})}$ = 0.183306 eV;

pH = 6.2, $\Delta G^{\circ\prime}_{PT} = -8.314462$ J mol^{-1}K^{-1} 298 K $ln(\frac{10^{-8.7}}{10^{-6.2}})$ = 14.26284 KJ mol^{-1} = $\frac{14.26284 \, X \, 1000}{(1.60218 \, X \, 10^{-19}) \, X \, (6.022 \, X \, 10^{23})}$ = 0.147827 eV;

pH = 6.5, $\Delta G^{\circ\prime}_{PT} = -8.314462$ J mol^{-1}K^{-1} 298 K $ln(\frac{10^{-8.7}}{10^{-6.5}})$ = 12.55130 KJ mol^{-1} = $\frac{12.55130 \, X \, 1000}{(1.60218 \, X \, 10^{-19}) \, X \, (6.022 \, X \, 10^{23})}$ = 0.130088 eV;

pH = 7.2, $\Delta G^{\circ\prime}_{PT} = -8.314462$ J mol^{-1}K^{-1} 298 K $ln(\frac{10^{-8.7}}{10^{-7.2}})$ = 8.557706 KJ mol^{-1} = $\frac{8.557706 \, X \, 1000}{(1.60218 \, X \, 10^{-19}) \, X \, (6.022 \, X \, 10^{23})}$ = 0.088696 eV.

The driving force of electron transfer (ET) reaction step was calculated by Eq. 2A5, where, M/M$^+$ represents mediator, n is the number of electron transfer, Faraday constant F = 96485 C mol^{-1}, 1 J (joules) = 1 V(volts) X 1 C (coulombs).

$$\Delta G^{\circ\prime}_{ET} = -nF(E^0_{app}(M/M^+) - E^0_{app}(GS^\bullet, H^+/GS^-))$$

Eq. 2A5

For the redox mediator Mo(CN)$_8{}^{3-}$/Mo(CN)$_8{}^{4-}$, when

pH = pK$_a$ = 5.1,

$\Delta G^{\circ\prime}_{ET} = -1 \, X \, 96485$ C mol^{-1}(0.583 V - 0.792406 V) = 20.20457 KJ mol^{-1} = $\frac{20.20457 \, X \, 1000}{(1.60218 \, X \, 10^{-19}) \, X \, (6.022 \, X \, 10^{23})}$ = 0.209410 eV;

pH = pK$_a$ = 5.6,

$$\Delta G^{\circ\prime}_{ET} = -1 \; X \; 96485 \; C \; mol^{-1}(0.583 \; V - \; 0.762920 \; V) \; = 17.3596 \; KJ \; mol^{-1} =$$
$$\frac{17.35961 \; X \; 1000}{(1.60218 \; X \; 10^{-19}) \; X \; (6.022 \; X \; 10^{23})} = 0.179924 \; eV;$$

pH = pK$_a$ = 6.2,

$$\Delta G^{\circ\prime}_{ET} = -1 \; X \; 96485 \; C \; mol^{-1}(0.583 \; V - \; 0.727581 \; V) \; = 13.94988 \; KJ \; mol^{-1} =$$
$$\frac{13.94988 \; X \; 1000}{(1.60218 \; X \; 10^{-19}) \; X \; (6.022 \; X \; 10^{23})} = 0.144583 \; eV;$$

pH = pK$_a$ = 6.5,

$$\Delta G^{\circ\prime}_{ET} = -1 \; X \; 96485 \; C \; mol^{-1}(0.583 \; V - \; 0.709961 \; V) \; = 12.24984 \; KJ \; mol^{-1} =$$
$$\frac{12.24984 \; X \; 1000}{(1.60218 \; X \; 10^{-19}) \; X \; (6.022 \; X \; 10^{23})} = 0.126963 \; eV;$$

pH = pK$_a$ = 7.2,

$$\Delta G^{\circ\prime}_{ET} = -1 \; X \; 96485 \; C \; mol^{-1}(0.583 \; V - \; 0.669298 \; V) \; = 8.326436 \; KJ \; mol^{-1} =$$
$$\frac{8.326436 \; X \; 1000}{(1.60218 \; X \; 10^{-19}) \; X \; (6.022 \; X \; 10^{23})} = 0.086299 \; eV;$$

The $\Delta G^{\circ\prime}_{ET}$ values for $IrCl_6^{2-}/IrCl_6^{3-}$ and $Fe(phen)_3^{3+}/Fe(phen)_3^{2+}$ were calculated using the same procedures for $Mo(CN)_8^{3-}/Mo(CN)_8^{4-}$ and correlated values were listed in Table 2.6.

Appendix 2B. Diffusion coefficients of GSH, mediators and buffers components

Species	Diffusion Coefficient/ 10^6 cm^2 s^{-1}
GSH	$(5.13 \pm 0.05)^a$
$IrCl_6^{2-}/IrCl_6^{3-}$	$(7.0 \pm 1.0)^b$
$Fe(phen)_3^{3+}/Fe(phen)_3^{2+}$	$(3.1 \pm 0.1)^b$
$Mo(CN)_8^{3-}/Mo(CN)_8^{4-}$	$(2.82 \pm 0.04)^b$
$H_2PO_4^-$	9.59^c
HPO_4^{2-}	7.59^c

Table 2B.1 Diffusion coefficient of all species used to simulate the cyclic voltammetry of GSH in the presence of different metal complexes and Brönsted bases B.

[a] Determined by Pulsed Gradient Echo (PGE) ^{1}H NMR as described in the experimental section; the diffusion coefficient of all the glutathione derived species (i.e. G$^•$, GG and G") was assumed to be the same as that of glutathione (G). [b] Estimated though digital simulation of cyclic voltammograms of aqueous solutions of 1.0 mM of metal complex alone. [c] Obtained from the CRC Handbook of Chemistry and Physics; the same diffusion coefficient was assumed for all deprotonation states of malic, succinic, citric and maleic species.

Appendix 2C. Simulation of experimental CV response of GSH and Fe(phen)$_3$SO$_4$ at various scan rates.

Figure 2C.1 Experimental (solid line) and simulated (open circles) CV response of 1.0 mM GSH + 1.0 mM Fe(phen)$_3$SO$_4$, at pH 10.00. Scan rates were 0.1, 0.3, 0.5 and 0.7 V s^{-1}.
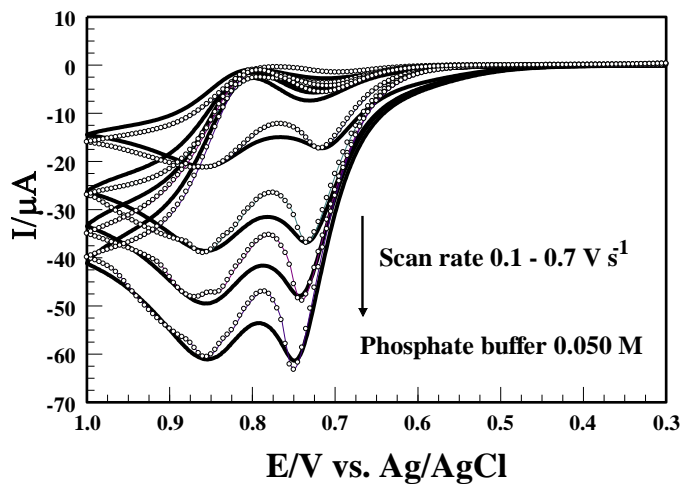
Figure 2C.2 Experimental (solid line) and simulated (open circles) CV response of 1.0 mM GSH + 1.0 mM Fe(phen)$_3$SO$_4$, at pH 10.00. Scan rates were 0.1, 0.3, 0.5 and 0.7 V s^{-1}.
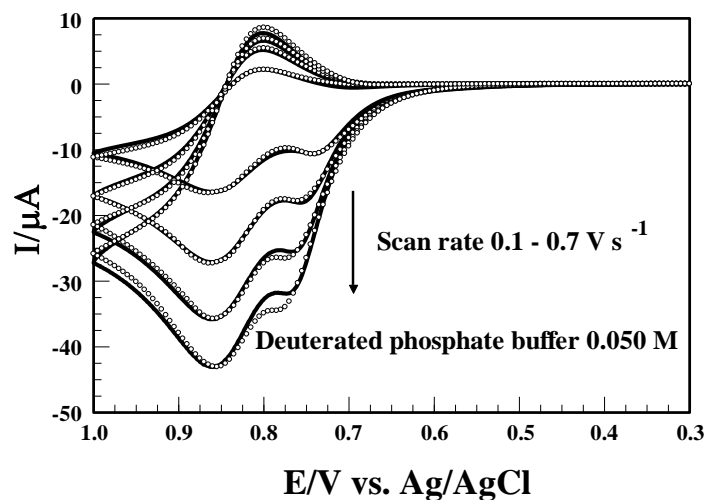
Figure 2C.3 Experimental (solid line) and simulated (open circles) CV response of 1.0 mM GSH + 1.0 mM Fe(phen)$_3$SO$_4$, at pD 10.00. Scan rates were 0.1, 0.3, 0.5 and 0.7 V s^{-1}.
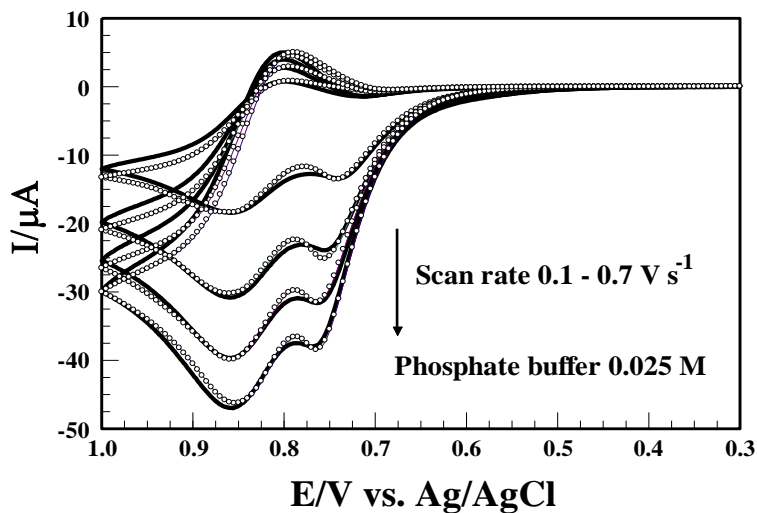

Figure 2C.4 Experimental (solid line) and simulated (open circles) CV response of 1.0 mM GSH + 1.0 mM Fe(phen)$_3$SO$_4$, at pD 10.00. Scan rates were 0.075, 0.1, 0.3 and 0.5 V s^{-1}. Appendix 2D. Simulation of experimental CV response of GSH and K$_4$Mo(CN)$_8$ at various scan
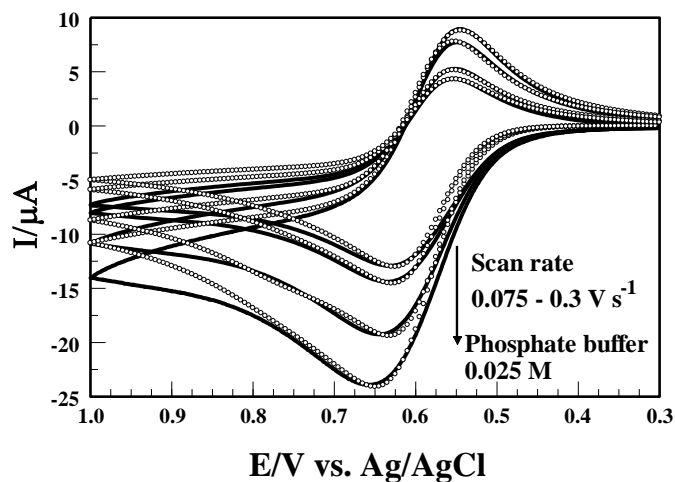
rates

Appendix 2D.1 Experimental (solid line) and simulated (open circles) CV response of 1.0 mM GSH + 1.0 mM K$_4$Mo(CN)$_8$, at pH 10.00. Scan rates were 0.075, 0.1, 0.2 and 0.3 V s^{-1}.
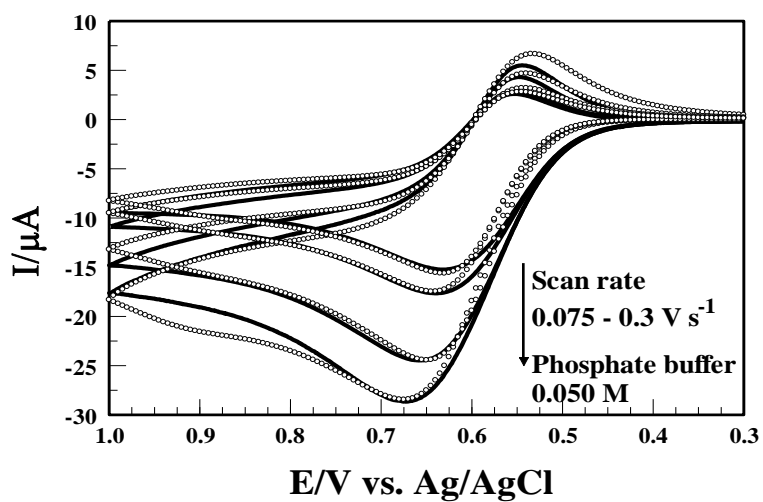
Appendix 2D.2 Experimental (solid line) and simulated (open circles) CV response of 1.0 mM GSH + 1.0 mM K$_4$Mo(CN)$_8$, at pH 10.00. Scan rates were 0.075, 0.1, 0.2 and 0.3 V s^{-1}.
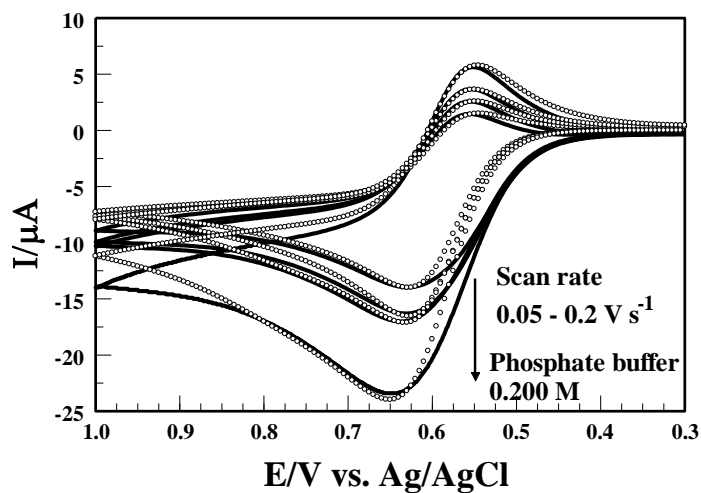
Appendix 2D.3 Experimental (solid line) and simulated (open circles) CV response of 1.0 mM GSH + 1.0 mM K$_4$Mo(CN)$_8$, at pH 10.00. Scan rates were 0.05, 0.075, 0.1 and 0.2 V s^{-1}.

Appendix 2D.4 Experimental (solid line) and simulated (open circles) CV response of 1.0 mM GSH + 1.0 mM K$_4$Mo(CN)$_8$, at pH 10.00. Scan rates were 0.05, 0.075, 0.1 and 0.2 V s^{-1}.
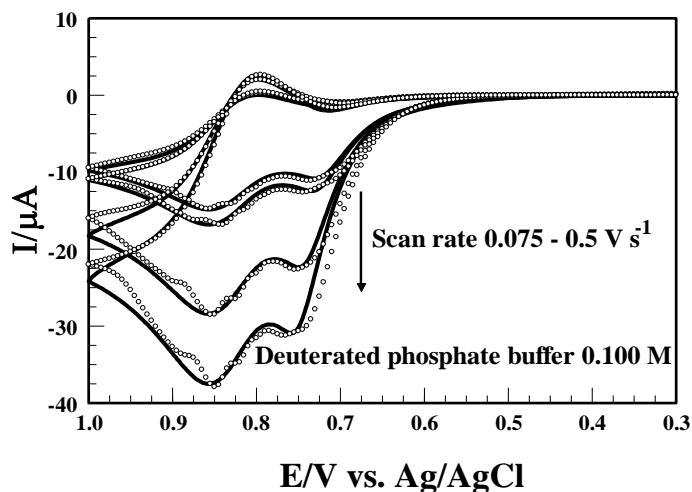
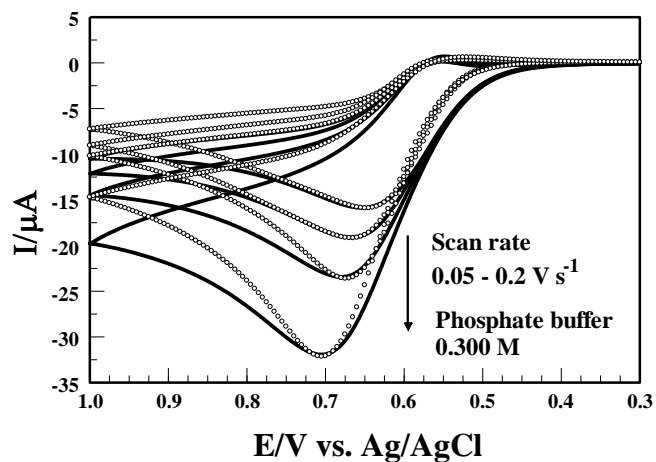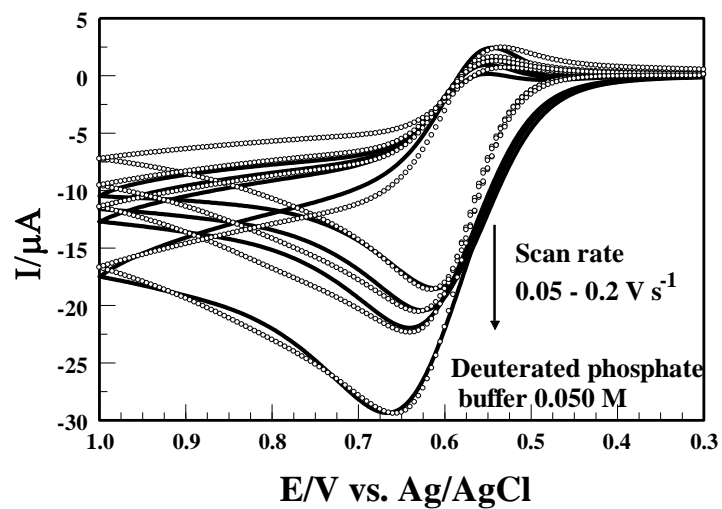**Appendix 2D.5** Experimental (solid line) and simulated (open circles) CV response of 1.0 mM GSH + 1.0 mM $K_4Mo(CN)_8$, at pD 10.00. Scan rates were 0.05, 0.075, 0.1 and 0.2 V s^{-1}.

Appendix 2E. Parameters used in digital simulations of cyclic voltammograms

The following are the electrochemical and kinetic parameters that best fitted the experimental voltammetry. The CV data for the oxidation of GSH by electrogenerated mediators recorded in DI water with various concentrations of phosphate buffer and 1.0 M NaCl as the supporting electrolyte at a 3 mm diameter glassy carbon electrode at room temperature. The values in the tables obtained from the average of the simulated electrochemical and kinetic parameters at various scan rates between $0.05 - 1$ V s^{-1}. The numbers on the left side of the parameter tables in the Appendix 2 mean the same number of the reaction steps of Table 2.1 and Table 2.2 in Chapter 2.

Units for fitted parameters: redox potential (E) : V ; diffusion coefficient (D) : cm^2 s^{-1} ; heterogeneous rate constant (k_s) : cm s^{-1}; transfer coefficient (α) : unitless ; homogeneous rate constants for the forward (k_f) and back (k_b) reactions: s^{-1} (first-order reactions), L mol^{-1} s^{-1} (second-order reactions) ; equilibrium constants (K_{eq}) : $K_{eq} = k_f/k_b$.

Simulations of CV experiments done at pH 10.00 and pD 10.00.
1.0 mM Fe(phen)$_3$SO$_4$ + 1.0 mM GSH + 25 mM phosphate buffer pH 10.00 + 1.0 M NaCl

#	Electrochemical Reactions	E	k_s	α
1	$Fe(phen)_3{}^{3+} + e^- = Fe(phen)_3{}^{2+}$	0.8285	0.1	0.5
3	$GS^{\bullet} + e- = GS^-$	0.5845	1.0×10^{-4}	0.5
	Chemical Reactions	K	k_f	k_b
2a	$GSH + PO_4{}^{3-} = GS^- + HPO_4{}^{2-}$	2×10^4	2×10^9	1
2b	$Fe(phen)_3{}^{3+} + GS^- = Fe(phen)_3{}^{2+} + GS^{\bullet}$	1.33×10^4	$(1.4\pm0.3) \times 10^7$	$(1.1\pm0.2) \times 10^3$
5	$Fe(phen)_3{}^{3+} + GS^{\bullet} = Fe(phen)_3{}^{2+} + GS"$	4.0×10^{11}	$(6.6\pm0.4) \times 10^6$	$(1.6\pm0.1) \times 10^{-5}$
4	$GS^{\bullet} + GS^{\bullet} = GSSG$	$(1.3\pm0.4) \times 10^9$	$(2.7\pm0.4) \times 10^9$	2.3 ± 0.8
6	$Fe(phen)_3{}^{3+} = P$	1.0×10^7	2.21×10^{-2}	2.21×10^{-9}

1.0 mM Fe(phen)$_3$SO$_4$ + 1.0 mM GSH + 50 mM phosphate buffer pH 10.00 + 1.0 M NaCl

#	Electrochemical Reactions	E	k_s	α
1	$Fe(phen)_3^{3+} + e^- = Fe(phen)_3^{2+}$	0.8225	0.1	0.5
3	$GS^{\bullet} + e- = GS^-$	0.5845	1.0×10^{-4}	0.5
	Chemical Reactions	K	k_f	k_b
2a	$GSH + PO_4^{3-} = GS^- + HPO_4^{2-}$	2×10^4	2×10^9	1
2b	$Fe(phen)_3^{3+} + GS^- = Fe(phen)_3^{2+} + GS^{\bullet}$	$(1.2\pm0.2) \times 10^4$	$(7.3\pm0.2) \times 10^7$	$(6.5\pm0.3) \times 10^3$
5	$Fe(phen)_3^{3+} + GS^{\bullet} = Fe(phen)_3^{2+} + GS"$	4.0×10^{11}	5.0×10^6	1.25×10^{-5}
4	$GS^{\bullet} + GS^{\bullet} = GSSG$	$(3\pm1) \times 10^8$	2.0×10^9	8.5 ± 0.4
6	$Fe(phen)_3^{3+} = P$	$(3.7\pm0.2) \times 10^7$	2.21×10^{-2}	$(1.0\pm0.1) \times 10^{-9}$

1.0 mM Fe(phen)$_3$SO$_4$ + 1.0 mM GSH + 100 mM phosphate buffer pH 10.00 + 1.0 M NaCl

#	Electrochemical Reactions	E	k_s	α
1	$Fe(phen)_3^{3+} + e^- = Fe(phen)_3^{2+}$	0.8225	0.1	0.5
3	$GS^{\bullet} + e- = GS^-$	0.5845	1.0×10^{-4}	0.5
	Chemical Reactions	K	k_f	k_b
2a	$GSH + PO_4^{3-} = GS^- + HPO_4^{2-}$	2×10^4	2×10^9	1
2b	$Fe(phen)_3^{3+} + GS^- = Fe(phen)_3^{2+} + GS^{\bullet}$	1.053×10^4	$(1.1\pm0.1) \times 10^8$	$(1.04\pm0.09) \times 10^3$
5	$Fe(phen)_3^{3+} + GS^{\bullet} = Fe(phen)_3^{2+} + GS"$	4.0×10^{11}	$(8\pm2)x 10^6$	$(2.0\pm0.4) \times 10^{-5}$
4	$GS^{\bullet} + GS^{\bullet} = GSSG$	$(1.9\pm0.9) \times 10^8$	$(6.3\pm0.2) \times 10^8$	4.1 ± 0.2
6	$Fe(phen)_3^{3+} = P$	4.0×10^7	2.21×10^{-2}	5.52×10^{-10}

1.0 mM Fe(phen)$_3$SO$_4$ + 1.0 mM GSH + 50 mM deuterated phosphate buffer pD 10.00 + 1.0 M NaCl

#	Electrochemical Reactions	E	k_s	α
1	Fe(phen)$_3^{3+}$ + e$^-$ = Fe(phen)$_3^{2+}$	0.8325	0.1	0.5
3	GS$^{\bullet}$ + e- = GS$^-$	0.5845	1.0×10^{-4}	0.5
	Chemical Reactions	**K**	k_f	k_b
2a	GSH + PO$_4^{3-}$ = GS$^-$ + HPO$_4^{2-}$	2×10^4	2×10^9	1
2b	Fe(phen)$_3^{3+}$ + GS$^-$ = Fe(phen)$_3^{2+}$ + GS$^{\bullet}$	1.553×10^4	7×10^6	450.61
5	Fe(phen)$_3^{3+}$ + GS$^{\bullet}$ = Fe(phen)$_3^{2+}$ + GS"	4.0×10^{11}	5.0×10^6	1.25×10^{-5}
4	GS$^{\bullet}$ + GS$^{\bullet}$ = GSSG	6×10^9	2.0×10^9	0.33
6	Fe(phen)$_3^{3+}$ = P	1.0×10^7	2.21×10^{-2}	2.21×10^{-9}

1.0 mM Fe(phen)$_3$SO$_4$ + 1.0 mM GSH + 100 mM deuterated phosphate buffer pD 10.00 + 1.0 M NaCl

#	Electrochemical Reactions	E	k_s	α
1	Fe(phen)$_3^{3+}$ + e$^-$ = Fe(phen)$_3^{2+}$	0.8325	0.1	0.5
3	GS$^{\bullet}$ + e- = GS$^-$	0.5845	1.0×10^{-4}	0.5
	Chemical Reactions	**K**	k_f	k_b
2a	GSH + PO$_4^{3-}$ = GS$^-$ + HPO$_4^{2-}$	2×10^4	2×10^9	1
2b	Fe(phen)$_3^{3+}$ + GS$^-$ = Fe(phen)$_3^{2+}$ + GS$^{\bullet}$	1.553×10^4	$(1.3 \pm 0.4) \times 10^8$	$(8.5 \pm 0.3) \times 10^3$
5	Fe(phen)$_3^{3+}$ + GS$^{\bullet}$ = Fe(phen)$_3^{2+}$ + GS"	4.0×10^{11}	$(1.7 \pm 0.8) \times 10^8$	$(4.2 \pm 0.2) \times 10^{-4}$
4	GS$^{\bullet}$ + GS$^{\bullet}$ = GSSG	6×10^9	2.0×10^9	0.33
6	Fe(phen)$_3^{3+}$ = P	1.0×10^7	2.21×10^{-2}	2.21×10^{-9}

1.0 mM K$_4$Mo(CN)$_8$ + 1.0 mM GSH + 25 mM phosphate buffer pH 10.00 + 1.0 M NaCl

#	Electrochemical Reactions	E	k$_s$	α
1	$Mo(CN)_8^{3-} + e^- = Mo(CN)_8^{4-}$	0.5916	0.03	0.5
3	$GS^{\bullet} + e- = GS^-$	0.5845	1.0×10^{-4}	0.5
	Chemical Reactions	**K**	**k$_f$**	**k$_b$**
2a	$GSH + PO_4^{3-} = GS^- + HPO_4^{2-}$	2×10^4	2×10^9	1
2b	$Mo(CN)_8^{4-} + GS^- = Mo(CN)_8^{3-} + GS^{\bullet}$	1.3182	$(2.87\pm0.06) \times 10^3$	$(2.17\pm0.04) \times 10^3$
5	$Mo(CN)_8^{4-} + GS^{\bullet} = Mo(CN)_8^{3-} + GS"$	1×10^5	1×10^5	0.1
4	$GS^{\bullet} + GS^{\bullet} = GSSG$	$(2.3\pm0.3) \times 10^{10}$	5.0×10^{10}	2.2 ± 0.2
6	$Mo(CN)_8^{4-} = P$	2.00×10^3	1.00×10^{-4}	5.00×10^{-8}

1.0 mM K$_4$Mo(CN)$_8$ + 1.0 mM GSH + 50 mM phosphate buffer pH 10.00 + 1.0 M NaCl

#	Electrochemical Reactions	E	k$_s$	α
1	$Mo(CN)_8^{3-} + e^- = Mo(CN)_8^{4-}$	0.5916	0.03	0.5
3	$GS^{\bullet} + e- = GS^-$	0.5845	1.0×10^{-4}	0.5
	Chemical Reactions	**K**	**k$_f$**	**k$_b$**
2a	$GSH + PO_4^{3-} = GS^- + HPO_4^{2-}$	2×10^4	2×10^9	1
2b	$Mo(CN)_8^{4-} + GS^- = Mo(CN)_8^{3-} + GS^{\bullet}$	1.3182	$(4.2\pm0.7) \times 10^3$	$(3.2\pm0.4) \times 10^3$
5	$Mo(CN)_8^{4-} + GS^{\bullet} = Mo(CN)_8^{3-} + GS"$	1×10^6	1×10^5	0.1
4	$GS^{\bullet} + GS^{\bullet} = GSSG$	$(5.3\pm0.6) \times 10^7$	1.0×10^{10}	$(1.9\pm0.2) \times 10^2$
6	$Mo(CN)_8^{4-} = P$	2.00×10^3	1.00×10^{-4}	5.00×10^{-8}

1.0 mM K$_4$Mo(CN)$_8$ + 1.0 mM GSH + 100 mM phosphate buffer pH 10.00 + 1.0 M NaCl

#	Electrochemical Reactions	E	k$_s$	α
1	$Mo(CN)_8^{3-} + e^- = Mo(CN)_8^{4-}$	0.5916	0.03	0.5
3	$GS^{\bullet} + e- = GS^-$	0.5845	1.0×10^{-4}	0.5
	Chemical Reactions	**K**	**k$_f$**	**k$_b$**
2a	$GSH + PO_4^{3-} = GS^- + HPO_4^{2-}$	2×10^4	2×10^9	1
2b	$Mo(CN)_8^{4-} + GS^- = Mo(CN)_8^{3-} + GS^{\bullet}$	1.2679	$(5.5\pm1.9) \times 10^3$	$(4.1\pm1.5) \times 10^3$
5	$Mo(CN)_8^{4-} + GS^{\bullet} = Mo(CN)_8^{3-} + GS"$	1×10^6	1×10^5	0.1
4	$GS^{\bullet} + GS^{\bullet} = GSSG$	$(2.1\pm0.2) \times 10^8$	1.0×10^{10}	$(1.3\pm0.2) \times 10^2$
6	$Mo(CN)_8^{4-} = P$	2.00×10^3	1.00×10^{-4}	5.00×10^{-8}

1.0 mM K$_4$Mo(CN)$_8$ + 1.0 mM GSH + 200 mM phosphate buffer pH 10.00 + 1.0 M NaCl

#	Electrochemical Reactions	E	k$_s$	α
1	$Mo(CN)_8^{3-} + e^- = Mo(CN)_8^{4-}$	0.6096	0.0045 ± 0.001	0.5
3	$GS^{\bullet} + e- = GS^-$	0.5845	1.0×10^{-4}	0.5
	Chemical Reactions	**K**	**k$_f$**	**k$_b$**
2a	$GSH + PO_4^{3-} = GS^- + HPO_4^{2-}$	2×10^4	2×10^9	1
2b	$Mo(CN)_8^{4-} + GS^- = Mo(CN)_8^{3-} + GS^{\bullet}$	2.6558	$(3.6\pm0.2) \times 10^4$	$(1.3\pm0.8) \times 10^4$
5	$Mo(CN)_8^{4-} + GS^{\bullet} = Mo(CN)_8^{3-} + GS"$	1×10^6	2×10^5	0.2
4	$GS^{\bullet} + GS^{\bullet} = GSSG$	5.0×10^9	1.0×10^5	2.0×10^5
6	$Mo(CN)_8^{4-} = P$	2.00×10^3	1.00×10^{-4}	5.00×10^{-8}

1.0 mM K$_4$Mo(CN)$_8$ + 1.0 mM GSH + 300 mM phosphate buffer pH 10.00 + 1.0 M NaCl

#	Electrochemical Reactions	E	k$_s$	α
1	Mo(CN)$_8^{3-}$ + e$^-$ = Mo(CN)$_8^{4-}$	0.6096	0.0043±0.002	0.5
3	GS$^{\bullet}$ + e- = GS$^-$	0.5845	1.0×10^{-4}	0.5
	Chemical Reactions	**K**	**k$_f$**	**k$_b$**
2a	GSH + PO$_4^{3-}$ = GS$^-$ + HPO$_4^{2-}$	2×10^4	2×10^9	1
2b	Mo(CN)$_8^{4-}$ + GS$^-$ = Mo(CN)$_8^{3-}$ + GS$^{\bullet}$	2.6558	$(4.0\pm0.2) \times 10^4$	$(1.5\pm0.9) \times 10^4$
5	Mo(CN)$_8^{4-}$ + GS$^{\bullet}$ = Mo(CN)$_8^{3-}$ + GS"	1×10^6	2×10^5	0.2
4	GS$^{\bullet}$ + GS$^{\bullet}$ = GSSG	5.0×10^9	1.0×10^5	2.0×10^5
6	Mo(CN)$_8^{4-}$ = P	2.00×10^3	1.00×10^{-4}	5.00×10^{-8}

1.0 mM K$_4$Mo(CN)$_8$ + 1.0 mM GSH + 50 mM deuterated phosphate buffer pD 10.00 + 1.0 M NaCl

#	Electrochemical Reactions	E	k$_s$	α
1	Mo(CN)$_8^{3-}$ + e$^-$ = Mo(CN)$_8^{4-}$	0.5906	0.06±0.02	0.5
3	GS$^{\bullet}$ + e- = GS$^-$	0.5845	1.0×10^{-4}	0.5
	Chemical Reactions	**K**	**k$_f$**	**k$_b$**
2a	GSH + PO$_4^{3-}$ = GS$^-$ + HPO$_4^{2-}$	2×10^4	2×10^9	1
2b	Mo(CN)$_8^{4-}$ + GS$^-$ = Mo(CN)$_8^{3-}$ + GS$^{\bullet}$	1.2679	$(5.3\pm0.3) \times 10^3$	$(4.0\pm0.4) \times 10^3$
5	Mo(CN)$_8^{4-}$ + GS$^{\bullet}$ = Mo(CN)$_8^{3-}$ + GS"	1×10^5	1×10^5	1
4	GS$^{\bullet}$ + GS$^{\bullet}$ = GSSG	2.0×10^5	1.0×10^6	5
6	Mo(CN)$_8^{4-}$ = P	4.00×10^3	1.00×10^{-4}	2.50×10^{-8}

Appendix 2F. Determination of heterogeneous rate constants using the method of Nicholson

For our system, the effect of ohmic potential losses is negligible because highly conductive supporting electrolytes was used to reduce the total solution resistance. The switching potential (E_λ) is at least 200 mV beyond anodic and cathodic peaks.[2] The shape of cyclic voltammgrams (i-E curves) and current peak difference (ΔE_p) for the reversible one-step, one-electron process are functions of scan rate (v), heterogeneous rate constant ($k°$), transfer coefficient (α) and diffusion coefficient (D). The i-E curves are functions of parameter ψ, defined by Eq. S6.[3]

$$\psi = \frac{k°}{(\pi D f v)^{1/2}} \qquad\qquad \text{Eq. 2F.6}$$

Where, $f = F/RT = 38.92$ V^{-1}. The diffusion coefficient values of the oxidants (M^+) and their reduced species (M) were assumed the same.

For example, $D_{Mo(CN)83-} = D_{Mo(CN)84-} = 2.82$ x 10^{-6} cm^2/s, $\Delta E_p = 61$ mV, $v = 0.1$ V/s, $\psi = 20$;

$k° = 20$ (π x2.82 x 10^{-6} cm^2/s 38.92 V^{-1} x 0.1V/s)$^{1/2} = 0.12$ cm/s.

The rate constants at various scan rates were calculated (0.1, 0.3, 0.5, 0.7, 1 V/s) using the method of Nicholson which are on the same order of maginitude as the values obtained from digital simulation. Table 2F.1 shows the average values of heterogeneous rate constants for three mediators.

Table 2F.1 Heterogeneous rate constants data of three mediators calculated at various scan rates

Oxidant	*Mo(CN)$_8$$^{3-}$*	*IrCl$_6$$^{2-}$*	*Fe(phen)$_3$$^{3+}$*
$k°$	0.25 ± 0.09	0.12 ± 0.04	0.3 ± 0.1

Appendix 2G. List of references

1.   Madej, E.; Wardman, P., The oxidizing power of the glutathione thiyl radical as measured by its electrode potential at physiological pH. *Arch. Biochem. Biophys.* **2007,** *462* (1), 94-102.

2.   Bard, A. J.; Faulkner, L. R., *Electrochemical methods : fundamentals and applications*. 2nd ed.. ed.; New York : Wiley: 2001; p 833.

3.   Nicholson, R. S., Theory and Application of Cyclic Voltammetry for Measurement of Electrode Reaction Kinetics. *Analytical Chemistry* **1965,** *37* (11), 1351-+.

Appendix 3 (Chapter 3)

Appendix 3A. Mass spectroscopy data of Trolox in methol-acetic solution

Appendix 3B. Mass spectroscopy data of oxidized Trolox in methol-water solution

Appendix 3C. UV-vis spectra of Trolox in different solvents prior to and after bulk elctrolysis

Appendix 3D. UV-vis spectra of Trolox in aqueous solutions at various electrolysis times

Appendix 3E. UV-vis spectra of Trolox in the mixture of water and acetonitrile with different pH values

Appendix 3A. Mass spectroscopy data of Trolox.
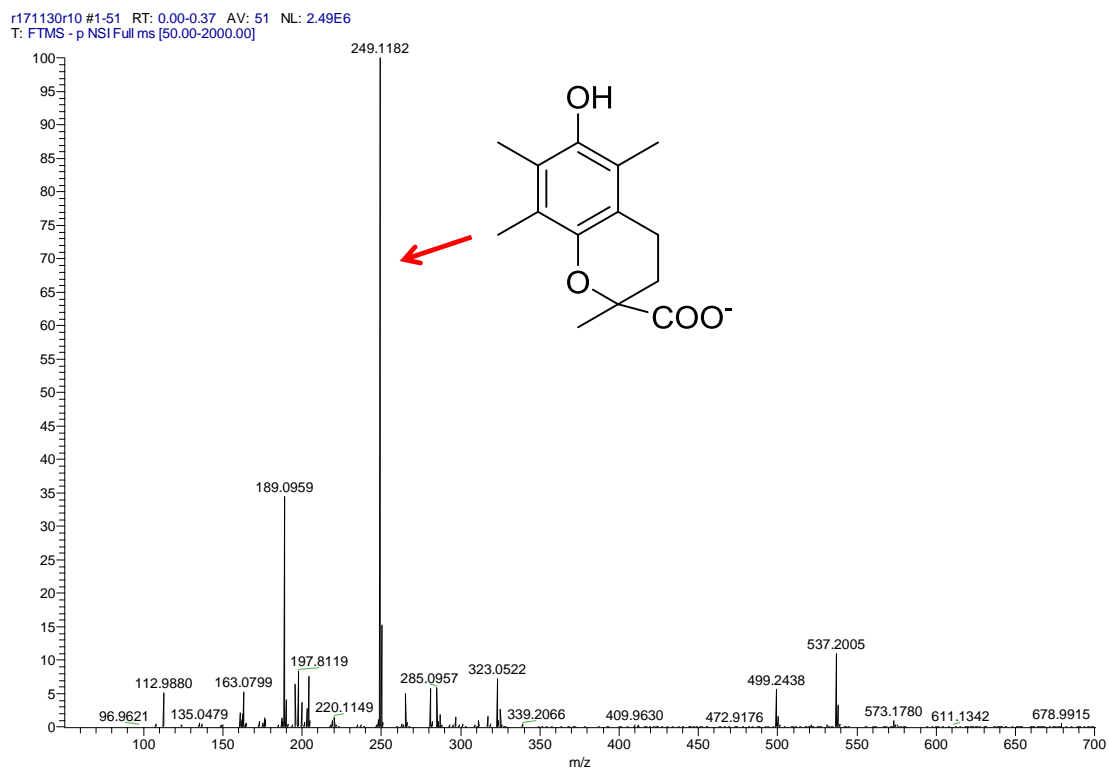
Figure 3A. ESI-MS spectra (negative mode) of Trolox in methanol + 0.1% acetic acid water solution (50-700 m/z).

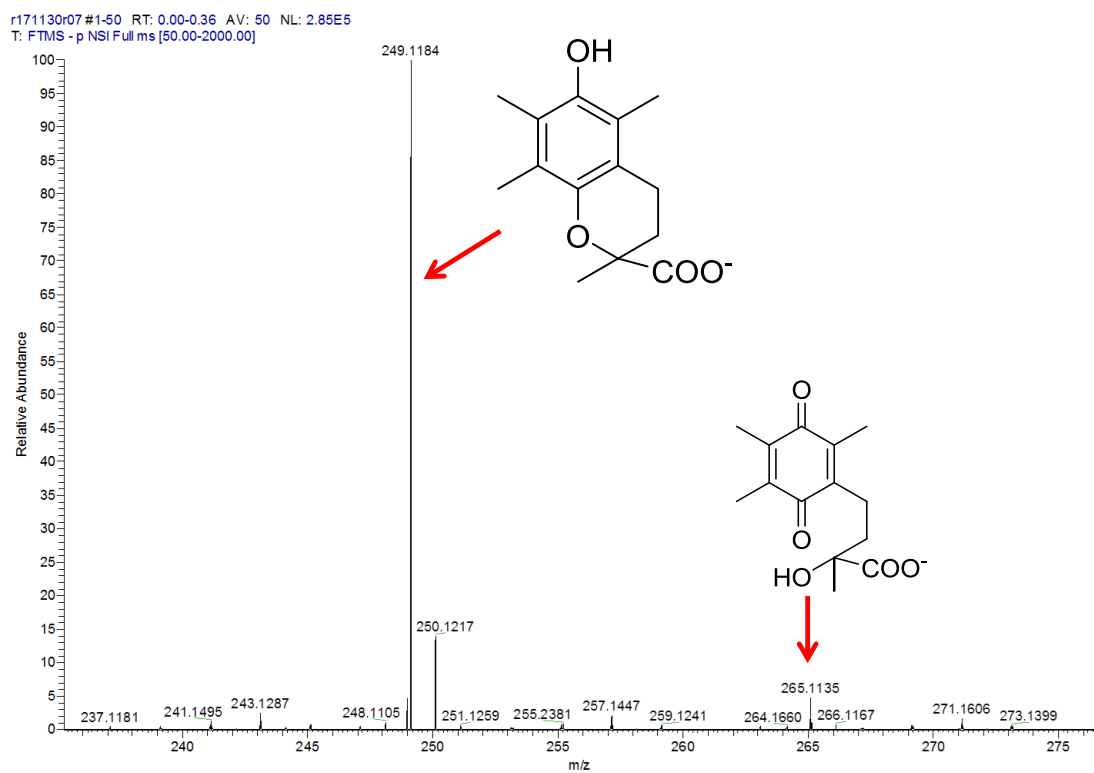**Appendix 3B.** Mass spectroscopy data of oxidized Trolox in methol-water solution

Figure 3B. ESI-MS spectra (negative mode) of oxidized Trolox in methanol water solution (235-275 m/z).

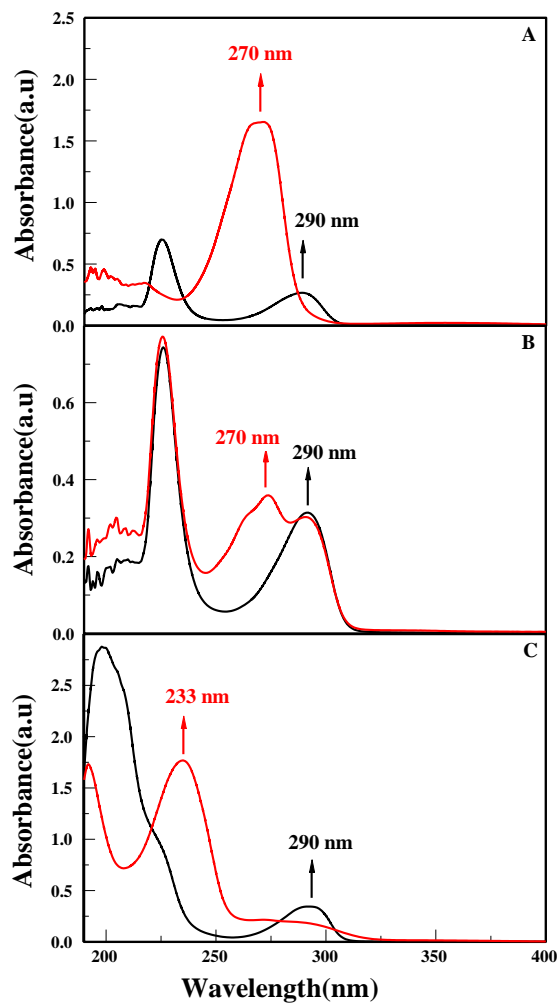**Appendix 3C.** UV-vis spectra of Trolox in different solvents prior to and after bulk elctrolysis

Figure 3C. UV-vis spectra obtained with 0.1 mM Trolox in (A) water with 0.2 M CH_3COONa; (B) acetonitrile + water (3:3, v/v) with 0.2 M CH_3COONa; (C) acetonitrile with 0.25 M Bu_4NPF_6; prior to the bulk oxidation of Trolox (black lines), after the oxidation of Trolox over 7200s, 700s, 4400s, respectively (red lines).

Appendix 3D. UV-vis spectra of Trolox in aqueous solutions at various electrolysis times
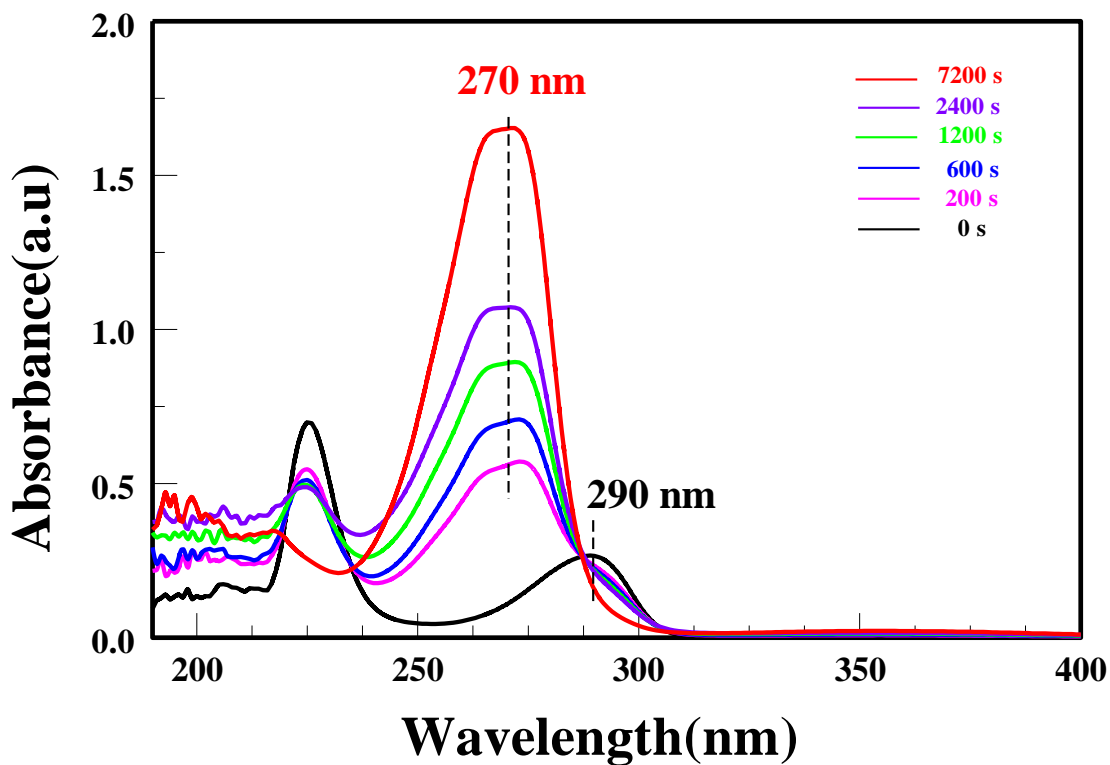

Figure 3D. UV-vis spectra obtained during the bulk oxidation of 0.1 mM trolox in water with 0.2 M CH$_3$COONa with different bulk electrolysis times.

Appendix 3E. UV-vis spectra of Trolox in the mixture of water and acetonitrile with different pH values
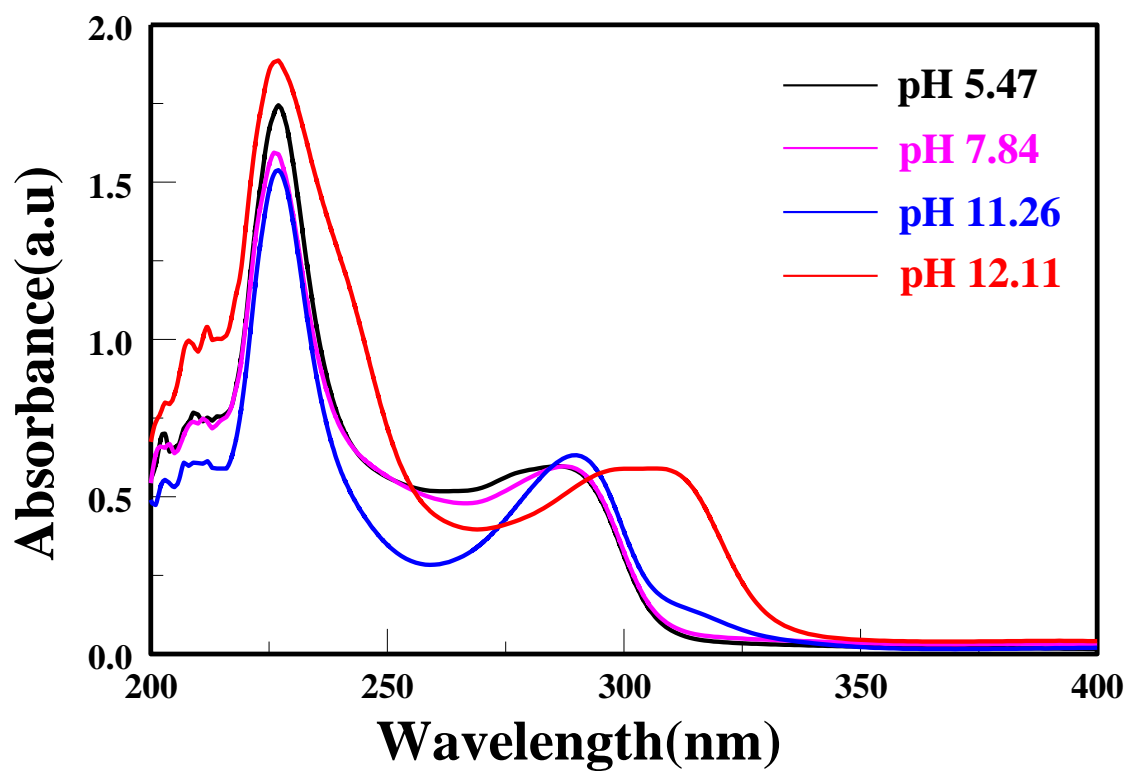

Figure 3E. UV-vis spectra for 0.25 mM trolox in water + acetonitrile (5:1, v/v) with 0.2 M CH₃COONa with different pH solutions.